THE UNIVERSITY OF SYDNEY

Detection and Characterisation of Combustion Formed Nanoparticles Using Time-Resolved Laser-Induced Emission

by

Daniel Bartos

A thesis submitted in fulfilment for the degree of Doctor of Philosophy

PhD

in the

Faculty of Engineering and I.T.

School of Aerospace, Mechanical and Mechatronic Engineering

2018

Publications

Published

D. Bartos, M. Dunn, M. Sirignano, A. D'Anna and A.R. Masri "**Tracking the Evolution of Soot Particles and Precursors in Turbulent Flames Using Laser-Induced Emission**" *Proceedings of the Combustion Institute* 36, no. 2 (2017): 1869-1876.

M. Sirignano, D. Bartos, M. Conturso, M. Dunn, A. D'Anna and A.R. Masri "**Detection of Nanostructures and Soot in Laminar Premixed Flames**" *Combustion and Flame* 176, (2017): 299-308.

In Progress - at time of submission

D. Bartos, M. Sirignano, M. Dunn, A. D'Anna and A.R. Masri "**Soot Inception in Laminar Coflow Diffusion Flames**".

D. Bartos, M. Dunn, M. Sirignano, A. D'Anna and A.R. Masri "**The Influence of Partial Premixing and Dilution on the Evolution of Soot in Laminar Diffusion Flames**".

Abstract

This thesis provides an improved characterisation of the evolution of soot nanoparticles in laminar and turbulent flames with a particular focus on the transition from nucleation to solid particles where intermediate structures occur. Laser pulses of wavelengths 266 nm and 1064 nm are used to probe a variety of combustion conditions, including; diffusion, premixed and turbulent flames. Laser light at 266 nm is primarily used for Laser-Induced Fluorescence (LIF) measurements as a means to detect and characterise incipient soot nanostructures that retain molecular qualities with sizes in the order of a few nanometres known to absorb light in the ultraviolet (UV). These species are often referred to as soot precursors and do not absorb light at longer visible and infrared (IR) wavelengths. In addition, the 266 nm laser is used for Elastic Light Scattering (ELS) and Laser-Induced Incandescence (LII) that prevail where larger solid particles are present. The 1064 nm laser, on the other hand, is used to exclusively excite solid soot particles that do absorb in the IR and preferentially incandesce. The combination of these Laser-induced-Emissions (LIE) is used to track the presence and character of both soot and soot precursor nanostructures. A key feature of these measurements is the ability to track the temporal decay of LIEs. This is captured by using suitably fast photomultiplier tubes (PMTs) placed within a purpose-built spectrometer. Measurements taken in different combustion conditions highlight different behaviours and properties of combustion formed particles. In all cases the lifetime of the majority of LIF signals is found to be much longer than that expected for molecules present with these flames at the same temperature, yet much shorter and spectrally different than that of soot particles, as is expected from semi-rigid structures. Premixed flat flames show a co-existence of soot precursors with lager soot particles in downstream locations, whereas laminar diffusion flames exhibit some separation where these two particle modes are observed. An obvious transition from smaller aromatic species to larger more rigid nanostructures is inferred from redshifted spectra downstream and longer fluorescent decay times.

The in-house developed technique also proved sensitive enough to resolve instantaneous LIE from the intermittent turbulent combustion. Measurements in a diffusion jet flame with a Reynolds number of 10,000 highlighted the spatial and instantaneous co-existence of nanostructures and soot in downstream regions, showing similarities to premixed flames more than laminar diffusion flames. Nanostructures investigated in laminar partially premixed flames also exhibit LIE somewhere between that of premixed and diffusion cases. Additionally, partial premixing shows that the initial enhancement of soot formation due to the presence of small amounts of oxygen is subsequently supressed due to the effects of dilution whilst nanostructures persist.

Collectively, these findings confirm the hybrid nature of nanostructures (semi-solid structure retaining molecular qualities) that dominate the early evolution of soot and highlight the multiple pathways in which soot precursor nanostructures initiate and evolve.

Declaration of Authorship

I certify that the intellectual content of this thesis is the product of my own work and that all the assistance received in preparing this thesis and sources have been acknowledged. This thesis has not been submitted for any degree or other purposes. This work was done wholly while in candidature for a research degree at this University. Where I have consulted the published work of others, this is always clearly attributed. Where the thesis is based on work done by myself jointly with others, I have made clear exactly what was done by others and what I have contributed myself.

Furthermore, this thesis contains material previously published [1, 2] and under review.

Chapter 4 of this thesis draws heavily from [1]. I co-designed the study, extracted and analysed the data and provided substantial edits and review of the manuscript.

Chapter 5 draws heavily from a paper currently under review. I designed the study, extracted and analysed the data and wrote the draft of the manuscript.

Chapter 6 draws heavily from a paper currently in final edits. I designed the study, extracted and analysed the data and wrote the draft of the manuscript.

Chapter 7 draws heavily from [2]. I designed the study, extracted and analysed the data and wrote the draft of the manuscript.

In addition to the statements above, in cases where I am not the corresponding author of a published item, permission to include the published material has been granted by the corresponding author.

Signed: _____

Name: DANIEL BARTOS

Date: _____

Acknowledgements

I wish to acknowledge the following people who have contributed to the work in this thesis in no particular order.

I would like to express my sincerest gratitude to Prof. Assaad Masri and Dr. Matthew Dunn for their continuous support and supervision over course of my candidature. Without their guidance, motivation, and knowledge, I would not have had the opportunity to explore the intricacies of pollution formation. They are both incredibly passionate about their work, and I am grateful for their friendship and mentorship during this PhD.

I would also like to thank all of those with whom I have had the pleasure of working with during this PhD and related research. A particular thanks to Dr. Mariano Sirignano who visited Sydney from Naples multiple times to help implement the experimental apparatus and suffer my many questions. His knowledge and patience were invaluable to the project. To Dr. Mrinal Juddoo, Dr. Agissilaos Kourmatzis and Dr. Phuong Pham, who provided valuable assistance in the laboratory along with many past and present members of the Clean Combustion Group at the University of Sydney. To Prof. Andrea D'Anna, for the numerous discussions had relating to this joint endeavour between Università degli Studi di Napoli Federico II and The University of Sydney.

Last but not least, I would like to thank my family and friends. To my parents, Brianne and Robert, who endlessly offered to help anyway that they could. To Nick and Kate for their support and encouragement throughout the past few years. To my girlfriend Lili, whose understanding and support has been invaluable in helping me finish what I started. And finally, to my friends who always there through the good and the tough times.

This work would not have been possible without the financial support of the Australian government and The University of Sydney for my scholarship and funding for the project by the Australian research council.

Table of Contents

List of Figures and Tables

Figures

Tables

Nomenclature

Abbreviations

AFM	Atomic Force Microscopy
C/O	Carbon to Oxygen (Ratio)
CCD	Charged Couple Device
DMA	Differential Mobility Analysis
DN	Nitrogen Diluted (Flame Set)
ELS	Elastic Light Scattering
FWHM	Full Width Half Maximum
H/C	Hydrogen to Carbon (Ratio)
HAB	Height Above Burner
HACA	Hydrogen-Abstraction Carbon-Addition (Mechanism)
ICCD	Intensified Charged Couple Device
IR	Infrared
ISF	International Sooting Flame (Workshop)
LIE	Laser-Induced Emission
LIF	Laser-Induced Fluorescence
LII	Laser-Induced Incandescence
MM	Method of Moments
MS	Mass Spectrometry

Nd: YAG	Neodymium-doped Yttrium Aluminium Garnet (Laser)
NOC	Nano-Organic Carbon
NVfx	Nanostructure flux
OA	Off-Axis (Mirror)
PAH	Polycyclic Aromatic Hydrocarbon
PDF	Probability Distribution Function
PMT	Photomultiplier Tube
PP	Partially Premixed (Flame Set)
PSD	Particle Size Distribution
S/B	Signal to Background (Ratio)
S/N	Signal to Noise (Ratio)
SM	Sectional Method
SVF	Soot Volume Fraction
SVfx	Soot Volume Flux
TEM	Transmission Electron Microscopy
TPD	Thermocouple Particle Densitometry
TRFPA	Time-Resolved Fluorescence Polarisation Anisotropy
UV	Ultraviolet
UV/Vis	LIF Ratio: LIF @ 350 nm/ LIF @ 445 nm

Symbol

$\dot{Q}_{abs}$	Absorptive Heating Rate
p_0	Bath Gas Pressure
T_0	Bath Gas Temperature
S(λ)	Black Body Signal
k_B	Boltzmann Constant
U_{bulk}	Bulk Velocity
$U_{bulkTad}$	Bulk Velocity Temperature Adjusted
m	Complex Index of Refraction
$\dot{Q}_{cond}$	Conductive Cooling Rate
I_E	Emission Function (non-convoluted)
ε	Emissivity
$\dot{Q}_{sub}$	Evaporative Cooling Rate
$f_{\#}$	F Number (Camera)
τ	Fluorescence Lifetime
ϕ	Fuel-Air Equivalence Ratio
C_p	Heat Capacity of Air at Constant Pressure
$\dot{Q}_{ann}$	Heating Rate from Annealing
A	Initial Emission Intensity
U_{int}	Internal Energy
W_a	Molecular Weight of Air
N_i	Number of Particles

$\dot{Q}_{ox}$	Oxidative Heating Rate
d, d_p, d_i	Particle Diameter
M	Particle Mass
π	PI Constant or Chemical Bond or Electron
$\dot{Q}_{rad}$	Radiative Cooling Rate
h	Plank constant
k	Rate Constants
Q_{vv}	Rayleigh Approximation Scattering Intensity
I_R	Recorded Signal (convoluted)
m	Reflection Order (Grating)
$E(m)$	Refractive Index for Absorption
σ	Sigma Bond or Standard Deviation
c	Speed of Light
I_S	System Response
t	Time
T	Temperature
α_T	Thermal Accommodation Coefficient
$\dot{Q}_{therm}$	Thermionic Cooling Rate
R	Universal Gas Constant
λ	Wavelength

Chemical Symbols

A_i	Aromatic with *i* Rings
C	Carbon Atom
C_2	Carbon Cluster
C_3	Carbon Cluster
C_2H_2	Acetylene
C_2H_4	Ethylene
C_3H_3	Propargyl Radical
CH_4	Methane
CO	Carbon Monoxide
CO_2	Carbon Dioxide
H	Hydrogen Atom
H_2	Hydrogen Gas
H_2O	Water
N_2	Nitrogen Gas
OH	Hydroxyl Radical
Pt	Platinum
Rh	Rhodium

Units

°	Degree (Angle)
m	Metre
cm	Centimetre
mm	Millimetre
µm	Micrometre
nm	Nanometre
s	Second
ns	Nanosecond
ps	Picosecond
kPa	Kilopascals
°C	Degrees Celsius
K	Degrees Kelvin
cm^{-1}	Wavenumber
V	Volts
GHz	Gigahertz
Hz	Hertz
J	Joules
mJ	Millijoules
SLPM	Standard Litres Per Minute (standard conditions of 25 °C and 101.3 kPa)

Chapter 1: Introduction

The energy density and availability of hydrocarbon fuels still makes combustion a very versatile and sought-after source of energy. Although there is a strong social shift towards the use of 'renewable' energies, such as wind and solar, there are many industries where the near-term demand cannot be met by renewable sources. While research into such technologies is prevalent and important [3], the role of combustion in the world's energy future is all but set to continue as energy demand continues to increase. Hence the research and development into the many forms of combustion and related technologies is very relevant given the associated environmental and health impacts.

There is scientific consensus that recent anthropogenic activity is a major contributor to climate change. Industries including power generation and transport are front and centre of this issue due to their significant emissions of CO_2 (carbon dioxide) and other pollutants from the burning of fossil fuels [3]. Over the past few decades improvements to combustion processes have increased efficiencies and reduced pollution emissions. However, combustion is still a significant contributor to greenhouse gas emissions and other pollutants [3, 4]. Particulate emissions, such as those found in photochemical smog, have also received increased attention in recent years, in particular soot and ultrafine particles. Particles ranging from few nanometres to hundreds of nanometres have their own direct environmental and health implications [5-11].

The majority of combustion generated particulates originate from unburned and partially burned hydrocarbons. Polycyclic aromatic hydrocarbons (PAHs) are abundant in our environment, being present as volatile, semi-volatile and particulate pollutants that are the result of incomplete combustion [12]. Airborne particulate matter was a concern to health before combustion technologies, consequently the human body has natural defences against inhaling and ingesting such particles [6]. However, significant correlation has been established between fine particle exposure and adverse health effects [5, 7]. Combustion formed particles often consist of harmful and carcinogenic chemicals and are present in sizes less than 100 nm [11, 13]. The fine nature of these particles allows them to bypass

some of the body's defences and facilitates uptake into cells, which then allows access into blood and lymph circulation. The adverse health implications include reduced lung function, heart disease, lung disease and cancers [6, 7]. Emission from traffic in urban areas is known to consist of large quantities particles as small as 3 nm [13] and thus governments are putting stricter restrictions on ultrafine particulate emissions [14].

The field of atmospheric chemistry also places importance on ultrafine particle emission into the atmosphere and has provoked debate on the impact of primary particles emitted from combustion systems and the secondary particles produced through atmospheric reactions [15]. Fine particles emitted from the burning of biomass and fossil fuels influence the climate by changing cloud formation and disturbing the radiation balance in the atmosphere. Ultrafine particles can serve as nucleation points for the formation of clouds, impact their reflectance and reduce droplet size [16]. Black-carbon (often referred to as soot) emissions are also problematic for climate change as they strongly absorb light in the visible and infrared (IR) spectrum [17]. Deposits of these larger particles are known to reduce the reflectivity of snow and ice and accelerate their melting [18, 19].

While the formation of most particulates can be prevented by having complete combustion of the fuel, this is not always possible in practical combustion devices, nor is it always desired [20]. Industrial furnaces, for example, rely on soot formation to maximise heat transfer rates through radiation. Biofuels can be used to close the carbon cycle and provide a "greener" alternative to fossil fuels, but do not necessarily result in fewer particle emissions [21, 22]. Furthermore, combustion is often used for the synthesis of materials [23], where the production of particles and solids is desired. Gaining a thorough understanding of the formation and evolution processes of combustion formed particles is important both for the reduction of harmful pollutants and the formation of unique materials.

Combustion processes can be broadly separated into premixed and non-premixed (also referred to as diffusion) modes. Premixed combustion is where the fuel is mixed with the oxidiser, typically oxygen in the form of air, prior to burning. Non-premixed, on the other hand, initially has the fuel and oxidiser separate and relies on mixing and transport phenomena to produce locations of flammable mixture to facilitate the combustion. Lean premixed combustion, where there is excess oxygen within the flammable mixture, will result in complete combustion of the fuel and will not produce particulates. On the other end of the spectrum, non-premixed combustion will facilitate the formation of PAHs in pyrolytic regions that then leads to the formation of soot precursor particles and finally soot [15]. Rich premixed and mixed mode combustion can also produce PAHs and particulates. Non-premixed or partially premixed combustion is common for practical combustion devices. Spray and particle combustion, such as occurs in internal combustion engines and

coal furnaces for example, operate in a diffusion mode of combustion as the fuel source is in a different physical state than the oxidiser (air) [24, 25].

The formation of PAHs and particulates is also linked to many other properties including fuel chemistry, flame temperature, pressure and residence time [15, 26, 27]. Understanding the mechanism of soot particle formation in flames, particularly in the inception stages, remains an outstanding challenge despite extensive research that has already been published on this topic [15, 28-30]. It is noted here that soot precursor particles are also often referred to as ultrafine particles, condensed phase, semi-volatile, nascent soot or nano-organic carbon (NOC). However, in this work soot precursor particles are mostly referred to as "nanoparticles" or "nanostructures". Such particles exhibit physical and chemical properties somewhere between those of large aromatic molecules and solid particles [31]. Soot primary particles and aggregates are found to absorb light over a broad spectrum, from the ultraviolet (UV) to the infrared (IR). Nanoparticles, on the other hand, are found to be mainly visible-transparent and appear to interact with light somewhat differently from soot aggregates because of their condensed phase state and transitional nature [15, 32-34] while exhibiting transport and surface related phenomena typical of larger particles. These characteristics of nanoparticles and their role in the initiation and evolution of soot will be further explored through this thesis.

There are a variety of techniques used to identify and characterise combustion formed particles, both in-situ and ex-situ, that exploit their range of physical and spectroscopic properties [15, 29, 30]. Ex-situ techniques such as differential mobility analysis (DMA) [13, 35-39] and transmission electron microscopy (TEM) [40-42] can provide rich information on size, structure and morphology. In-situ techniques, on the other hand, are often far are less intrusive, such as the optical methods: elastic light scattering (ELS), absorption, and laser-induced emissions (LIE). These optical methods can also be used to infer size, concentration and chemical composition. Within this document the term "soot" is used specifically in reference to solid particles, both primary particles and aggregates, defined by their ability to absorb in the IR and incandesce. An optical technique, Laser-Induced Incandescence (LII) is generally attributed to soot particles and aggregates in the order of tens to hundreds of nanometres that are sufficiently graphitic to be heated up to temperatures of 3500-4500 K [30, 43-47]. Other "nanoparticles/nanostructures", nominally less than 10 nm in diameter, are less likely to absorb in the IR and hence are defined by their capability to fluoresce under UV excitation. While Laser-Induced Fluorescence (LIF) has been reported from nanostructures, both in the presence and absence of soot [28, 29, 33, 48-53], controversy about the hybrid nature of these nanoparticles and their ability to fluoresce still exists [31, 52, 54]. Although the fluorescence from these structures is from

aromatic groups, an important distinction is made in the current work between LIF originating from gas phase PAHs and those bound in nanostructures.

The primary objective of this work is to show the hybrid nature of nanoparticles and track their role in the formation and evolution of larger particles. The use of LIF, LII and ELS techniques provide crucial insight in the nature and evolution of combustion formed particles. While an extensive body of literature is reported on the structure of sooting laminar premixed and diffusion flames using a variety of techniques [15, 28-30], similar research in turbulent flames is rather limited [49, 55-63] due to the difficulty of applying the same diagnostic methods and simultaneously resolving the relevant time and spatial scales. A secondary objective of this work addresses particle measurements in turbulent combustion. The LIE based technique developed here was designed to simultaneously probe both soot and nanoparticles whilst also being able to resolve instantaneous measurements, making it very suitable for resolving instantaneous features in turbulent combustion.

This thesis presents a novel application of LIE techniques that required the design and manufacture of a custom spectrometer. This spectrometer allowed for the simultaneous collection of ELS, LIF and LII, originating from combustion formed particles. The combination of fast response photomultiplier tubes (PMT) and a high bandwidth oscilloscope meant that individual signals could be temporally resolved. This temporal resolution is crucial in delineating between types of LIE and the origin of them. This technique was then applied to a range of combustion conditions in laboratory flames. Rich premixed, diffusion, partially premixed and turbulent diffusion flames are explored and compared in terms of their sooting propensity and structure. This thesis consists of 8 Chapters, including the introduction, background, methodology, four Chapters investigating different combustion conditions and finally conclusions and recommendations. The majority of the work presented here has either already been published [1, 2] or is currently under review, hence the discussion is presented in a similar format to that of journal papers.

Chapter 2 discusses the current state of research in soot formation including relevant techniques. Fundamental concepts and theory are introduced here facilitating further discussion in later Chapters.

Chapter 3 describes the experimental apparatus used throughout this work, including the design and calibration of the system. Also covered are methods of data processing and description of the burners used in the proceeding investigations.

Chapter 4 concerns measurements within rich premixed flames used to establish the novel technique. The work presented in this Chapter has been previously published [1] and contains complementary measurements from Università degli Studi di Napoli Federico II.

Chapters 5, 6, and 7 investigate the evolution of soot and nanoparticles across diffusion, partially premixed and turbulent diffusion flames respectively. Discussions and specific conclusions to each Chapter are contained within. These Chapters are followed by a general conclusion and the author's thoughts for the direction of future work in Chapter 8.

Chapter 2: Background

Combustion occurs in many forms with each having unique characteristics and applications. At one end of the flame spectrum exists premixed combustion. This is where fuel and oxidiser, usually pure oxygen or air, are homogeneously mixed prior to ignition at the flame front. The flame front is defined by an area of dense chemical reactions and heat release resulting in a rapid increase in temperature, consumption of reactants and formation of products. Premixed flames may also be lean, rich or stoichiometric depending on the relative amount of fuel and oxidiser are present in the mixture. This distinction is typically defined using the fuel-air equivalence ratio (ϕ). Equation 2.1 defines ϕ as the ratio between the relative mass (m) of fuel and air present in the mixture and relative amount of fuel and air found in a stoichiometric (st) mixture. At the other end of the spectrum is non-premixed combustion (also referred to as diffusion). These flames rely on diffusive transport of initially separate fuel and oxidiser to achieve locations of a flammable mixture. The non-premixed flame front exists at the interface of the fuel and oxidiser, spread either side of the stoichiometric mixture contour. While there are various examples of practical combustion that utilise either premixed or non-premixed modes, many combustion technologies operate somewhere in between having some level of mixing prior to combustion but where flame propagation is still limited by diffusion of fuel and oxidiser molecules to reach a combustible mixture. This mode of combustion is known as partial premixing. Additional characteristics such as inhomogeneity, stratification and dilution in fuel and oxidiser mixtures add complexities to these definitions.

$$\phi = \frac{m_{fuel}/m_{air}}{(m_{fuel}/m_{air})_{\mathrm{st}}} \qquad (2.1)$$

The formation of particulate matter, in particular soot, and other pollutants is generally associated with incomplete combustion of hydrocarbons. This is where there is insufficient oxygen present to complete the stoichiometric reactions of fuel and oxidiser to water (H_2O)

and carbon dioxide (CO_2). Such conditions exist in rich premixed flames and on the fuel side of diffusion (including partially premixed) flames. These conditions, by definition, have $\phi > 1$, meaning that the local oxygen content is insufficient for a complete stoichiometric reaction. The excess fuel thermally decomposes and recombines to form benzene [64, 65] naphthalene and other polycyclic aromatic hydrocarbons (PAH). PAHs are a group of molecules defined by their aromatic ring structure. Aromatic rings are unique carbon molecules, where the six sp^2 hybridised carbon atoms are sigma (σ) and pi (π) bonded in a hexagonal (or ring) configuration. PAHs consist of two or more aromatic rings joined in a chain or cluster. PAHs with relatively few number of rings, such as pyrene and anthracene, are commonly found in flames, while much larger PAHs can also be present but exist in much lower concentrations [66-68]. Pyrene is found to be a very common product in combustion of organic fuels and has previously been used in kinetics models [69-72] built to help understand the inception process. The Hydrogen-Abstraction Carbon-Addition (HACA) mechanism is generally accepted as a dominant contributor to the formation of PAHs [28], where acetylene (C_2H_2) is an important intermediate species in fuel rich conditions [73-75]. Model reactions for PAH growth via HACA mechanism is presented in Equations 2.2, 2.3, and 2.4, where A is an aromatic species with *i* number of rings. PAHs are known precursors of soot, with formation of the first nanoparticles linked with the nucleation of PAHs and acetylene formed through pyrolysis of the fuel [28, 29, 64, 65, 76]. Despite the large amount of literature on the subject, the formation and evolution mechanisms for combustion formed particles have not been completely identified [15, 28, 43, 64, 69, 77-82].

$$A_i + H \rightleftharpoons A_{i-} + H_2 \tag{2.2}$$

$$A_{i-} + C_2H_2 \rightleftharpoons A_iC_2H_2 \tag{2.3}$$

$$A_iC_2H_2 + C_2H_2 \rightleftharpoons A_{i+1} + H \tag{2.4}$$

2.1.1 Combustion Formed Particles

Understanding the nature and formation processes of combustion formed particles is crucial for the responsible use of combustion technologies given the extent of their environmental [12, 16-19] and health impacts [5-9, 11]. Ultrafine particles formed in combustion can escape controlled combustion systems and be emitted into the atmosphere. Particles less than 10 nm are known to bypass particle filters in diesel engines for example [83] and be released through the exhaust. The combustion conditions and the fuel composition play a significant role in the morphology, number and size of formed and emitted particles [64, 76, 84-86]. Soot particles have been characterised in terms of size

distribution [13, 35-39], optical features [34, 87-93] and their impact on the environment [12, 17] and human health [8]. The existence of compounds different from primary soot particles and aggregates based on size, optical features, and lifetimes in flames and the atmosphere has also been known since the early 1990s [32-34, 87].

Particles formed in combustion can generally be grouped under two headings: "nanoparticles/nanostructures" and "soot" particles. Nanoparticles exist in the transition between the gas-phase and solid particles and are also labelled as soot precursor particles [41, 87, 94-96], condensed phase [28], nascent soot [28, 97] or nano-organic carbon [15, 49, 98-102]. Soot particles, on the other hand, can be labelled as either young or mature* [40], but is largely concerned with solid particles. The definitions of nanoparticle and soot can vary slightly depending on the technique used to measure them due to the transitioning of properties experienced by the particles in the growth process. However, there are general characteristics associated with either nanoparticle or soot that can be used to discriminate between them.

Nanoparticles are believed to be PAH clusters, stacked compactly or in loose oligomers comprising of aliphatic and aromatic bonds [29, 51], nominally less than 10 nm in diameter, but not exclusively defined by size. While nanoparticles display transport and surface related phenomena typical of larger particles, they also maintain chemical reactivity and spectroscopic properties of their constituent gas-phase products. Because nanoparticles are composed of organic species with high hydrogen to carbon ratio (H/C) [43, 103] and often contain oxygen [66, 104-106], these particles are thus typically more reactive. On the other hand, the largest soot particles, that can be 100s of nanometres in diameter, have a well-known chain-like structure in which primary particles can be distinguished within aggregates [42, 91, 107]. The primary particles are covalently bonded to form aggregates with fractal dimension typically in the range of 1.7 to 1.9 [108, 109]. Soot primary particles have a more graphite like structure, exhibiting low H/C [43, 110, 111]. Soot does not display molecular characteristics such as fluorescence and behaves like a blackbody in terms of its absorption and emission spectra [43]. In fact, the presence of soot can often be observed by eye as the yellow part of the flame in fuel rich conditions, caused by incandescence of hot solid particles.

Particle size distribution in laminar flames has been shown to be bimodal [13, 22, 36, 97, 112]. Measurements in a rich premixed ethylene flames presented by D'Anna [15] by

* In the literature the term "soot" is often used more broadly than it is in this work and the difference between "nanostructures" and larger soot primary particles is distinguished by a scale of "maturity". Maturity of soot is usually a function of the H/C ratio. The techniques used in this work are unable to determine the H/C ratio of measured particles and thus using such a definition does not makes sense here. In any case, the author would also argue that this definition of soot is too broad as the properties possessed by "nanostructures", chemical, physical and photo-physical, are starkly different from those of primary and aggregated soot particles as described in this chapter.

means of differential mobility analysis (DMA) demonstrated two population peaks. Particles as small as 1 nm in diameter were able to be detected with this technique in a premixed ethylene flame of carbon to oxygen ratio (C/O) = 0.77, or ϕ = 2.31. Figure 2.1 reports size distribution of particles in the flame, showing a distinct peak of nanoparticles in the first mode and a much broader distribution of particle sizes in the second mode. Nanoparticles predominate just downstream of the flame front (HAB = 4 mm). In this region of the flame light absorption in the UV up to 300 nm is observed via extinction measurements [15, 88] as well as fluorescence from UV excitation [21, 113]. Similar extinction and fluorescence observations have been made on the fuel side of diffusion flames [51, 99, 101, 113]. Also observed in these regions, prior to soot, is excess of ELS above the gas phase [15, 88, 101, 114]. While the nanoparticles detected by both DMA and excess scattering are correlated with the presence of absorption and Laser-Induced Fluorescence (LIF), this spectroscopic behaviour is generally associated with molecular species, specifically PAHs absorbing in the UV and exhibiting fluorescence that ranges from the excitation wavelength up to at least 500 nm [26, 115-117]. However, Bruno et al. [98, 118-121] showed that the fluorescence from this region originates from larger structures through the use of time-resolved fluorescence polarisation anisotropy (TRFPA). This is a technique that assesses the rate of depolarisation of fluorescence emission and attributes it to the size-dependent rotational diffusion rate due to Brownian motion of the particles. Thus, TRFPA found that the species responsible for fluorescence were larger than 2 nm and up to 20 nm is some cases [122]. In addition to this, the general fluorescence lifetime measured in these regions has shown to be excessively long for it be attributed to gas phase PAH. Ossler et al. [117] showed that the fluorescence lifetime of molecular PAH decreased rapidly in presence of elevated temperature. PAHs such as naphthalene exhibit an exponential decay with a characteristic decay time (τ) less than 1 ns at 1200 K. Flame temperatures in the pre-soot region very often exceed 1200 K whilst also exhibiting fluorescent decay times in excess of a few nanoseconds [51]. Although the attribution of fluorescence in these regions to nanostructures is apparent in the literature, there are still numerous publications that attribute LIF only to molecular PAH [26, 123, 124].

Moving further downstream in the C/O = 0.77 flame (HAB = 8 mm) as shown in Figure 2.1 the second mode of particles emerges. These larger particles exhibit an increase in ELS signal by orders of magnitude [15, 101, 114, 125]. Extinction measurements in this region show absorption into the visible and infrared (IR) wavelengths [30, 88, 101]. These particles, with their increased mass and rigidity, have lost their molecular character such that internal conversion increases and thermal radiation is favoured over fluorescence [43]. Exploiting this, a technique known as Laser-Induced Incandescence (LII) is used extensively to track and characterise these soot particles. Figure 2.1 also highlights that in the downstream region, the distribution of the first mode of particles broadens to include

particles up to around 8 nm. This is indicative of the coalescence process of nanoparticles into larger soot particles [15, 28, 97, 112].

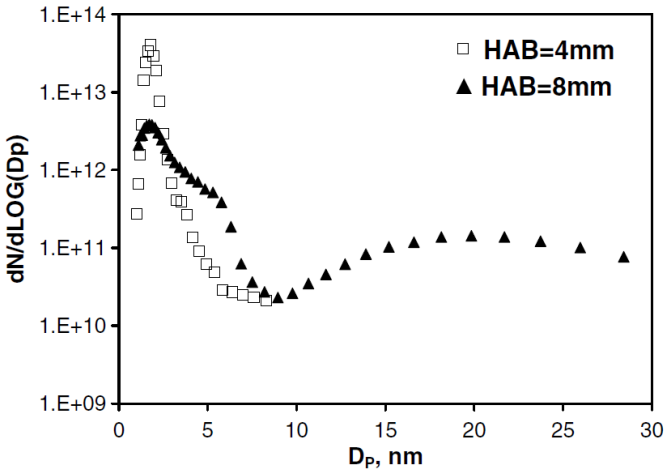

Figure 2.1: Particle size distribution measured via DMA at 4 mm and 8 mm HAB in premixed C/O = 0.77 ethylene/air flame [15].

Particle inception and initial growth is theorised to progress via two key pathways [15]. The first pathway can be considered to be chemically driven, where particles begin to form through polymerisation reactions. PAHs are joined by C-C σ bonds and aliphatic compounds such that constituent PAH that make up these oligomers are distinguishable within branching chains [78, 126]. This pathway is believed to be more active in the presence of oxygen with correspondingly higher temperatures, where high number of radicals facilitate this growth mechanism, i.e. the addition of aromatic radicals to other aromatics [15]. The second pathway relies more on physical interaction of the van der Walls attractive forces between peri-condensed PAHs [50, 77] that begin to stack into graphite like structures, also known as dimerisation. This van der Walls interaction is also responsible for the further coagulation of either of these initial nanostructures into the first primary soot particles. This pathway is favoured in lower temperature pyrolytic and fuel rich flame regions, where radial concentrations are limited. The relative contribution of these two pathways to the inception of soot appears to be strongly dependent upon the combustion conditions [49, 51, 127-129]. Further processes increase the carbonisation of soot particles through dehydrogenation and oxidation reactions.

These two formation processes produce distinctly different nanostructures that can be distinguished between by their measurable properties. Specifically, fluorescence lifetime and spectra have been correlated with the internal structure of the fluorescing species [51, 98]. The chemically driven nanostructures exhibit absorption and emission

akin to that of the constituent PAHs, transparent to visible wavelengths (> 300 nm) [88, 101, 130-134] and fluorescing predominantly in the UV (250 – 450 nm) [51, 113, 121, 131, 134]. These structures tend to be smaller (nominally < 3 nm) and have comparatively shorter decay times (τ) due to the loose chain-like structure. The PAH fluorophores are still able to dissipate energy through non-radiative channels, such as roto-vibrational movements, resulting in short fluorescence lifetimes [33]. On the other hand, nanostructures that favour more stacked configurations exhibit fluorescence in the visible spectrum (400 – 600 nm) [51, 98, 121] and extended fluorescence decay times. When fluorophores are bound within semi-rigid structures they are less able to give roto-vibrational movements and are less able to lose internal energy through non-radiative means, resulting in a longer fluorescence lifetime [51, 130, 135]. Additionally, absorption of these particles shifts to longer wavelengths [122]. While absorption and fluorescence at longer wavelengths may be attributable to PAHs with larger ring numbers [26, 123, 124, 136] grown through the HACA mechanism [28], it is also a consequence of the stacked nature of these particles. Interactions of the π electrons between aromatic islands induce a red-shift of the fluorescence [51]. It is also possible that these stacked nanostructures would have reduced fluorescence quantum yield and dissipate energy via thermal emission as observed by Desgroux et al. [52, 54]. "Nucleation" flames exhibited LII, corresponding to particles between 1 and 6 nm indicating that some nanostructures may lose their molecular quality quickly.

Nanoparticles have been shown to be quasi-spherical when imaged by Transmission electron microscopy (TEM) and atomic force microscopy (AFM) [137-139], but have also been shown to have extreme aspect ratios [140]. However, this is suspected to be consequence the liquid-like nature of these particles [28, 92, 128, 137, 139, 140] and the interaction they have with the mica imaging surface. As nanoparticles begin to coalesce they form the first soot particles that are quasi-spherical [137], while their structure more resembles graphite [42, 95]. During this process, and as these particles grow, internal conversion of absorbed energy becomes the dominant pathway and thus soot particles lose the ability to fluoresce and preferably incandesce. Surface growth also adds to the particle size, where molecular PAH and other small structures condense on the surface of these primary soot particles [30]. Further processes, thermal and chemical, then lead to dehydrogenation [43, 103, 110, 111] and a more graphitic structure as the ratio of aliphatic to aromatic bonds decreases [103, 141]. The age or "maturity" of soot is usually defined their H/C, where nanoparticles can be as high as 0.7 and soot particles can fall as low as 0.05.

Primary soot particles range in size from that of a collection of a few nanostructures up to 50 nm in diameter [28, 41, 116, 142]. From here aggregation of primary particle dominates

the growth process of soot, with the aid of continuing surface growth. Aggregates can become many 100s of nanometres and are better described by a radius of gyration and fractal dimensions rather than a diameter [108, 109]. As soot continues to mature within the flame the graphitic crystallite size increases, becoming more ordered on the soot exterior, while the core remains relatively disordered [40, 143]. However, geometric constraints on PAH layer curvature would prevent concentric layering close to the centre. Finally, soot may be oxidised, particularly at the closing tip of a diffusion flame, when oxygen concentration increases again. Oxidation will then start to reduce the size of the primary particles and aggregates alike and reduce the overall soot volume fraction (SVF) [110]. Although the fuel chemistry is known to play a significant role in the formation, nature and concentration of nanoparticles, if soot is produced, the underlying morphology of soot particles appears to be relatively common regardless of the fuel [109].

Not all the combustion-produced nanoparticles form larger aggregated soot. In fact, they have a very low coagulation rate measured in flames. Thermal rebound of nanoparticles is believed to be a major source of this low ratio between coagulation and collision of particles at flame temperatures [144]. This has been demonstrated by a plateauing of ELS signal that is a result of nanoparticles unable to undergo coagulation [88, 114, 132, 145]. It is this unique behaviour that could explain how these particles bypass exhaust systems [83] and are reluctant to grow to larger soot particles at high temperature [146]. The coagulation rate of nanoparticles is currently described by the balancing van der Waal-interaction energy and the kinetic energy of the particles [145]. The low rate of coagulation may also be due to functional groups containing oxygen. Within the structure of nanoparticles these groups often exist and are believed to greatly influence the coagulation efficiency of the particle [15].

2.2 Experimental Methods

Capabilities to detect soot and nanostructures in reacting flows may be classified into two broad categories: in-situ and ex-situ techniques. In-situ techniques are important for the determination of particle formation kinetics and concentration. Ex-situ techniques alternatively can provide rich information particle structure and morphology. To comprehensively characterise combustion formed particles a combination of in-situ and ex-situ techniques are required [15]. Soot particles and its precursors span a variety of sizes and possess a variety of properties. Nanoparticles display different photo-physical and chemical characteristics than mature soot and consequently require different techniques to detect them.

Very small particles behave similarly to the molecules that make them up. These include spectral qualities like absorption and fluorescence, which can be exploited in both in-situ and ex-situ techniques. Other light interactions, like static and dynamic scattering, from these particles will be in the same order of magnitude as that from gas phase products in which the particles are suspended [15]. Hence, non-intrusive methods of measuring nanometre scale particles rely on absorption, fluorescence and to some extent ELS. Larger particles will display much larger ELS signals and will also incandesce above the flame background upon excitation [15, 43]. A combination of Laser-Induced Fluorescence (LIF), static scattering, and Laser-Induced Incandescence (LII) can be used to determine size and relative concentration of both nanoparticles and soot [41, 42, 51]. These diagnostic techniques are very useful, however, specific information about the measured particles can be difficult to obtain from the data. Often additional data from other techniques is required to calibrate such a system. For example, SVF can be measured through extinction measurements and used to calibrate LII. However, these methods can only provide limited information on particle size distributions, number density and morphology. These details are crucial for modellers as well as developing comprehensive understanding soot formation. Some of these properties can be obtained from ELS TEM and DMA [13, 35, 41, 42, 107, 142, 147-153].

In-situ and ex-situ techniques possess their own advantages and disadvantages which will be discussed in the following subsections.

2.2.1 Ex-situ Methods

Ex-situ techniques used to sample flames require extraction of particles and gas-phase products and reactants. This allows careful and detailed measurements on the sample due the controlled environment that can be maintained. Particle size and distribution measurements that are vitally important can be performed using methods such as mass spectrometry (MS), TEM, AFM and DMA.

Although Ex-situ measurements provide very useful information, they are not without shortcomings. For example, the Differential Mobility Analyser technique [13, 35-39] involves the use of horizontal and vertical suction probes to withdraw particles from the combustion environment. Alternatively, particle probing can be performed through thermophoretic sampling onto a specialised substrate to be further analysed by TEM [40-42], Atomic Force Microscopy [100, 140, 145] or Raman [23, 85, 154]. One disadvantage of these ex-situ techniques is the inevitable perturbation by the physical probe, and the disruption this has on the local flow field and temperature [97, 155, 156]. Additionally, sampling techniques can suffer from saturation, where too many particles saturate the

detection device such that it is difficult to distinguish individual contributors or in the case of ionising processes, the device does not have the capacity to ionise all the relevant products that are being sampled [29]. To combat this, samples are usually diluted and cooled to prevent further reactions. However, the final measured sample may differ from that originally existent in the flame as gas phase and particles can coagulate and condensate on each other or on the walls of the device. Probing measurements also have limited capability in turbulent flames. The extraction process takes time to build up samples, much longer than inherent fluctuations in turbulent flames. Measurements are still taken in turbulent flames, but represent a time-averaged sample [157-159]. Never the less, ex-situ techniques remain extremely valuable and continue to be used to track the evolution of nanostructures in a wide range of flames [22, 97, 155].

Differential Mobility Analysis

Differential Mobility analysis (DMA) has recently become an important tool in identifying sub 10 nm particles. Particles are sampled from the flame location via probe, generally horizontally, with an entrance pinhole in the order of a few hundred microns. However, larger pinholes of 0.8 mm have been used for sooting flames to prevent clogging [22, 112]. A vacuum pump supplies constant suction for the probe while the sampled gas and material are also diluted with nitrogen. This dilution aims to prevent further chemical reactions in the sampling device and limits coagulation and condensation of particles and gas phase species. A secondary dilution prior to the sample entrance to the differential analyser is also required. Suction probes like this obviously perturbate the flame and have been shown to reduce the temperature locally and downstream, although, the impacts on the measured particle size distributions (PSD) appears to be marginal [36].

The differential mobility analyser assesses the mobility of charged particles within an electric filed. The particles entering the analyser are charged using radioactive source such that have a Fuchs equilibrium charge distribution [160]. These charged particles then pass through the electric field, maintained between two high voltage electrodes. Here positively charged particles are attracted to the negatively charged collector rod. Where the particles land depends on the particles electric mobility, fluid flowrate and the internal geometry of the analyser. A particle counter is used to determine number concentration. Stoke's law, see [161] for more detail, has been traditionally used for determining the mobility diameter of particles (d_p), however, this on its own has proven insufficient for size determination of quasi-spherical carbonaceous particles. Singh et al. [71] proposed the following relationship between the diameter measured by the analyser and the actual carbonaceous particle, Equation 2.5.

$$\frac{d_{p,actual}}{d_{p,measured}} = \tanh(1.4334 + 0.01248 d_{p,measured})(1.0676 - \frac{0.4463}{d_{p,measured}}) \quad (2.5)$$

Nano-DMA devices have been used extensively to identify both nanoparticles and soot [13, 35-39]. It is established that, compared to soot, the number density of nanostructures/nanoparticles is more than an order of magnitude higher while their contribution to the total mass concentration is negligible [15] and can be seen in Figure 2.1.

2.2.2 In-situ Methods

In-situ techniques do not have the same capacity to provide quantitative data that ex-situ techniques do. Quantitative measurements are possible but often require careful calibration usually obtained through ex-situ techniques or complex models. In-situ techniques can, however, provide pertinent information on soot formation within flames. As discussed above ex-situ techniques suffer from a number of shortcomings some of which are overcome by in-situ techniques. Laser-based measurements are non-invasive by allowing observation of the flame as it exists without concern of changing the conditions by the physical act of sampling. By exploiting the rich interaction of light with particles, the presence, size, concentration and morphology of soot have been investigated using optical processes such as absorption, scattering, fluorescence and incandescence in a wide range of combustion systems [15, 29, 32-34, 87, 162-164].

In-situ techniques are not without drawbacks. By measuring directly in the flame, there is no way to separate the individual constituents within the probe volume. For example, probing for fluorescent properties of PAH will also return incandescent and scattering signals. Subtraction of signals and appropriate calibration can mitigate this, only if all sources of returned signal are known [50, 51]. Due to this, a certain amount of uncertainty is involved when extracting quantitative results from in-situ measurements.

Pertinent to this thesis, a big advantage of laser-based in-situ techniques are their suitability for turbulent flame measurements. Additionally, these techniques have the capacity for high spatial and temporal resolution, making them more suited for the detection of nanostructures and soot agglomerates in turbulent flames [29, 99]. The inhomogeneous and intermittent nature of turbulent combustion is an important variable to observe as it an inherent in many practical combustion devices.

Elastic Light Scattering

Elastic light scattering (ELS) technique relies on the ability of molecules and particles alike to scatter light. ELS can be an intended or unintended feature of any laser-based measurement. For molecular species and small spheroids ELS is best described by the Rayleigh approximation. The Rayleigh approximation for scattered light holds true when the object being measured is smaller than the wavelength of light ($d_p << \lambda$). The magnitude of ELS is also a function of wavelength such that, the smaller the wavelength the greater the degree of scattering. Equation 2.6 defines the Rayleigh approximation ELS intensity (Q_{vv} with *vv* corresponding to vertical polarisation for both incident light and the detected light) as also a function of particle size (d_i), number of particles (N_i) and the particles complex index of refraction (m). This Equation highlights the strong sensitivity ESL has to particle diameter ($Q_{vv} \propto d^6$), and hence ELS measurements have been used in combination with other techniques to infer particle size and volume fraction [99, 125, 148, 151, 165-167]. Without calibration, comparing ELS with other measurements that are indicative of volume fraction, such as LII, allows inference of changes in average particle size. Determination of average particle size is skewed towards the largest particles within the sample, due to the proportionality to d^6. The Rayleigh approximation is appropriate for gas phase and nanostructures, even at UV wavelengths, given the absorption spectra of PAH and nanoparticles. Absorption in the UV can be attributed to a number of other compounds that are present in the gas phase. At high temperatures CO_2 and H_2O are known to absorb UV light, but typically at wavelengths below 230 nm [26, 168].

$$Q_{vv} = \frac{\pi^4}{4\lambda^4} \sum \left| \frac{m_i^2 - 1}{m_i^2 + 2} \right| N_i d_i^6 \qquad (2.6)$$

As particles get larger as is the case with soot and soot aggregates, the Rayleigh approximation no longer holds. In this regime ($d_p \sim \lambda$), Debye or Mie scattering would be more appropriate, if one cannot use incident light at larger wavelengths. However, because soot aggregates are also non-spherical other approximations are generally used. The Rayleigh–Debye–Gans approximation has been used, among others approximations to deal with soot aggregates [30].

Laser-Induced Incandescence

Laser-Induced Incandescence (LII) is a workhorse for particulate measurements in a variety of fields and has broad application when combined with complementary methods such as scattering and probe measurements [43]. The optical properties of soot make it suitable for LII measurements. Soot absorbs strongly in a broad wavelength range from the

UV into IR. Mature soot is also a refractory material with a sublimation point, about 4000 K, well above the flame temperatures in many conditions [43].

The principle of this technique is to heat up the soot particles to a temperature high enough to emit measurable quasi-blackbody radiation at temperatures well above the background temperature of the flame. This is achieved with a high-power pulsed laser that is absorbed by the soot allowing it to subsequently thermally radiate.

Interpreting LII quasi-blackbody radiation is a problem of energy and mass balance. The known contributors to this balance as identified in Equations 2.7 and 2.8 for the energy and mass balance respectively [43, 169]. Where U_{int} is the internal energy of the particle, t represents time, $\dot{Q}_{abs}$ is the absorptive-heating rate for a single primary particle, $\dot{Q}_{rad}$ is the radiative-cooling rate, $\dot{Q}_{cond}$ is the conductive-cooling rate, $\dot{Q}_{sub}$ is the evaporative-cooling rate, $\dot{Q}_{ox}$ is the oxidative heating rate, $\dot{Q}_{ann}$ is the heating rate from annealing, and $\dot{Q}_{therm}$ is the thermionic cooling rate. The mass balance is only practically impacted by sublimation and oxidation as seen in Equation 2.8, where M is mass of particle. An in-depth description is not provided here on each of these contributing process, the reader is advised to see [43] for more detail. During the very short period that particles are heated by the laser and measured for their radiation, it is assumed that they would otherwise have been in equilibrium in the flame. During the laser pulse the particle begins to heat up as some of the laser energy is absorbed ($\dot{Q}_{abs}$), increasing the particles internal energy (U_{int}). The particle reaches its maximum temperature toward the end of the laser pulse where a number of processes attempt to bring the particle back into thermal equilibrium. The major contributors to the energy balance are $\dot{Q}_{abs}$, $\dot{Q}_{cond}$, $\dot{Q}_{sub}$ and to a lesser extent $\dot{Q}_{rad}$. As for the mass balance, this is generally modelled by sublimation only ($\dot{Q}_{sub}$). The rest of the components are generally omitted in LII models due to their limited impact or unknown nature.

$$\frac{dU_{int}}{dt} = \dot{Q}_{abs} + \dot{Q}_{rad} + \dot{Q}_{cond} + \dot{Q}_{sub} + \dot{Q}_{ox} + \dot{Q}_{ann} + \dot{Q}_{therm} \tag{2.7}$$

$$\frac{dM}{dt} = \left(\frac{dM}{dt}\right)_{sub} + \left(\frac{dM}{dt}\right)_{ox} \tag{2.8}$$

The quasi-blackbody radiative emission ($\dot{Q}_{rad}$) is the signal that is collected in LII measurements. This signal ($S(\lambda)$) is temperature and wavelength dependent as dictated by Planck's law adapted for Equation 2.9. Where ε_λ is the emissivity, h is the Planck constant, c is the speed of light, k_B is the Boltzmann constant, λ is the emission wavelength and T is the temperature of the particle. The emissivity ($\varepsilon_\lambda(\lambda,m)$) describes the deviation of emission from a perfect blackbody for particles with a diameter in the Rayleigh approximation ($d_p \ll \lambda$). Various definitions of emissivity are available in the literature [45, 170-172].

Because *S* is a function of both temperature and wavelength and if measurements are taken over at least two separate wavelengths, or bands, then LII temperature can be determined. This is only true for temporally resolved signals as the temperature changes rapidly in these measurements. Although radiation is one of the mechanisms for cooling the soot, it is not as dominating as conduction ($\dot{Q}_{cond}$).

$$S(\lambda) = \varepsilon_\lambda(\lambda, m) \frac{2\pi^2 d_p^2 hc^2}{\lambda^5 \left[e^{\left(\frac{hc}{\lambda k_B T}\right)} - 1 \right]} \tag{2.9}$$

Conductive cooling ($\dot{Q}_{cond}$) at atmospheric and greater pressures accounts for the majority of the exponential decay in the LII signal, in the case where laser fluences are not high enough to induce substantial sublimation mass loss. $\dot{Q}_{cond}$ is described by Equation 2.10 and is a function of the temperature difference of the particle to the surrounding bath gas. Where p_0 is the bath pressure, T_0 is the bath temperature, R is the universal gas constant, W_a is the molecular weight of air, C_p is the heat capacity of air at constant pressure and α_T is the thermal accommodation coefficient.

$$\dot{Q}_{cond} = \frac{-\pi d_p^2 \alpha_T p_0}{RT_0} \sqrt{\frac{RT_0}{2\pi W_a}} \left(C_p - \frac{R}{2} \right) (T - T_0) \tag{2.10}$$

The above expressions become a little more complex when particle size and mass is not considered constant during these processes. Particle sublimation ($\dot{Q}_{sub}$) begins to influence the LII signal once laser fluences exceed around 0.3 J/cm^2 for 1064 nm laser pulses. At and above these fluences particle temperatures approach and surpass the expected sublimation temperature of soot, which is around 4000 K. Heat and mass is thus lost from the particle in the form of vaporised carbon clusters, including C_2 and C_3 that are known to have excited emission bands in the visible. An initial decrease in signal is approximately contained within the laser pulse duration as is expected as sublimation processes will drop significantly as the particle temperature falls below the sublimation temperature. After the laser pulse the enduring signal remains dominated by conductive cooling. Choosing the correct laser fluence is a trade-off of signal magnitude versus its impact on the particle size and morphology and the resultant signal interpretation.

A laser wavelength of 1064 nm is generally preferred for selective measurement of solid particles as longer wavelengths are not absorbed by most gaseous and condensed phase species in combustion. For lasers with top hat spatial profiles the LII signal increases with increasing fluence levels up to a point where it plateaus around 0.5 J/cm^2 before decreasing again towards 10 J/cm^2 [173] for 1064 nm as seen in Figure 2.2. It is deemed good practice to operate in this plateau region in heavily sooting flames to minimise the impact of beam attenuation as it travels through other areas of the flame [29]. Although mass loss does

occur, it has a marginal impact on determination of SVF [149, 150]. For Gaussian spatial beam profiles there are less defined features in the LII vs. fluence curve. This is a consequence of the fluence variation along the Gaussian profile, i.e. the centre of the Gaussian beam has a higher fluence than the wings. Consequently, any decrease or plateauing of signal of the LII signal in the centre of the beam due to high fluences is compensated by an increase in wing area that exists at intermediate fluence levels [43, 174]. Because of this variation in laser fluence, when using a Gaussian profile, particle sizing becomes more challenging, although has little impact on determination of SVF of pointwise or spatially integrated measurements [175].

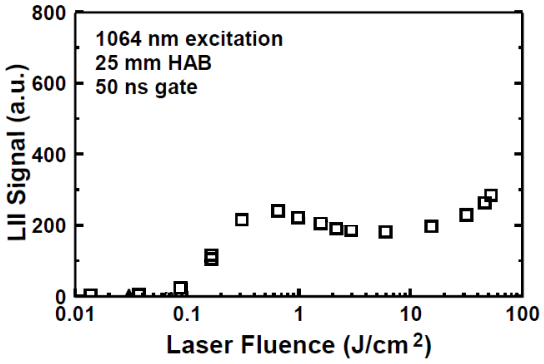

Figure 2.2: LII signal intensity against 1064 nm laser fluence recorded at 650 nm [173].

When breaching the sublimation threshold, ejection and excitation of C_2 and C_3 radicals can be problematic due to their own spectral emission. Irradiation at 1064 nm requires high fluences (> 0.5 J/cm^2) before any faint spectral features of C_2 and C_3 are seen in the broadband quasi-blackbody spectrum [176]. Visible wavelengths and lower such as 532 nm require much lower fluences (> 0.25 J/cm^2) before these features are visible and significant [176-178]. Laser wavelength deep in the UV have the energy to overcome the sigma bonds between carbon atoms and thus may preferentially induce mass loss by photodissociation from the soot surface rather than vaporising by means of reaching high temperatures [179, 180]. A number of studies using laser wavelengths of 193 nm have shown substantial mass loss and particle disintegration at modest fluences of 193 nm light [179-181]. This photodissociation does not occur using slightly longer wavelengths such as 213 nm and greater where LII has been observed [41, 99, 116, 124, 182]. Shorter wavelengths have a much higher propensity to excite fluorescing species within the flame compared to 532 nm and 1064 nm [183]. However, using UV wavelengths has proven advantageous in probing aromatic species and nanostructures [50, 51, 99, 122, 184].

Broadband fluorescence peaking between 300 and 400 nm has been attributed to these species.

Laser-Induced Fluorescence

Fluorescence is the phenomenon of almost immediate light emission after excitation of a molecule. Laser-Induced Fluorescence (LIF) uses a pulsed laser, much like LII measurements, as the excitation source, where the incident light, often in the UV, is absorbed by the molecule. Unlike ELS, the emission process is measurably longer than the absorption, although still happens only in a number of picoseconds or nanoseconds. When an incident photon is absorbed, an electron is promoted from the "ground state" to a higher energy state known as an "excited state". Due to the nature of quantum mechanics, these electronic excited states are quantised which restricts the absorption of light to specific wavelengths. Although, the absorption spectrum is broadened due to the sublevel states of vibrational and rotational energy that exist within electronic states. These specific states are most commonly illustrated on a Jablonski diagram. Within flames, due to the elevated temperatures and many species that co-exist, the absorption spectrum is broad [29] and without strong features to identify individual contributors. As discussed earlier, the absorption in the UV (< 300 nm) is attributed to aromatic species [26, 29, 88, 101, 130-134].

For the molecule to return to the ground state, it undergoes three following generalised sequential processes. (1) The molecule moves to the minimum free energy state (lowest vibration sublevel) of the higher electronic state. (2) The electron returns to the ground electronic state. This step is where the fluorescence emission occurs, but there are also other competing mechanisms to dissipate the energy that would not result in photon emission. (3) The final relaxation of the molecule from higher energy vibrational or rotational states within the electronic ground state until equilibrium is reached with the surrounding molecules. As a consequence of these intermediate steps, the energy released via florescence is usually less than that absorbed resulting in the emission wavelength being longer than the absorbed wavelength. The quantisation of the energy levels is also responsible for the emission being confined to specific wavelengths.

Fluorescence of an excited molecule is not guaranteed, it has a probability balanced against other non-radiative processes, such as internal conversion, quenching and intersystem crossing. For more detail on these processes and fluorescence in general the reader is advised to see [135, 136]. Each of these processes have their own rate constants (k) that dictate the how and when the energy is dissipated. Each excited molecule only has the potential to release one photon, however, a collection of excited molecules will exhibit a

temporal distribution of this emission, known as fluorescence lifetime (τ). The fluorescence lifetime, can also be considered as the excited lifetime of the molecule and measuring the fluorescence is convenient way to observe this. Thus, fluorescence lifetime is a function of all the contributing rate constants as seen in Equation 2.11. The emission intensity (I_E) of a collection of fluorescing species is generally expressed as a single exponential decay as seen in Equation 2.12, where *A* is the initial intensity and *t* is time.

$$\tau = 1/\sum k_i \tag{2.11}$$

$$I_E = Ae^{-t/\tau} \tag{2.12}$$

Because absorption occurs in the order of femtoseconds and typical laser excitation sources are much longer, in the order of picoseconds and nanoseconds, the observed fluorescence signal is not a simple exponential function. The recorded signal (I_R) becomes a convolution of the laser pulse function and the measuring equipment as seen in Equation 2.13. Often it is either the laser pulse or the limited response of the collection equipment that becomes the limiting system response (I_S). To extract the actual decay function from the recorded signal, a deconvolution process is required [51, 117]. Signal convolution also occurs for LII and a similar deconvolution procedure is required for soot particle size estimations.

$$I_R(t) = I_S * I_E = \int_{-\infty}^{\infty} I_S(x) I_E(t-x) dx \tag{2.13}$$

There are many factors that impact the fluorescence yield of fluorophores beyond their intrinsic rate constants. For example, pressure and temperature have large impact on concentration and the rate of collisions with quenching species. Ossler et al. [117] showed that gas phase PAH fluorescence lifetimes dramatically reduce with increasing temperature and also induces a slight redshift in the spectrum. Some broadening of the spectrum was also observed by Chi et al. [185] with increasing temperature. Whilst fluorescence is generally associated as a molecular phenomenon, molecules within larger structures still fluoresce. However, when fluorophores are bound within semi-rigid structures they are less able to give roto-vibrational movements and are less able to lose internal energy through non-radiative means, resulting in a longer fluorescence lifetime [51, 130, 135]. If the relationship between the fluorophore and other factors can be accounted for, some inferences on the particle structure can be made.

The fluorescence spectrum and lifetimes can be used as guide to identify physical and chemical changes in the nanostructure and its environment. In the presence of oxygen (a known fluorescence quenching species), the higher temperature increases the effectiveness of vibrational pathways in fluorophores and keep fluorescence lifetimes low, particularly in aliphatic linked structures that allow many degrees of freedom,

that favour non-radiative pathways. Conversely in pyrolytic conditions, where temperature is generally lower, radiative pathways are enhanced due to more ridged stacked structure of particles formed here that don't allow the same vibration freedom, resulting in longer fluorescence lifetimes [34, 51, 130, 135]. PAH are known to fluoresce primarily in the UV -Visible spectrum (250 – 450nm) as discussed earlier [26, 117, 185] with longer fluorescence wavelengths attributable to larger PAH species with more rings. While fluorescence emission spectrum generally increases with the size of the aromatic island (number of rings) [34, 48, 123, 124, 130, 136], fluorescence spectrums peaking at wavelengths above 450 nm are difficult to attribute to the corresponding PAH sizes larger than coronene as their relative concentration in flames is quite low compared to smaller PAH species [66, 67]. A redshifted spectrum can also be associated with evolution of the structure of the nanoparticle towards a more stacked arrangement. In summary, a redshift and increase in fluorescent lifetime is indicative of nanostructure growth favouring physical dimerisation, whilst bluer spectrums and shorter/constant lifetimes indicate growth through chemical polymerisation.

Fluorescence intensity for molecular species, in controlled environments, is known to be proportional to the concentration, provided the optical density remains small enough to avoid reabsorption effects [135].The same can also be said for fluorescent nanostructures within non-sooting premixed flames [98]. Fluorescence intensity in these flames is found to correlate linearly with UV absorption and light scattering coefficients that already correlated with NOC concentrations. In premixed flames, the temperature remains relatively constant downstream of the flame front and particle evolution is curtailed as coagulation is limited in low concentrations. Extending this conclusion to other conditions is challenging, such as in diffusion flames where temperature is changing along with particle evolution. However, fluorescence cross-section and quantum yield should vary sensibly along the flame [184]. In fact, in high temperature (> 1300 K) regions in counter-flow diffusion flames, the concentration of two classes of nanostructures determined by sectional model approach showed good correlation with measured LIF intensities [50]. Such a correlation also exists among a range of sooting and non-sooting premixed flames [186].

Time-resolved fluorescence polarisation anisotropy (TRFPA) provides an even more robust way to assess the source of fluorescence. This technique exploits the fact that fluorophores preferentially absorb photons whose electric field is parallel with orientation of the molecule's transition dipole. Since absorption happens relatively instantly the molecule or larger structure has not had time to shift its orientation, however, during the fluorescence process it does. The emitted photon is also preferentially polarised with respect to the molecule. Consequently, the prompt fluorescence emission is relatively

polarised, while later emission's polarisation becomes scrambled due to rotational diffusion. The rate of depolarisation can then be used to infer particle size [1, 98, 118-122, 184, 187]. Fluorescing particle sizes from 1 to 20 nm have been identified both in-situ and ex-situ of premixed and diffusion flames using this method.

Thermocouple

Thermocouple temperature measurements are intrusive in-situ measurements and do perturbate the flame to some extent as a thermocouple bead is placed within the flow. However, thermocouple measurements provide valuable data required for the interpretation of other in-situ measurements. A thermocouple consists of two dissimilar metals whose voltage difference under a thermal gradient are dissimilar. This potential difference is then measured and correlated with temperature. Platinum/rhodium-alloy thermocouples are often used in combustion measurements as they are suitable in high temperatures. Determining the temperature of the flow is then an energy balance problem as seen in Equation 2.14. Convective heat transfer is responsible for heating the thermocouple bead close to the gas temperature, while conduction through the wires and radiate loss from the bead often prevent the thermocouple reaching the gas temperature. Losses through conduction can be reduced by exposing more of the wire to the combustion environment under the assumption that temperature gradients are not strong in the probe volume [188]. Additional uncertainty can be due to catalytic effects, where the bead itself is responsible for enhanced reactions taking place on the surface that artificially increase the local temperature and that measured by the probe. This can be mitigated by the use of coatings [189].

$$Q_{conduction} + Q_{convection} + Q_{radiation} + Q_{catalytic} = 0 \qquad (2.14)$$

Thermocouple measurements in sooting flames further complicates the energy balance equations due to particle deposition of the thermocouple bead. This changes the diameter, roughness and emissivity of the bead. However, by measuring the temperature-time history it is possible to extract values for the emissivity of the particles within the flame through a technique called thermocouple particle densitometry (TPD) [190-192]. These measurements have further highlighted the difference in spectroscopic properties of particles formed early in the flame compared to soot.

Thermocouples have thermal inertia that does not allow them to faithfully track fluctuations in gas temperature, such as those in turbulent flames. Whilst temporally resolved thermocouple measurements have been conducted in turbulent flames with compensations made for this thermal inertia, they are more suited to time-averaged temperature measurements.

2.3 Modelling

Many experimental measurements of soot and its formation are used to inform or validate various computational models, particularly measurements in laboratory flames that focus on fundamental characteristics of combustion. These models range from those focused on fundamental flame structure, species and soot formation [27, 50, 69, 77, 79, 80, 186, 193] to models attempting to capture more practical combustion [58, 82, 194-196]. Modelling is not a focus of this thesis and thus only a brief overview will be given here, as it is a very involved and active area of research on its own. It does, however, provide some additional context for the measurements presented in this thesis.

The coupling of fluid dynamics and chemical kinetics becomes more complex with the addition of mechanisms for the formation of the first PAHs and ultimately the interaction of the gas phase with solid and condensed phase species, as is the case with soot formation. Withstanding the fact that the formation mechanisms are not yet well defined, it is currently computationally infeasible to model all PAH isomer and nanostructure variations and accurately represent their populations. For this reason, simplification of these processes through soot models are used to capture the important features of soot within simulations, such as SVF and PSD. There are two general types of soot models used to address this problem; (1) Sectional Method (SM) [70, 72, 80, 81, 127, 191, 197-199] and (2) Method of Moments (MM) [58, 82, 194, 195].

Sectional method discretises aromatic compounds/particles formed into separate bins (or sections) based on molecular mass. Additional section dimensions such as H/C ratio are also used to further characterise particles and further define the interaction with the gas phase [81]. The output (PSD, SVF, etc.) of SM models is subject only to the model defined gas phase reactions and physical interactions (coagulation, aggregation) as SMs are directly coupled with the gas phase kinetics. SMs are generally able to provide a greater depth of information on the predicted particle distributions, extending from mass and size properties to include chemical composition and morphology. This, however, comes at a computational cost as a large number of sections are needed to adequately represent the continuous PSD and such SM models are generally limited to modelling simpler cases.

Method of moments models consider a continuous PSD which can be defined by its moments, as opposed to a numerical solution. The first four moments of a distribution are representative of the distribution mean, variance, skewness and kurtosis respectively. Knowledge of the infinite moments would allow for a fully defined PSD. A description of the first few moments is generally sufficient to define such properties volume fraction, mean particle size and variance. However, some assumptions about the functional form of

the PSD need to be made, such as its bimodality, which are generally informed by experimental measurements. The MM approach is less computationally intensive compared to the SM, as the PSD is defined only by a relative few equations relating to the first few moments. These models thus lend themselves to more complex combustion conditions including turbulent flames [58, 82, 194, 195].

In recent years there have been large improvements in these models' ability to predict soot formation in a variety of combustion conditions. Advancements in these models and providing experimental data for validation is a key focus of the International Sooting Flame (ISF) workshop [200].

Chapter 3: Methodology

As stated in the introduction, the objective of this thesis is to develop an improved understanding of the inception processes related to nanoparticles. For this purpose, three flame configurations are investigated: (1) premixed laminar flames, (2) laminar diffusion flames and (3) a turbulent diffusion flame. Combined LIF, LII and scattering technique is applied to all of these cases. This Chapter gives a description of the flames studied and the diagnostic methods employed.

3.1 Optical Setup

Temporally resolved LIE was the main event of this work. The experimental setup exploits the spectroscopic properties of PAH, nanoparticles and soot in laboratory flames. The setup includes two pulsed lasers and a custom designed spectrometer along with applicable laser and collection optics. The technique is similar to that seen in previous works [49, 50, 113, 198, 201, 202], however, there are some important differences that extend this technique over others.

3.1.1 Lasers and Timing

Two pulsed lasers were used for excitation of combustion formed particles. The first was an Ekspla PL2251 Series Laser, while the second was a Spectra Physics Quanta-Ray Pro-350 Series Laser. The Ekspla is a pulsed picosecond Nd: YAG laser, running at 10 Hz. The P80 echelon was placed within the resonance chamber to achieve a full width at half maximum (FWHM) pulse length of 80 ps. Although initially a pulse length of 30 ps was trialled, the 80 ps pulse was preferred as it reduced the likelihood of multiphoton processes

occurring in the probe volume, while not compromising the temporal resolution of the measurements. A pulse length in the order of tens of picoseconds was necessary to properly observe fast temporal evolution of LIF. The fundamental output of this laser is at a wavelength of 1064 nm. In the current work, the 2nd and 4th harmonic crystals were also installed to convert the output to 266 nm. As discussed in Chapter 2 to probe PAH and nanoparticles consisting of PAH an excitation source in the UV is required, hence the choice of 266 nm for excitation. The Primary purpose of the 266 nm pulse was for LIF and ELS measurements. Although LII was expected and was observed from larger particles after absorbing the 266 nm pulse it was difficult to separate contributions of LIF and LII from each other in the measurements. For this reason, a second laser probe was used; The Quanta Ray laser is also a 10 Hz Nd:YAG with a fundamental output of 1064 nm and FWHM pulse duration of 8 ns. The fundamental, 1064 nm, output was used to exclusively excite larger soot particles, as precursor molecules and nanostructures are known not to absorb in the infrared. The Quanta Ray laser is non-seeded, which is known to provide some challenges in LII measurements due to the shot to shot variability and uneven heating [43, 203]. The maximum shot to shot variability from the Quanta ray was less than 40% (peak intensity), much less than that experienced by Goulay et al. [203]. Whilst this variability can impact size determination based of LII decay times, the impact on LII temporal peak intensity when operating at or below 0.6 J/cm^2 remains negligible. Unless otherwise stated LII measurements presented in this thesis refer to 1064 nm LII.

Both lasers are focused for pointwise measurements, overlapping in space but temporally separated. The 266 nm Ekspla laser arrives first primarily for LIF measurements, with the 1064 nm Quanta Ray laser arriving up to 100s of nanoseconds later exclusively for LII measurements. The exact temporal separation between these two pulses varied from experiment to experiment as adjustments were made and potential interactions between the sources were identified. The specific timing used for each study will be detailed in the setup sections of the relevant Chapters along with discussion on these interactions. Figure 3.1 is a conceptual diagram highlighting the temporal separation of the two laser pulses. The 266 nm pulse arrives first resulting in the emission of LIF, followed by the arrival of the 1064 nm pulse. The relatively short LIF signal from the 266 nm pulse has time to decay to negligible intensity and not interfere with the proceeding LII from the 1064 nm pulse. The timing of these two lasers was achieved by a SRS DG535 digital delay generator that provided minimal jitter (< 1 ns) between pulses.

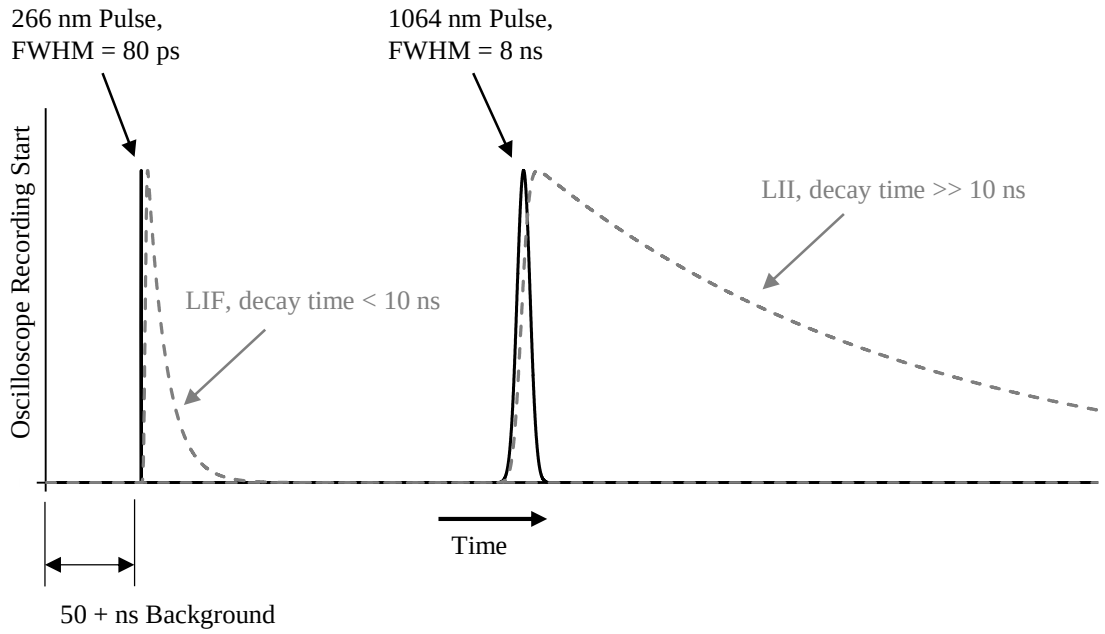

Figure 3.1: Conceptual diagram of laser pulses and LIE temporal separation.

In steady, laminar conditions measurements at 266 nm and 1064 nm could be made separately or combined. However, this is not possible for turbulent flames where joint, time-resolved measurements are essential and this is an objective of this work. The velocities in the turbulent flames investigated in Chapter 7 are such the packet of gas passing through the probe volume will not have moved significantly within a few microseconds. Hence the two laser pulses can be separated by microseconds and the two measurements (266 nm and 1064 nm) can still be considered simultaneous.

3.1.2 Laser Optics

Both lasers are directed and focused to the probe volume through a series of mirrors and lenses as seen in Figure 3.2. The Ekspla 266 nm pulse first is reflected around a loop of UV coated mirrors (Lattice Electro Optics, Inc. RX-266-45-UF-2038) to bleed off any residual 1064 nm or 532 nm component of the pulse from the frequency doubling and quadrupling procedure. The 266 nm pulse is then directed to the probe volume at a shallow angle of 6.85° with respect to the 1064 nm pulse from the Quanta Ray. The laser energy was controlled using a combination of a half-wave plate (Lattice Electro Optics, Inc. CWO-266-02-08-R10) and a polarisation cube (Lattice Electro Optics, Inc. PBU-266-100). The half-wave plate allows the adjustment of the linear polarisation direction of the laser, while

the polarisation cube siphons off only the component of the beam in the parallel polarisation. This allowed for fine control of the laser energy to ensure consistency between studies. The 266 nm laser was then focused using a 500 mm focal length UV coated plano-convex lens (Lattice Electro Optics, Inc. UF-PX-50.8-500-266). The Gaussian beam was focused from 12 mm diameter to a point at the probe volume, where the converged beam diameter was measured to be 250 µm. The laser energy per pulse was measured between the focusing lens and the probe volume using an energy detector head (Newport® 811E10-25-F) connected to a Gentec-EO MAESTRO power meter. The resultant fluence measured at the probe volume for the majority of studies presented here was around 1.2 J/cm^2 and achieved a RMS stability less than 1%. The specific fluence for each study will be detailed in the relevant Chapters. Not detailed in Figure 3.2 are a few irises and beam dumps that remove unwanted reflections of the 266 nm beam.

Figure 3.2 also depicts the laser path of the 1064 nm Quanta Ray laser. The normal output energy range of the Quanta Ray was very excessive for the pointwise LII measurements, more than 2.5 J/pulse. To maintain stability the laser needed to be run at its peak output, so the beam was substantially attenuated before reaching the probe volume. This was achieved by reflecting the vast majority of the 1064 nm beam into a beam dump and taking the bleed through of the first mirror (Lattice Electro Optics, Inc. RX-1064-45-B-2038) as the useful part of the beam. This residual beam is not likely to have a pure polarisation; however, this is of no consequence for the LII measurements presented here. Before the beam was focused, it passed through a half-wave plate (Lattice Electro Optics, Inc. CWO-1064-02-10) and a thin film polariser (Lattice Electro Optics, Inc. TP-1064-B-2025). The half-wave plate and thin film polariser served the same purpose as it did with the 266 nm beam; ability to precisely attenuate the laser energy. The 1064 nm laser was then focused using a 300 mm focal length IR suitable plano-convex lens (Lattice Electro Optics, Inc. B-PX-50.8-300). The super-Gaussian beam was focused from 12 mm diameter to a point at the probe volume, where the converged beam diameter was measured to be 450 µm. The laser energy was measured in the same way as 266 nm. The fluence for the 1064 nm laser pulse was set to 0.6 J/cm^2 and achieved a RMS stability less than 1%. This fluence maximises signal, while keeping effects of soot mass loss due to surface soot sublimation relatively low [43, 173, 174].

The beam sizes at the focal point (probe volume) was measured using a scanning edge (also known as knife edge) technique. These measurements were in agreement with microscopic images of the laser burn marks taken on photosensitive paper.

To ensure that both lasers passed through the same volume at their focus, a fully closing iris was placed centred at this location. Both lasers we aligned and focused through this iris to achieve good overlap. Further precision was achieved by imaging the two lasers with

photosensitive paper at the probe volume. The precision of this technique was determined to be < 100 µm distance between the centres of the focused beams at the probe volume. After the lasers pass the probe volume they are then terminated in a pair of beam dumps. The fluences used and the spatial overlap of the two lasers have the potential to influence the LIF and LII measurements. These interactions are handled specifically in the following Chapters where relevant.

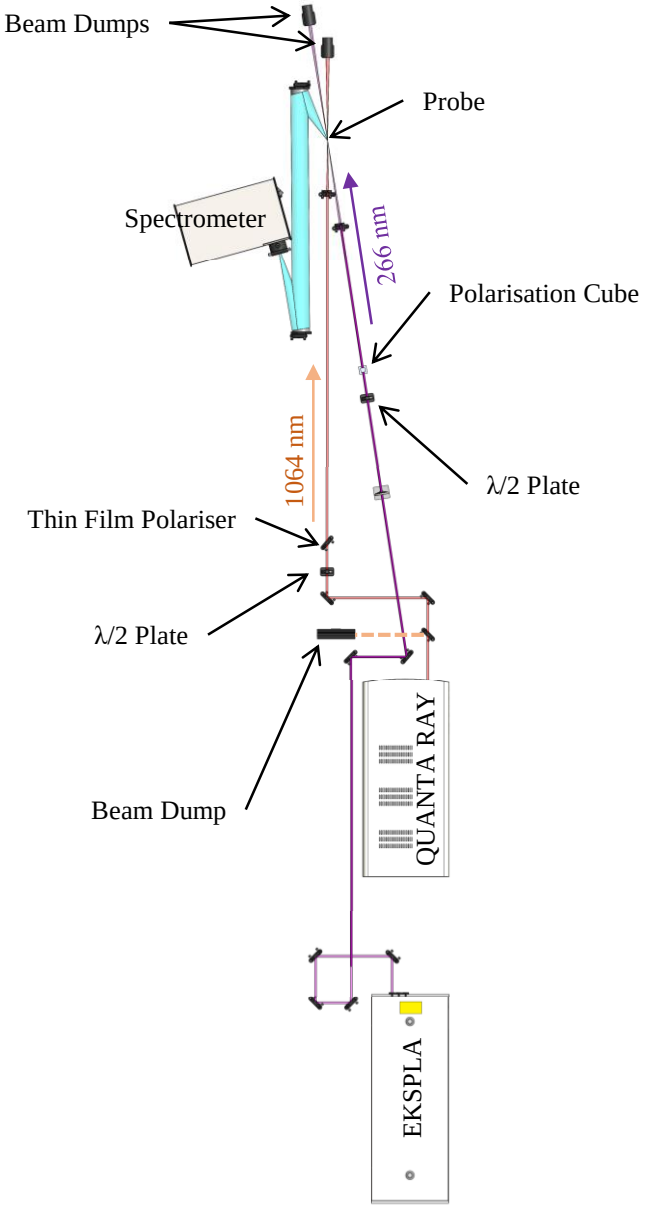

Figure 3.2: Top view schematic of laser optic setup.

3.1.3 Light Collection

The LIE from both the 266 nm laser and the 1064 nm laser are collected for spectral measurements within a custom-built spectrometer. Light emitted from the probe volume is guided onto the spectrometer slit using two large diameter off-axis (OA) aluminium parabolic mirrors as seen in Figure 3.3. The mirrors are 101.6 mm in diameter and achieve a low collection *f-number* to maximise the collected signal. The choice of aluminium parabolic mirrors was also driven by the need to avoid spherical aberration to maximise the spatial resolution and avoid chromatic aberration as the collected light spans a broad spectrum from the UV into the visible. The mirror focused on the probe volume (Edmund Optics, Inc. #83-967) is a 30° off-axis with a parent focal length of 300mm. This mirror collects LIE signals from behind the probe volume with respect to the direction of the laser pulses. The second mirror (Edmund Optics, Inc. #83-959) is 15° off-axis parabolic with a parent focal length of 500 mm. This was necessary to match the spectrometer focal length. This combination provides an atypical collection angle, but was dictated by the geometry of mirrors available for purchase at the time. Typically, LIF and LIE measurements are taken at an angle perpendicular to the direction of the laser pulse, although measurements at other angles have a minor effect on pointwise LIF and LII measurements within axisymmetric flames. Taking measurements at this angle, compared to perpendicularly, does have the consequence of maximising ELS, particularly from larger particles.

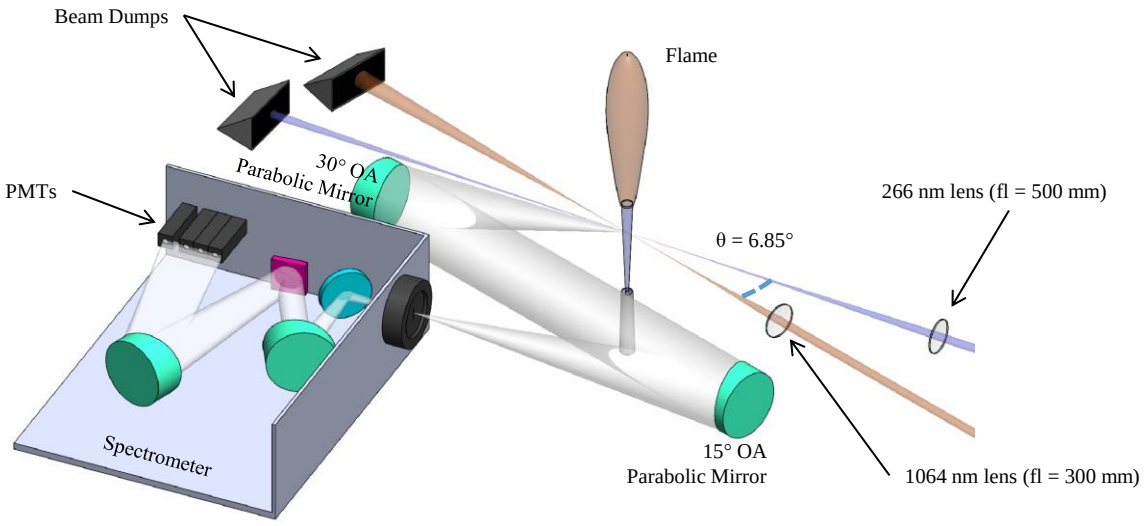

Figure 3.3: Collection optics and spectrometer internals.

3.1.4 Spectrometer

The spectrometer consists of four photomultiplier tubes (PMTs) situated at the focal plane of a 0.5 m spectrometer, as shown in Figure 3.3 and some more detail is given in Figure 3.4. A collection of flat and parabolic mirrors were used for the internal optics, with a 600 line/mm reflective grating (Thorlabs, Inc. GR50-0603) providing spectral separation. The internal layout of the spectrometer was designed and constructed by the author. The slit width of the spectrometer was adjustable and tailored to each study to maximise the signal depending on the conditions which prevents direct signal comparison between studies presented in this thesis.

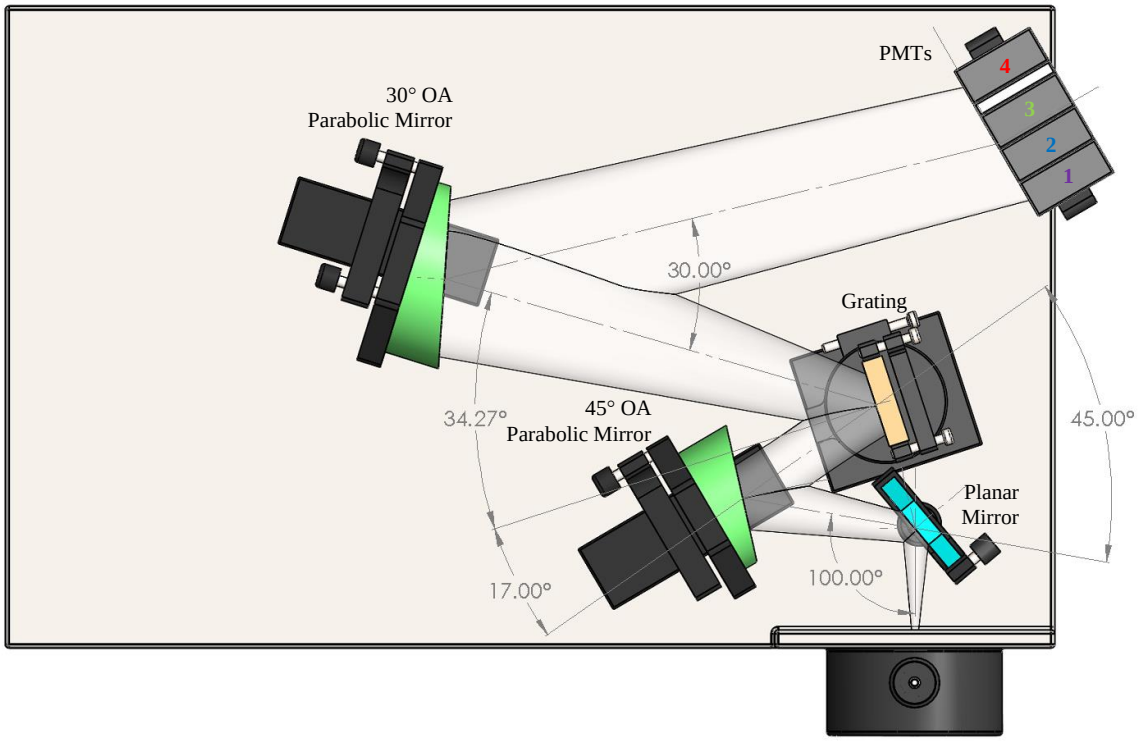

Figure 3.4: Schematic of spectrometer and internal optical layout.

All the optics within the spectrometer were “off the shelf”, but chosen specifically to achieve a high light reflectance across a broad spectrum and a spectral dispersion that allowed the placement of four 22 mm wide photomultiplier tubes at the focal plane. The light that is focused on the slit then starts to diverge again as it travels into the spectrometer. The first mirror (Edmund Optics, Inc. #48-569) is flat and serves to reflect this light into

the cavity of the spectrometer. The next mirror is parabolic (Edmund Optics, Inc. #83-971) and collimates the light before it hits the grating. The grating equation (Equation 3.1) dictates how the incident light onto the grating is then dispersed by wavelength, as further illustrated in the accompanying diagram in Figure 3.5. Where m is the order of refraction, d is the spacing between the grating grooves (1/(groves/mm)), θ_i the angle of incident beam with respect to the normal of the grating and θ_r is the angle of reflectance for the specified wavelength (λ) with respect to the normal of the grating.

$$m\lambda = d(sin\theta_i + sin\theta_r) \tag{3.1}$$

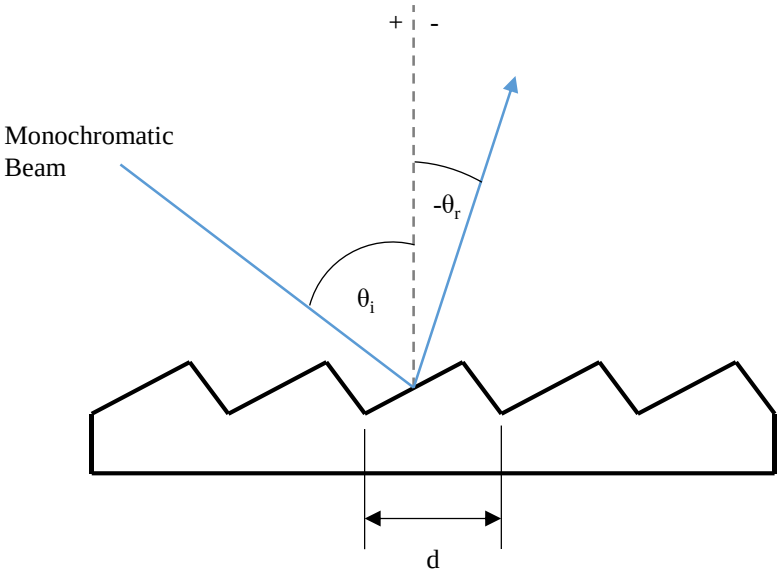

Figure 3.5: Angle of diffraction from ruled diffraction grating.

In most circumstances, the first order reflection (m = 1) is used for spectrometers, as this provides the highest reflectance. However, this Equation highlights a potential problem when investigating a broad spectrum, especially if the highest wavelength of interest is more than double the smallest wavelength of interest, which is the case in the current work. This is because the first order (m = 1) reflection of 532 nm, for example, shares the same reflection angle as the second-order (m = 2) of 266 nm. A thorough spectral calibration, discussed later, showed that this interference was not an issue and that the second-order reflection was negligible in the spectral bins chosen. The spectrally separating light from the grating was then reflected off a final parabolic mirror (Edmund Optics, Inc #83-967) to focus the light to a spectral plane at which the PMTs where placed. Parabolic mirrors were

used on the interior of the spectrometer again to remove spherical aberrations and marginally reduced the complexity of the design.

3.1.5 Photomultiplier Tubes and Oscilloscope

The four PMTs (x3 Hamamatsu H10721-210 and x1 Hamamatsu H10721-20) simultaneously collect time-resolved signals in four distinct spectral bands: PMT1 at 266 ± 15 nm, PMT2 at 350 ± 15 nm, PMT3 at 445 ± 15 nm, PMT4 at 575 ± 15 nm. Figure 3.6 shows how PMT1 tracks the ELS of the 266 nm laser, while PMT2 and PMT3 measure LIF in the UV and the visible range in spectral bands chosen similarly to earlier studies in laminar flames [26, 29, 49-51, 113, 198, 201, 202]. PMT4 was primarily used for LII measurements as it was better placed within the quasi-black body spectrum of soot at ≈ 4000 K, and being situated at longer wavelengths had reduced contribution from PAH originating LIF. PMT4 was also placed away from the wavelength 532 nm, as this part of the spectrum is prone to interference from second-order reflection of the 266 nm laser light.

PMTs are highly sensitive photodetectors, often used for counting individual photons. A photon is absorbed by a photocathode that then emits an electron into the PMT via the photoelectric effect. This electron is then accelerated by a series of charged plates, where collisions with these plates results in further electron emission. This initial electron has become a cascade of electrons that now has an amplified and measurable charge. The level of amplification can generally be adjusted via a gain voltage which affects the level of cascading inside the tube and thus the final output voltage. PMTs themselves are not able to spatially or spectrally resolve incoming light, but their advantage lies in the ability to temporally resolve incoming light. However, placing the PMTs within a spectrometer allows a degree of spectral resolution, whilst spatial resolution is dictated by the laser and collection optics. Further details on PMT operation can be found in [204].

ELS was by far the brightest emission from the probe volume, particularly in particle-rich conditions and thus needed to be substantially attenuated before entering the spectrometer. This was achieved by a 280 nm high pass filter (Newport® FSQ-WG280) in front of the spectrometer slit. This attenuated the light reaching PMT1 by more than 98% and a few percent for all the other PMTs. This, however, did have the adverse effect of reducing resolution for lower ELS signals. The dynamic range of ELS emission from the probe volume is vast, extending many orders of magnitude from gas phase scattering through to solid primary soot particles and soot aggregates.

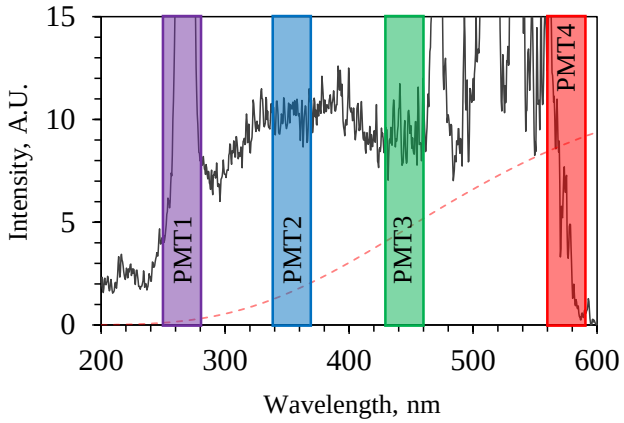

Figure 3.6: Spectral bins of PMTs overlay on example spectrum. Blackbody LII component highlighted in red (dashed).

The signals from the four PMTs were recorded using a high sample-rate (25 Giga-samples/s), high bandwidth (4 GHz) oscilloscope (Tektronix DSA70404C). Such a quick response oscilloscope was required to adequately capture the fast rise and fall of the LIF and ELS signals recorded on the PMTs. The system response in this setup was limited by the sub-nanosecond rise time of the PMTs and oscilloscope, rather than the 80 ps laser pulse, but was more than capable of resolving LIF lifetimes present in the following studies. A sample 266 nm ELS signal captured on PMT1 is presented in Figure 3.7 and exhibits a rise time of 0.85 ns. Identical system response was measured on all four PMTs by directly irradiating all of the PMTs with a significantly attenuated portion of the 266 nm laser beam.

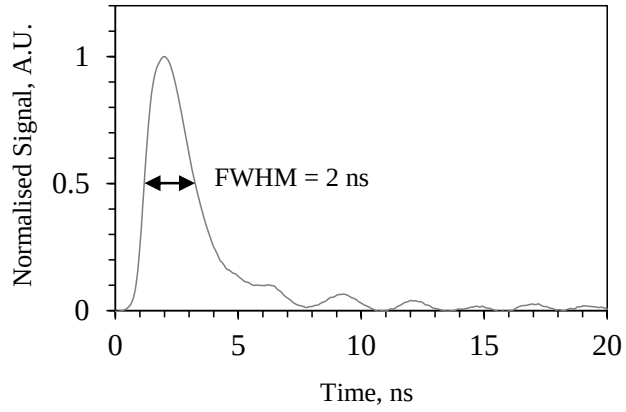

Figure 3.7: Normalised sample of measured ELS/system response (I_s).

All 4 PMTs had a gain voltage that could be set between 0.5 and 1 V, corresponding to gain multipliers of 4 x 10^3 through to 2 x 10^6 respectively. Although gain voltage could be used to mitigate issues of dynamic range, keeping a fixed gain for all studies was preferred as it allowed a reliable spectral calibration of the entire collection system. The gains for the 4 PMTs is given in Table 3.1.

Table 3.1: PMT gain voltages.

PMT	Gain Voltage, V
1	0.85 ± 0.002
2	0.75 ± 0.002
3	0.75 ± 0.002
4	0.85 ± 0.002

3.1.6 Calibration

The spectral calibration of the system was necessary for some of the data analysis as it allowed direct comparison between PMTs, particularly PMT2 andPMT3 which covered the majority of the broadband LIF. The collection system was calibrated using a broadband light source, in this case a deuterium lamp (SpectroLamps D005). The light from the deuterium lamp was focused on the entrance slit of a monochromator (built in-house by the author) and the exit slit of the monochromator emitted only a narrow spectrum, 2 nm FWHM. Inside the monochromator was a curved holographic grating (Richardson Gratings^{TM} 52094BK01-098C) that made for a simple design. Although the spectrum of the deuterium lamp is relatively well documented, the exact output of the lamp-monochromator system was not known. The spectral width, output wavelength and constant deviation with grating angle was confirmed with the use of a compact CCD (charged couple device) spectrometer (Thorlabs, Inc. CCS100). This spectrometer was not sufficient to determine the spectral response of lamp-monochromator system. For this, a calibrated photodiode (Gentec-EO PH100-SiUV), sensitive down to 210 nm, was used. The lamp-monochromator system gave the spectrum shown in Figure 3.8. Various filters were used to assess the contributions of 2nd order reflections from the grating to the spectrum and corrections made, which ensured an accurate calibration of the PMT spectrometer.

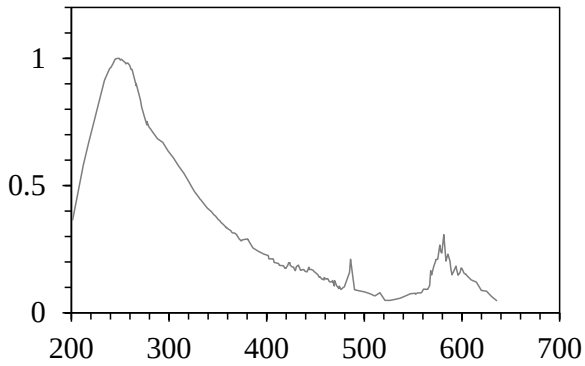

Figure 3.8: Lamp-monochromator output spectrum.

With the known output of the light from the monochromator exit slit the PMT spectrometer was calibrated. The exit slit of the monochromator was placed at the probe volume and the sensitivity of the PMTs to wavelengths across the spectrum from 250 nm to 600 nm was determined. The sensitivity and the spectral bins of the PMTs can be seen in Figure 3.9. As mentioned above, the intensity resolution of ELS measurements on PMT1 is compromised by the use of the WG280 filter, measurements are further complicated when considering the non-negligible tail of sensitivity PMT1 exhibits between 280 and 310 nm as seen in Figure 3.9. It is known that LIF signals extend down deep in to the UV [51], around 280 nm, and thus can be present on PMT1. In sooting regions of flames, this signal contributes negligibly to the ELS signal. However, at low HAB where ELS is low and LIF signals are at their peak the interference of LIF on PMT1 can be significant, when the WG280 filter is used. Where possible ELS, measurements presented here will show an error band accounting for this LIF contribution. The location and spectral bands that The PMTs capture agreed very well with intended design and could capture the three different phenomena; ELS, LIF and LII, as intended.

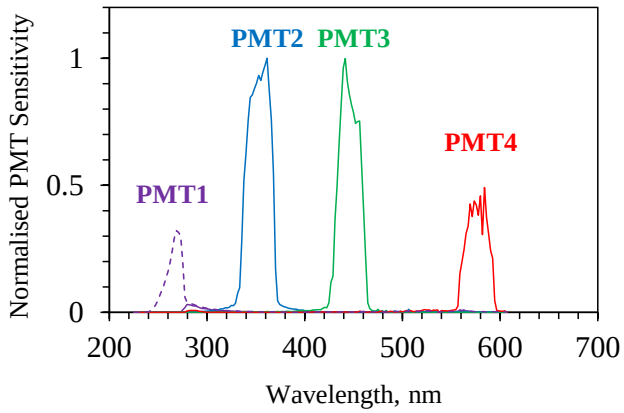

Figure 3.9: Spectral response curves of PMT spectrometer with (solid) and without (dashed) WG280 high pass filter.

3.2 Signal Processing

The signals recorded by the oscilloscope were time traces of the measured emission, an example of LIF @ 350 nm and LII from 1064 nm is shown in Figure 3.10, and these are measured in volts. The recorded LIF signal is a convolution of the laser pulse, the system response (seen in Figure 3.7) and true dynamics of the material, be it molecules, nanostructures or particles being probed. There are several features of this emission that can be analysed.

3.2.1 Peak, Integral and Tau

The intensity of the signal can be measured either by taking the integral or the temporal peak that it measured only a few nanoseconds after the laser pulse. The other important feature of the signal is the temporal decay or, in the case of LIF, the fluorescence lifetime. For LIF measurements, intensity can be proportional to concentration of the fluorescing species [50, 98, 184, 186], providing the effects of temperature and quenching species [51, 117, 136] is negligible, while the signal decay is exponential in nature as it originates from molecular electronic levels. Before any of these values were determined all signals either instantaneous or averaged were background corrected. Because each signal was recorded with at least a 50 ns window prior to the 266 nm pulse each signal had its own background, as illustrated in Figure 3.1. This allowed for active background subtraction in turbulent flames whose instantaneous luminosity fluctuated. The shot to shot fluctuation found in

steady laminar flames was found to have a standard deviation of 13% off the mean. Measurements in laminar flames, where multiple signals were averaged, the system showed excellent repeatability.

Recorded LIE signals are a convolution of the exponential decay function is determined by the type of emission and the system response, as defined in Equation 2.13 and displayed in Figure 3.10. The recorded signal (I_R) still resembles its exponential source, however, is distorted by the convolution process, exhibiting a finite rise and fall to the signal. To obtain the actual lifetime of the material being probed from the collected LIE signals, a deconvolution process is required to extract the exponential decay function (I_E). It was found that, with the short 80 ps laser pulse and the quick system response (I_S), the LIF decay was better fitted with a bi-exponential (Equation 3.2). This is likely due to the distribution of species being excited within nanostructures. A bi-exponential decay in TRFPA experiments has been found for nanoparticles and used to retrieve information about their sizes [98, 122, 184, 205]. Also, bi-exponential behaviour also has been observed by Ossler et al. [117] for PAHs at elevated temperatures. Some decay times presented in the current are the effective time decay (τ_{eff}) computed as a weighted mean between the two exponential components (Equation 3.3). The bi-exponential function constants are obtained by fitting the signal from each PMT to a multi-parameter library using a non-linear least squares fitting algorithm. For this method, three independent variables were solved for, τ_1, τ_2 and A_1. A_2 is a dependant variable, such that $A_2 = 1 - A_1$, where $0 \leq A_1 \leq 1$. Some restrictions were also placed on τ_1 and τ_2 to keep decay times within a reasonable range (0 and 500 ns). In laminar flames where LIF signals were relatively smooth due to averaging, the fitting error using this technique was always small, less than 5%. Having said this, a single exponential fit, discussed later, was found to be more than sufficient in determining τ_{eff} and assessing the changes in the decay times.

$$\hat{I}_E(t) = A_1 e^{\left(-\frac{t}{\tau_1}\right)} + A_2 e^{\left(-\frac{t}{\tau_2}\right)} \tag{3.2}$$

$$\tau_{eff} = (A_1\tau_1 + A_2\tau_2)/(A_2 + A_2) \tag{3.3}$$

The same procedure can be performed on the 1064 nm LII measurements, although the total system response is very much impacted by the long pulse duration of the Quanta Ray laser. It was not possible to directly measure the combined response (I_S) of the 1064 nm pulse as no PMT was positioned or sensitive to capture the scattering signal of the laser pulse in the IR region. As an alternative, the pulse length was measured using a photodiode to estimate the system response function with a FWHM of 8 ns. In this case, the precision of the system response function is less important considering the relative length of the measured LII signals (> 50 ns) as seen in Figure 3.10 where pure LII signals from 1064 nm

pulse decay at a much slower rate than those from LIF. The use of a bi-exponential fit for LII is rather mandatory as has been discussed in literature [43, 206]. This is found to be mainly due to the distribution of particle and aggregate sizes present in the soot leading to different constituent decay times.

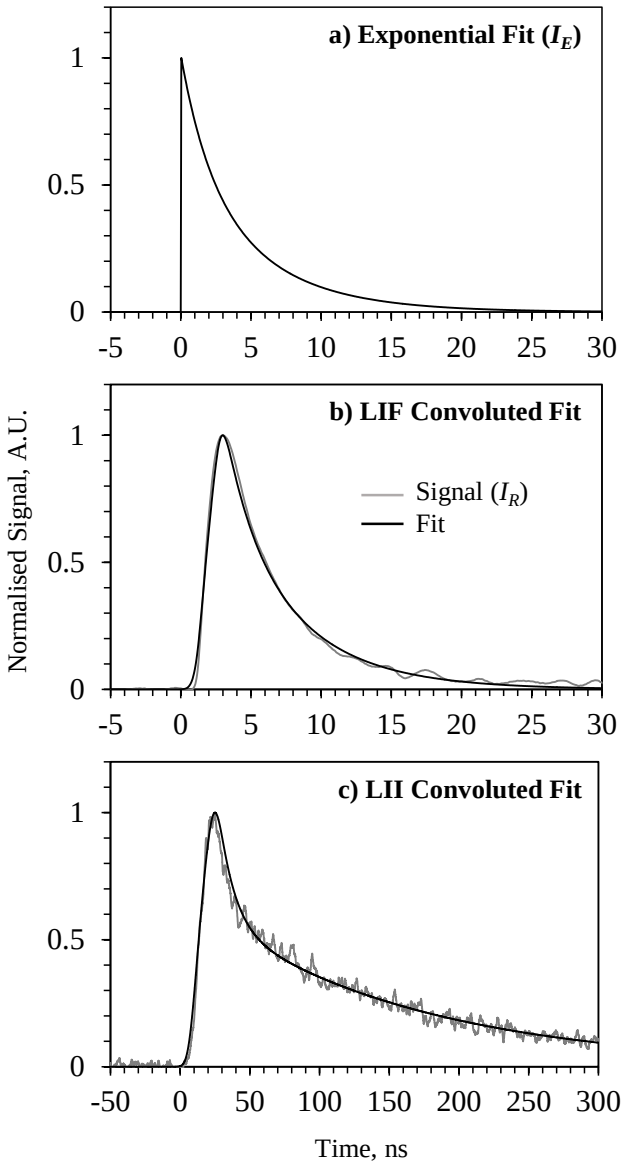

Figure 3.10: Example of a) underlying exponential emission function (I_E) and convoluted bi-exponential fits for example b) LIF and c) LII signals.

An alternative method for determining the effective time decay was also used in this work. The decay times can be determined by taking the integral of the peak normalised signal.

The value of this integral has a linear relationship with an actual single exponential decay time, provided that the actual decay time is not substantially less than the FWHM of the system response responsible for the convolution of the signal. The measured system response is shown in Figure 3.7 and has a FWHM of 2 ns. Consequently, decay times less than 1 ns, using this method, should be treated with caution, although, none are observed in these studies. Figure 3.11 highlights the suitability of this fitting procedure against single exponential functions and the proportional nature of the normalised integral for decay times greater than 1 ns. In this Figure, the peak normalised integral is taken from 0 to 200 ns and results in the displayed Equation for τ_{eff}. Using different integral windows will result in slightly different constants for the linear trend. This method provides a very good fit to the LIF signal and is acceptable for signals where there are not multiple emission contributing to the signal. Conversely in sooting regions of flames where fluorescing and incandescing species can co-exist it can be challenging to separate the relative contribution of LIF from LII. In areas of only LIF a maximum error of 18% was found compared to a bi-exponential convoluted fit described above. This simpler method proved to be a necessary time saver in the processing of turbulent data where thousands of decay times needed to be extracted for each location in a flame. This method was also used for the laminar diffusion and partially premixed studies presented here. Time-resolved 266 nm LIF measurements, used in the present work, can delineate between LIF from PAH and that originating from nanostructures. It is known that PAH LIF decay times decrease rapidly at flame temperatures [117] and thus longer LIF decay times are attributed to nanostructures [1, 51].

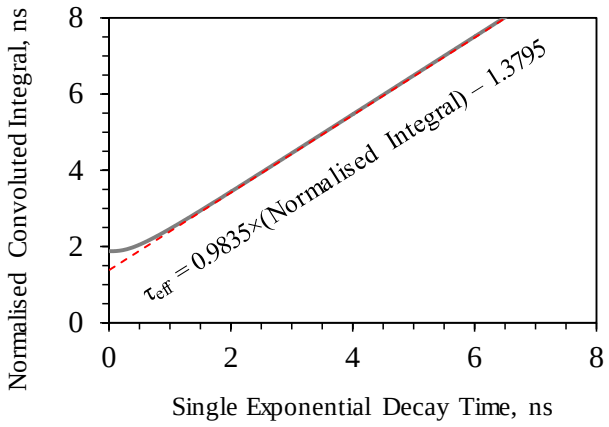

Figure 3.11: Normalised integral (0-200 ns) fit against actual single exponential decay time (solid). Linear trend highlighted in red (dashed) with the fitted decay time given in the Equation.

3.3 Burners

Three different burners were used in the studies presented here to investigate various modes of combustion. These include, diffusion, partially premixed, premixed and turbulent combustion. All burners were rigidly mounted to the 3-axis traverse of a milling machine. This allowed the flames to move with respect to the laser and optical collection system facilitating measurements at numerous locations within each flame. The flowrates of fuel, oxidiser and inert gases were controlled by Alicat Scientific Mass flow controllers. The specific flames investigated and flowrates used are detailed in the appropriate Chapters for that study. All volume flowrates listed in this thesis are given as Standard Litters per Minute (SLPM) for standard conditions of 25 °C and 101.3 kPa, unless otherwise stated.

3.3.1 Laminar Coflow Burner

For the atmospheric diffusion and partially premixed flames a burner initially developed at Yale University was used [200, 207-209]. It consists of a stainless steel 4 mm inner diameter jet for the fuel mixture surrounded by a 74 mm diameter air coflow as shown in Figure 3.12. The air coflow is fed from four points spread around the base into a small plenum area before passing through two layers of honeycomb and a section of 3 mm diameter glass beads to create a uniform flow field at the exit. O-rings and compression tube fittings are used to ensure the burner is properly sealed.

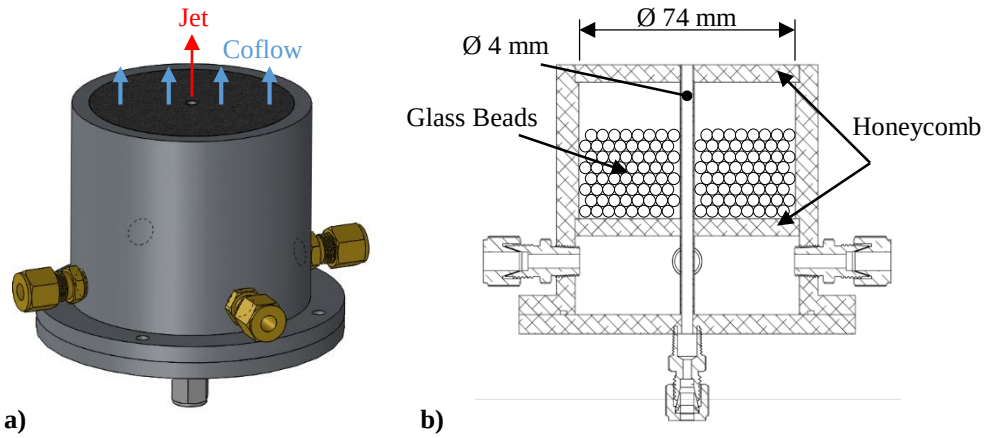

Figure 3.12: Yale coflow burner [209] a) solid model and b) cross-section drawing.

This burner has already been used for several studies of sooting flames [142, 167, 207, 208, 210-213] that makes it very appropriate for comparison with the current technique. Many of these studies have been computational or focused on soot measurement through LII, extinction, TEM and scattering. Most notably, a selection of flames using ethylene have been chosen as a set of target flames for the ISF workshop [200], which becomes the focus of the study presented in Chapter 5.

3.3.2 Laminar Flat Flame Burner

Atmospheric rich premixed flames were stabilised on a Bronze McKenna burner flat flame burner [214] as seen in Figure 3.13a . The fuel-air mixture flows through a water-cooled, porous, sintered bronze 60 mm diameter outlet. This gives a uniform flow outlet allowing for the “flat” flame. The flame is shielded by an annular coflow of nitrogen. This configuration separates the centre of the flame from diffusion with ambient air. For the study presented in Chapter 4, a circular stabilisation plate is situated 28 mm above the burner surface to maintain a flat flame and can be seen in Figure 4.1. The height of the stabilisation plate varies between studies in literature. However, the purpose is always to contain the flame resulting in essentially a one-dimensional flame. To prevent the burner from overheating, cooling water is pumped around the bronze through a copper tube coil. A similar style capillary burner is also used in Chapter 4, with very similar dimensions and produces near identical flames. The only practical difference is that the sintered bronze is replaced with 1 mm diameter stainless steel tubes as seen in the photograph in Figure 3.13b. Similar and complementary measurements to the LIF and LII technique described above have already been made in flames using the McKenna or capillary burner [21, 113, 198, 201, 215, 216]. For this reason, some of these flames were chosen for early experiments to validate the technique as discussed in Chapter 4.

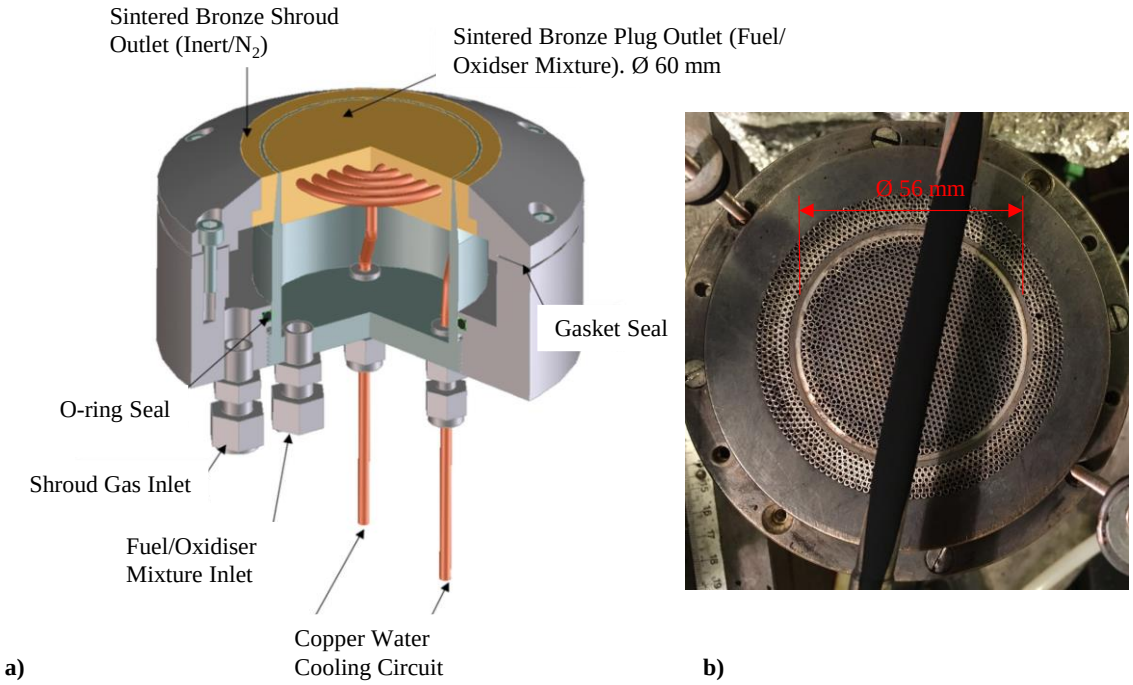

Figure 3.13: a) McKenna burner cross-section [214] and b) Top view of capillary burner.

3.3.3 Turbulent Jet Burner

Turbulent combustion was investigated through the use of a piloted jet burner as a suitable choice for the investigation of sooting turbulent flames, similar in design to the Sydney piloted burner [217]. The fuel mixture exited from a 4 mm inner diameter stainless steel jet. The jet tube was 850 mm in length, ensuring that the turbulent flow reaching the jet outlet was fully developed. The mixture was ignited and the flame attached to the burner by a 15 mm annular pilot as shown by the drawing in Figure 3.14a. Having a pilot allows for investigation of sooting flames at substantial Reynolds numbers, in comparison to an unpiloted jet, and removes such variables as auto-ignition [217]. The pilot mixture of Hydrogen (H_2), acetylene and Air was well within the flammability limits and first passed through a porous sintered bronze flame arrestor to prevent flashback. The pilot plate was 2 mm thick was recessed only 4 mm from the jet outlet to minimise the pilot preheating the jet tube and gases. The pilot consisted of 3 concentric rings of holes that were sized and spaced to achieve uniform porosity (percentage of hole area) over the pilot plate. The purpose of this is to achieve a uniform flow and temperature boundary across the pilot flame annulus [218]. Detailed drawings of the burner are provided in Appendix A. The use

of a well-defined pilot is beneficial, particularly form a modelling perspective to have a known and defined boundary conditions [217, 218].

A large wind tunnel provided a coflow to shield the jet from ambient disturbances and provide a repeatable flow configuration. A cross-section of the coflow is provided in Figure 3.14b. Filtered air is pumped through the converging duct before passing through a perforated plate (1 mm thick with 1 mm diameter holes with 2 mm spacing) and a series of wire mesh (0.25 mm wire with a spacing of 1 mm) and aluminium honeycomb to produce uniform flow at the 225 mm x 225 mm outlet. The two instances of honeycomb are not shown for the sake of clarity, although their position is indicated in Figure 3.14b between the perforated steel plate and mesh. The honeycomb filled the 50 mm gap between the mesh/perforated plate and had a cell size of 8 mm. The uniformity of the wind tunnel was measured with a hot wire anemometer, with a precision of ± 0.1 m/s. With a bulk coflow velocity of 5 m/s the variation over the coflow area was less than ± 0.3 m/s.

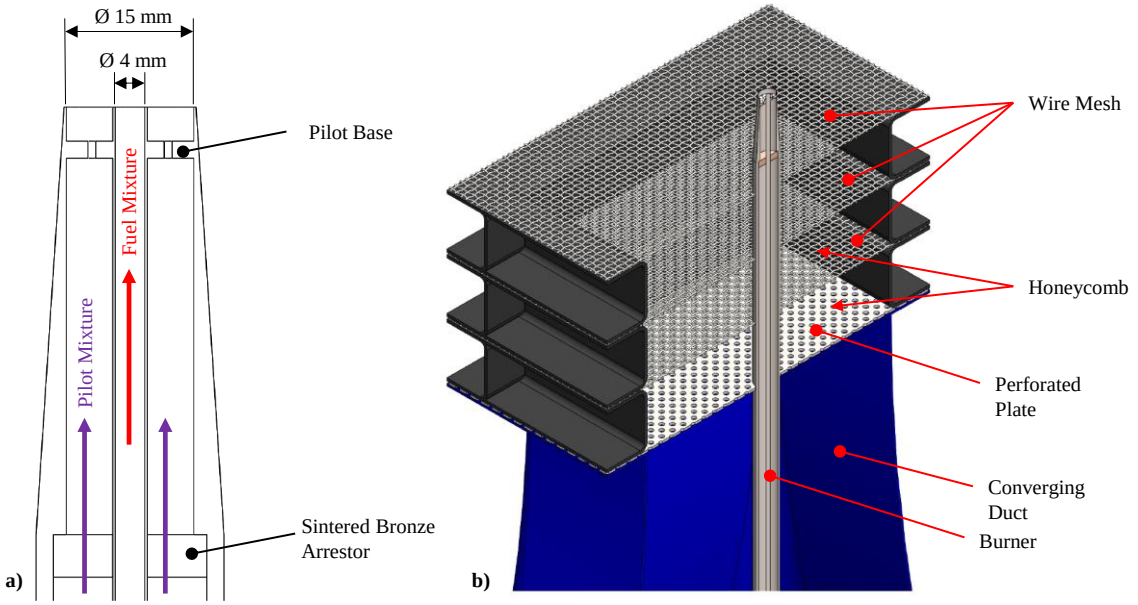

Figure 3.14: Cross-section of turbulent jet burner outlet and b) cross-section of burner within coflow wind tunnel.

Chapter 4: Laminar Premixed Flames

This Chapter presents both in-situ and ex-situ measurements of nanostructures and soot in laminar rich premixed flames. The bulk of the work presented in this Chapter has been previously published [1]. Two laminar flame burners are studied covering a range of C/O ratios and hence different sooting propensities. In addition to the temporally resolved LIE measurement technique described in Chapter 3, complementary measurements performed at Università degli Studi di Napoli Federico II by Mariano Sirignano and Marielena Conturso are discussed here. These measurements are valuable in validating the technique developed at the University of Sydney and add to the discussion and interpretation of LIE signals.

The objective of this first study is to confirm the presence of LIF from nanostructures and to exploit such phenomena, along with other measurements, to further elucidate their hybrid behaviour and transitional nature (from molecules to solid particles) by comparison to soot. Ex-situ measurements using DMA are reported here along with in-situ measurements using LII, ELS and LIF which is detected both in the visible and the UV bands. Collectively, the data reported in this Chapter demonstrates the capability of the aforementioned time-resolved LIE technique to simultaneously track nanostructures, soot and key features in their evolution within flames.

4.1 Experimental Setup

This section describes a series of experiments conducted in two laboratories, in Sydney and Naples, using complementary in-situ and ex-situ techniques applied to similar laminar premixed flames. In-situ, spectrally resolved LIE, thermocouple and ex-situ Differential mobility analyser measurements were conducted in Naples, whereas time-resolved LIE measurements were carried out in Sydney under similar conditions.

4.1.1 Temperature Measurements (Naples)

Temperature measurements were performed using a rapid insertion procedure of a silica-coated Pt/Pt–13%Rh thermocouple with 125 µm diameter wire and a bead diameter of about 225 µm [219]. The Thermocouple remained within desired location for more than 100 seconds. To minimise the heat conduction along the thermocouple wires, the thermocouple was positioned parallel to the burner surface. The soot deposited on the thermocouple was burnt off after each measurement by exposing the bead to a methane torch. The applied radiation correction was similar to that of McEnally et al. [192] and was found to be of the order of 10% whereas the uncertainty associated with these measurements was estimated to be within ± 25 K.

4.1.2 Flame Setup and Conditions

Two burners were used to produce the atmospheric pressure premixed flat flames studied here. The laboratory in Naples used a stabilised capillary burner [21, 113, 201, 215, 216] while Sydney used a bronze McKenna burner (as detailed in Section 3.3.2). Both configurations stabilised the flame with a steel plate situated 2.8 cm above the burner surface. Ethylene/air premixed flames with a set of molar carbon to oxygen (C/O) ratios of 0.67, 0.77 were investigated in both laboratories where the bulk gas mixture velocity was maintained at 10 cm/s at standard conditions. Images of the flames and the flowrates used are presented in Figure 4.1 and Table 4.1 respectively. The capillary burner was cooled with water (1.0 L/min) kept at 70°C using a thermostatic bath whereas the McKenna burner was cooled with 0.7 L/min of colder water at 20°C. The Naples and Sydney burners produce near identical flames for C/O ratios of 0.67. However, the McKenna Burner produces flames slightly lifted compared to the capillary burner for the C/O ratio of 0.77. This difference is thought to be due to the different water temperatures employed in the cooling system and the difference in heat transfer (namely sintered bronze vs. stainless

steel tubing). Although this affects the absolute location of the reaction zone, it does not change the evolution of the particles, so the results from both burners remain comparable. The similarities between the flames stabilised on both burners can be noted from the mean axial temperature profiles measured along the centrelines and reported in Figure 4.2 Both flames have similar peak temperatures ranging from 1770 K to 1700 K depending on the C/O ratios, and the decay rate in the hot combustion products is identical. For the case of C/O = 0.67, the flame front is located at 1.5–2.0 mm above the burner whereas the flame with C/O = 0.77 shows a slightly broader shift in the location of the peak being between 2 and 3 mm.

Table 4.1: Rich premixed flame details.

Flame	**C/O = 0.67**	**C/O = 0.77**
C_2H_4 flowrate, SLPM	2.08	2.35
Air flowrate, SLPM	14.88	14.61
ϕ	2.01	2.31
Shroud	N_2	N_2
Soot	Not detectable by LII	Sooting
All bulk velocities are 10 cm/s. Flowrates differ slightly for capillary burner but match the same bulk velocity.		

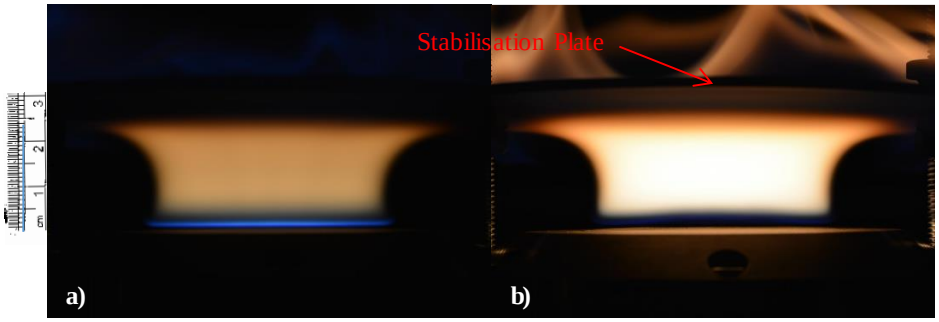

Figure 4.1: Photograph of flat rich premixed laminar flames a) C/O = 0.67, b) C/O = 0.77. Scale in cm.

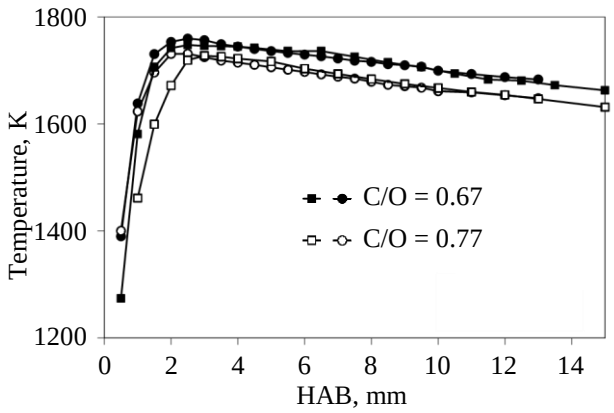

Figure 4.2: Centreline temperature profiles measured in the McKenna burner in Sydney (squares) and the capillary burner in Naples (circles) for C/O = 0.67 and C/O = 0.77 flames.

4.1.3 Spectrally Resolved LIE Measurements (Naples)

Spectrally resolved measurements of LIE were obtained between the wavelengths of 200 and 550 nm using the fourth harmonic (266 nm) of an Nd:YAG with an 8 ns laser pulse as an excitation source. The experimental setup is the same as that employed in previous works [49-51, 113, 198, 201, 202] and is similar in principle to the technique described in Chapter 3. A schematic of the setup is shown in Figure 4.3. The laser beam was focused to a diameter of 350 μm at the centre of the flame. The energy of the laser pulse was kept constant at 0.8 mJ (0.83 J/cm^2) as a compromise between laser-induced emission signals and species interference due to fragmentation. It is noted that the high fluence of the 266 nm laser pulse can result in fragmentation of gas phase compounds (such as ethylene) or particles which subsequently produce small fragments of unknown nature. The spectral response allows the detection of suspicious bands due to undesired phenomena such as emission from these fragmented compounds or particles. The emitted radiation was collected at 90° with respect to the laser beam, focused onto the 280 μm entrance slit of a spectrometer and detected by an intensified CCD (ICCD) camera (placed at the spectral plane) thermoelectrically cooled down to −10°C to reduce noise. The measured spectra were corrected for the spectral response of the detection system. The emission spectra were detected using a gate time of 100 ns synchronised with the laser pulse and by summing the CCD counts over 150 scans. In this way, ELS, LIF and LII signals were detected simultaneously.

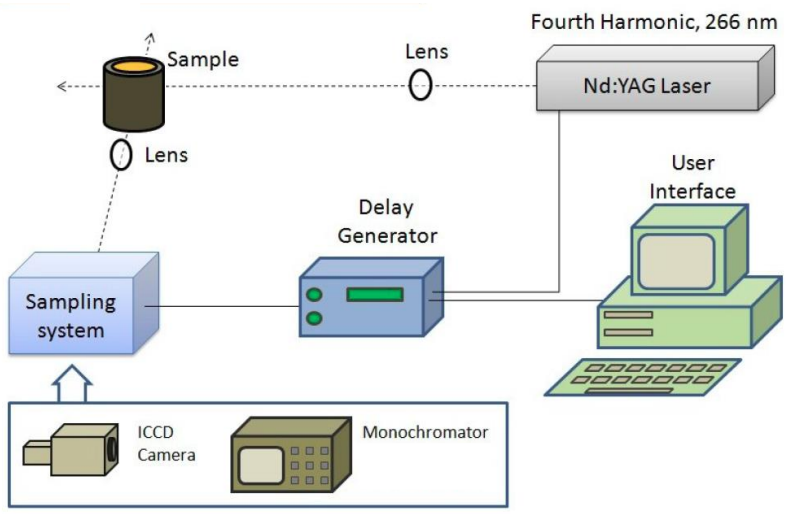

Figure 4.3: Schematic of Naples Spectrally resolved setup [220].

Figure 4.4 shows spectral measurements of LIE performed in the capillary burner using 266 nm excitation with 8 ns pulse duration. The spectrum is shown for height above the burner of 15 mm in a flame with C/O = 0.77 and covers the 200 nm to 550 nm spectral range. It is evident from Figure 4.4 that the four prominent spikes in the spectrum can be attributed to ELS from particles at 266 nm and the residual 532 nm along with the two C_2-swan band emissions centred 470 and 516 nm. Also shown in Figure 4.4 (dashed line) is the blackbody curve at 3750 K which matches the detected signal at 550 nm, hence implying the presence of LII from large particles and LIF both in the UV and the visible bands. The blackbody curve is here used, as in previous works [51, 99], to subtract the contribution of LII to the LIF. The use of 3500 K or 4000 K as temperature for the blackbody curve has a minor effect, on the order of 10%, on the LIF determination. More importantly, the profiles of the LIF along the HAB are not affected.

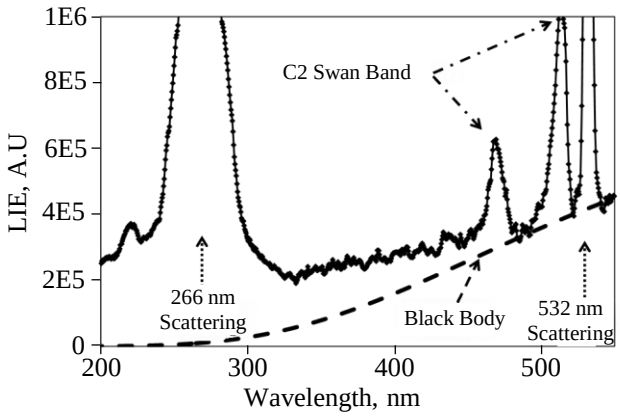

Figure 4.4: Spectrally resolved LIE performed in the capillary burner with an 8 ns, 266 nm laser pulse in a laminar premixed ethylene flame with C/O = 0.77 at HAB = 15 mm.

4.1.4 Time-Resolved LIE Measurements (Sydney)

For the time-resolved measurements the technique described in Chapter 3 was used with the following setup. The 4 PMTs captured the temporal decays of the three prominent LIEs; ELS, LIF and LII in the chosen spectral bands. The 266 nm Ekspla laser had an energy of 0.55 mJ/pulse measured at the probe volume, giving a fluence of 1.1 J/cm^2 for the 266 nm probe. The 1064 nm Quanta Ray laser was set to a fluence of 0.6 J/cm^2.

The laser energy was selected to achieve the highest signal, whilst minimising the fragmentation of the particles and eventual side emission from these fragments. The use of UV excitation can result in particle fragmentation, however, no sign of fragmentation was obvious within the current measurements. Additionally, the laser fluences used are orders of magnitude lower than those used specifically for fragmentation of soot [221, 222]. In order to verify that the signal detected on PMT2 and PMT3 is genuinely LIF, in Figure 4.5a signal intensities for the PMT2 obtained with different laser energies, in a region where large LII signal is detected, is reported to show the independence of the collected signal in the fluence range investigated. The linear trend observed in the non-sooting region (HAB = 7 mm) and the sooting region (HAB = 13 mm) is what is expected from fluorescence emission, whereas a departure from this linear trend would suggest a significant component of LII or photofragmentation (a multi photon process). Similar linearity was also measured for PMT3. Additional interference may come from a LII contribution to the signals seen on PMT2 and PMT3 induced by the UV laser. If a LII contribution is present on PMT2 and PMT3, then a correction similar to that applied in the spectral measurements (as shown in Figure 4.4) could be applied. It was found that, for the

cases studied here, such correction is not necessary because the influence of LII on PMT2 and PMT3 was not significant. Figure 4.5b shows the signal recorded on PMT3 at various UV laser fluences and highlights that any contribution from long lived LII is insignificant as there is no difference in the response along the entire signal at various fluences. In fact, LII has less than 8% impact on the determination of fluorescence lifetime for the presented flames.

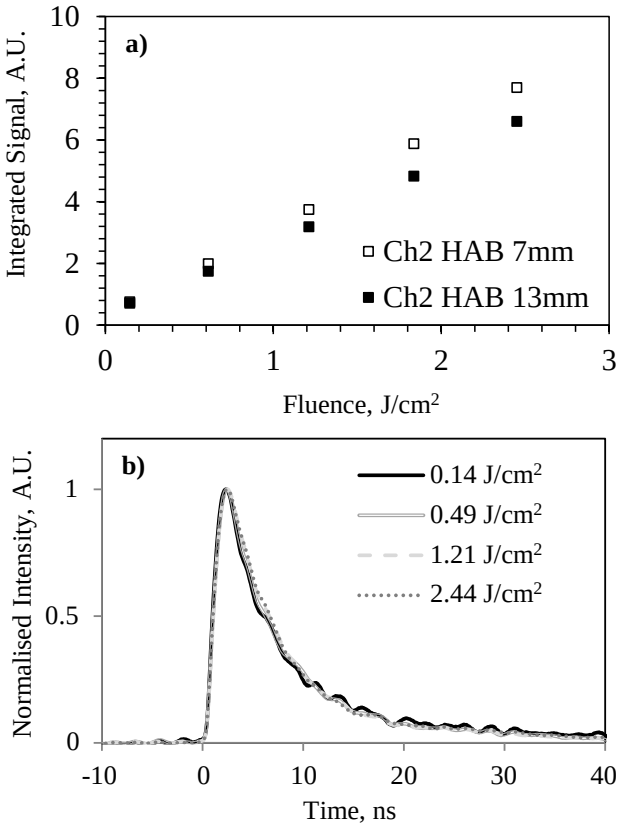

Figure 4.5: a) Integrated signal detected on PMT2 (LIF @ 350 nm) in the C/O = 0.77 flame at HAB = 7 mm (□) and HAB = 13 mm (■) versus the fluence of the 80 ps at 266 nm laser pulse. b) PMT3 signal detected in C/O = 0.77 flame at HAB = 13 mm with various 266 nm laser fluences.

The slit of the spectrometer was set to 20 µm to keep all signals within the dynamic range of the oscilloscope. Each flame was measured incrementally along its axis and at each location, 500 instantaneous acquisitions were recorded and subsequently averaged. In Figure 4.6, a typical measured signal collected using the temporally resolved system with the PMT positioned at 350 nm, (LIF @ 350 nm), is reported versus acquisition time collected at HAB = 10 mm in the flame with C/O = 0.67. The signals are reported starting

from the maximum of the ELS signal to help evaluate the accuracy of the technique for small decay times in the order of few nanoseconds, similar to those found in flames. The convoluted signals generated by using the measured ELS signal and a fixed decay time are also reported and these represent the typical fitting curve used to retrieve the decay time. The curve corresponding to a decay time of 0 ns represents the measured ELS (black dotted line). It is worth noting that this signal is longer than the 80 ps of the laser pulse due to the finite system response of the PMTs and oscilloscope.

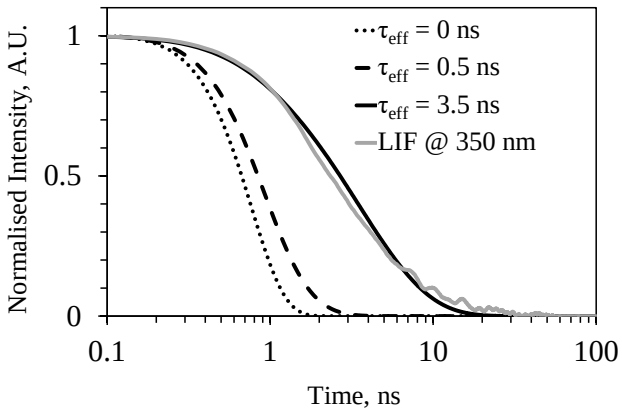

Figure 4.6: Time-resolved signals of LIF @ 350 nm measured in the McKenna burner at HAB = 10 mm in C/O = 0.67 flame (grey line). Exponential fits with different τ_{eff} are also reported.

It is evident from Figure 4.6 that the measured LIF (solid grey line) is well-fitted by a convoluted signal generated using a decay time of 3.5 ns (solid black line) which is well within the sensitivity of the system. This decay time is significantly longer than that measured for molecular PAH fluorescence at flame temperatures (τ_{eff} < 0.5 ns, dashed line) [117] as represented by a convoluted curve generated with a decay time of 0.5 ns. A very similar behaviour has been found in the visible region, i.e., PMT positioned at 445 nm. These decay times, in the order of 3–5 ns are almost an order of magnitude shorter than the LII, which has decay times larger than 20 ns.

For these measurements, the 1064 nm pulse was delayed by 100 ns with respect to the 266 nm pulse. Due to the low jet velocities of 10 cm/s in the studied flames both these measurements are deemed to excite the same packet of gas. This is because the displacement over 100 ns is in the order of 1×10^{-7} m, orders of magnitude less than the diameter of the probe volume. This simultaneous measurement is not necessary in steady laminar flames, but is by design for the systems use in turbulent flames. However, this has

the potential for interaction between the two laser pulses. The first pulse could result in newly formed particles from laser ablation and sublimation of soot [150, 179, 180] affecting the particle morphology and particle size distributions [149]. To identify any influence of the 266 nm pulse on the subsequent 1064 nm pulse, an additional experiment was conducted where only the 1064 nm pulse was employed and the results are reported in Figure 4.7 for HAB = 10 mm in the C/O = 0.77 flame. Both profiles collected on PMT4 shown in Figure 4.7 overlap confirming that the first 266 nm pulse has no influence on the LII collected on PMT4 due to the 1064 nm pulse. It is also worth noting that the second pulse is the 1064 nm laser and is used primarily as a marker of soot through LII, with the focus of the study more on LIF measurements. Additionally, in this study it was found that the LII generated from the preceding 266 nm pulse was insignificant in comparison to the LIF signal and the 1064 nm LII. Whilst the use of a laser fluence of 1.2 J/cm2 might be expected to at least partially sublimate or ablate soot, no observable impact was made in this test. As this result did not detrimentally impact results going forward it is not laboured in this thesis. However, it is tangentially an interesting interaction (or lack thereof) which warrants further investigation. Perhaps the picosecond regime of the 266nm laser pulse does not couple as efficiently with soot absorption as it does with nanosecond laser pulses.

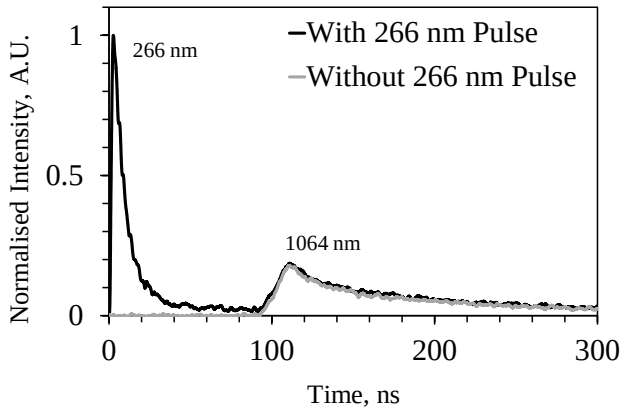

Figure 4.7: PMT4 signal detected in C/O = 0.77 flame at HAB = 10 mm using both 266 nm and 1064 nm consecutive pulse (black line) and just with 1064 nm pulse (grey line).

4.1.5 DMA Particle Size Distribution Measurements (Naples)

Particles were sampled with a stainless-steel probe placed horizontally at different HAB from 6 to 15 mm in an arrangement similar to [13, 22, 35-39] as seen in Figure 4.8. Although the perturbation of the flame is evident, the system has proven to be reliable in the determination of the particles size distributions (PSDs) even in highly sooting flames

with equivalence ratios as high as 2.46. In the present work, the probe has an ID = 8 mm, a wall thickness of 0.5 mm, and a pinhole diameter of 0.8 mm which is larger than those used in previous works [112]. The large pinhole has the advantage of reducing the clogging which is a problem for smaller pinholes when placed in a fully sooting flame. With a pinhole of 0.3 mm, the dilution ratio required may be of the order of 10^4 whereas with the 0.8 mm pinhole used here, a dilution of 500 is achieved for the investigated conditions.

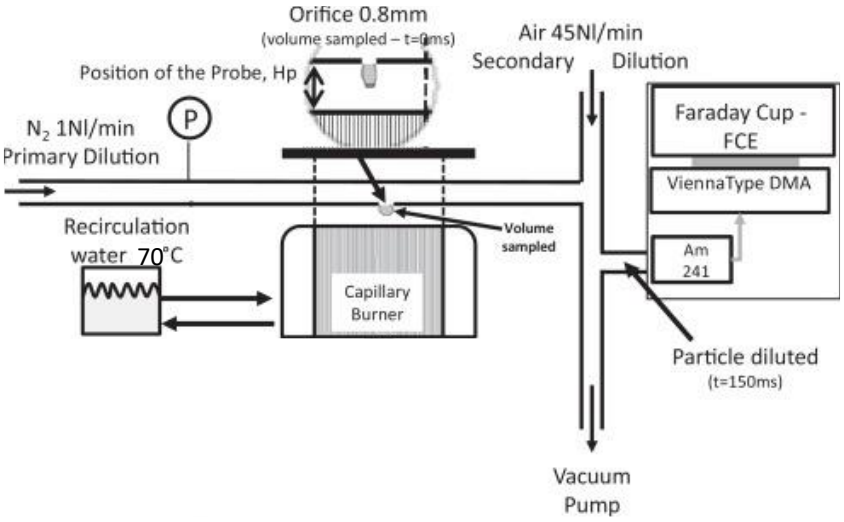

Figure 4.8: Schematic of particle sampling setup (Naples) [22].

The disadvantage is that the lower dilution increases the possibility of coagulation of particles and surface condensation of gas phase PAHs onto the particles in the probe line. To reduce the impact of these phenomena on the PSD, the probe line was modified so that the dilution is split into two stages. The first stage occurs in the probe itself by using a carrier gas, similarly to other apparatus [34, 87-93] while second dilution stage is placed just after the flame where the carrier gas containing particles is mixed with a cold gas stream. In the probe, the carrier gas has been reduced to 1 L/min (at 273 K, and 101.3 kPa) and the sample is immediately diluted with 45 L/min. This ratio between the two streams allows an immediate cooling of the sample, necessary to operate the DMA safely. Finally, the DMA has been placed just after this secondary dilution. The total residence time of the particles in the probe line is 160 ms. Comparable results are obtained from the 0.8 and 0.3 mm pinholes for the slightly sooting flame conditions where both probes can be used without clogging.

For the PSD measurements, a nano-DMA was used (TapCon 3/150 DMA system in high voltage mode corresponding to a nominal size range 2–100 nm equipped with a Faraday Cup Electrometer detector). At the entrance of the DMA, a radioactive (Am-241) bipolar

diffusion charger was placed such that particles reach Fuchs' steady-state charge distribution [160]. Particles then enter in the nano-DMA where they are separated according to their electrical mobility in an electrical classifier. The classified particles are then counted by an Electrometer Faraday Cup. By varying the electrical field applied to separate particles it is possible to rebuild the original PSD. The PSDs obtained by DMA was successively corrected for losses in the pinhole and the probe following the procedure reported in the literature [146, 160, 223]. DMA separates particles on the basis of their mobility diameter so that finally the particle diameter was retrieved from the correlation proposed by Singh et al. [71].

4.2 Results and Discussion

Results for two flames, namely C/O = 0.67 and 0.77, will be reported here as good respective representatives of non-sooting and sooting conditions. For convenience, the measurements performed in Naples are referred to as spectrally-resolved or intensified charge-coupled device (ICCD) data while results from the Sydney experiments are termed time-resolved or PMT data.

Figure 4.9 presents axial profiles measured along the centrelines of flames with C/O = 0.67 and C/O = 0.77 using both the capillary burner and the McKenna burner. The Sydney measurements in the McKenna burner employ a picosecond laser source and are time-resolved as the signals are collected on fast PMT's (Sydney, right) while the capillary-flames are probed with an 8 ns at 266 nm laser pulse and are collected on an ICCD hence spectrally resolved covering the region from 250 to 550 nm (Naples, left). For ease of comparison, the ICCD signals (left) are reported at selected wavelengths, namely the same spectral bands (350 ± 15 nm and 445 ± 15 nm) collected by the time-resolved measurements while the signals from the PMTs reported on the right-hand side of Figure 4.9 are integrated over 100 ns, namely the same gate time of the ICCD. Results are normalised with the relevant maximum values to facilitate comparison. The uncertainty for both the ICCD and PMT measurements lies within 5% which encompasses the small bumps observed along the profiles.

It is evident from the profiles shown in Figure 4.9 that the trends are similar for both the ICCD and PMT measurements and these, in turn, are comparable to what has been reported earlier in similar flames [21, 215]. Starting just after the flame front (which is around 2–3 mm, as shown in Figure 2), the ELS signal in both flames is higher than that expected for gas phase scattering which is reported as a grey-shaded band in two top panels of Figure 4.9. ELS from the gas phase was measured in cold ethylene and is scaled by the cross-

section of the burnt gas (CO, CO_2) at the flame temperature. Ideally it would be better to calculate the gas phase scattering including contribution from gas phase PAH. However, refractive properties of such species ae difficult to come by. The lower and the upper limit of the grey band correspond to temperatures measured in the current flames. ELS results obtained from both ICCD and PMTs for the C/O = 0.67 flame remain almost uniform at all HAB's. On the contrary, the C/O = 0.77 presents a strong increase of ELS signal moving towards the flame tip. In both flames, the LIF @ 350 nm signal (row 2, from top) peaks just after the flame front (HAB ~ 3 mm) and decreases towards the flame tip. The LIF @ 445 nm (row 3 from top) signal peaks just after the LIF @ 350 nm and then decreases slightly for the flame with C/O = 0.67 whereas it is possible to see an overall increase of the signal near the tip of the C/O = 0.77 flame. It should also be noted that both LIF @ 350 nm and LIF @ 445 nm signals are consistently higher in the sootier flame with C/O = 0.77.

The overall comparison presented in Figure 4.9 confirms that the techniques (ICCD and PMT) are substantially equivalent in tracking LIF signals and possess similar advantages and drawbacks which can be summarised as: (i) LIF @ 350 nm signals can be influenced by strong ELS from soot (as may be noted from the spectral responses reported in the Figure 3). (ii) LIF @ 445 nm signals can be affected by LII induced by 266 nm excitation and this is noticeable in the slight increase measured near the tip of the C/O = 0.77 flame. (iii) Despite these minor drawbacks, both techniques can simultaneously track ELS, LIF and LII in flames of different sooting propensities.

The LII profiles for the PMT4 region in the lower row of Figure 4.9 show some differences between the two measurement schemes and will thus be explored in detail below. The results for 266 nm excitation (both ICCD at 8 ns and PMT at 80 ps) show a trend of increasing signal with increasing HAB, albeit with different slopes. The LII signal on PMT4 from the 1064 nm pulse shows no signal until HAB ~ 5 mm, and then a steady linear increase further downstream. The signal between 560–590 nm on PMT4 is expected to be composed of both LII and LIF for 266 nm excitation, making the unambiguous attribution of any trends due solely to LIF or LII challenging [15, 33]. However, the signal on PMT4 from the 1064 nm pulse can be unambiguously attributable to LII and therefore differences between the 1064 nm pulse and 266 nm pulse on PMT4 can be attributed to LIF. Looking at Figure 4.9 it is possible to consider the influence of LIF is largely reduced at high HABs where the slopes of the ICCD signals and the PMTs become similar. Interpreting the 1064 nm pulse signal on PMT4 as LII, the profile in the lower RHS plot of Figure 4.9 confirms that LII is not detected for HAB less than about 5 mm, this being the region of the flame dominated by nanostructures rather than soot aggregates. It is notable that no LII signal was detected at any HAB with 1064 nm in the C/O = 0.67 flame.

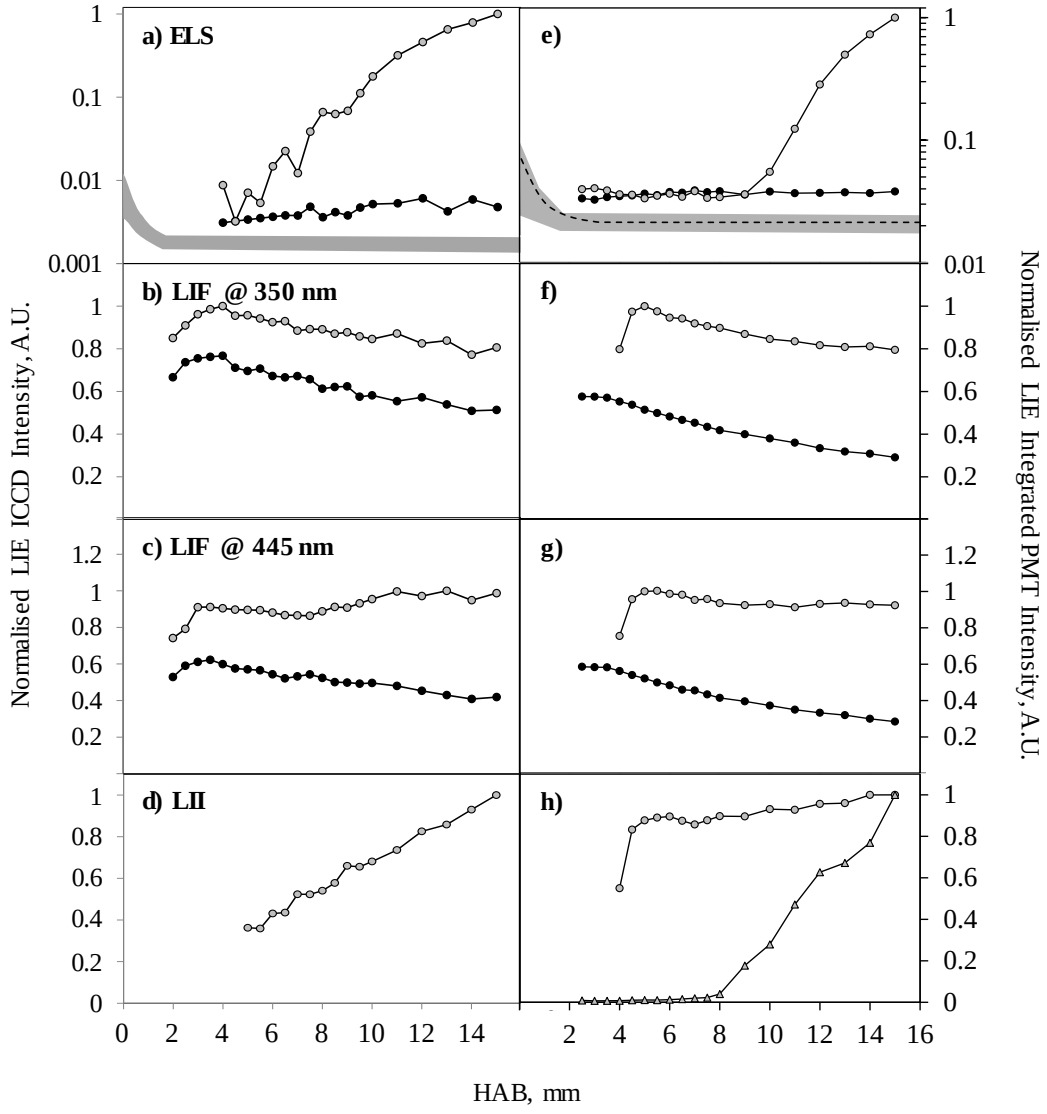

Figure 4.9: LIE signal integrated over 100 ns for the ICCD camera (left column, a, b, c and d) and for the PMTs (right column, e, f, g and h) for the C/O = 0.67 (black symbols) and C/O = 0.77 (grey symbols). h) shows 266 nm (80 ps) LIE (circles) and 1064 nm (8 ns) LII (triangles. Shaded grey areas (a and e) represent the gas phase ELS.

The proposed hypothesis for the difference between the 80 ps–266 nm pulse and the 8 ns–1064 nm signal on PMT4 is that the former is a combination of both LII and LIF, whereas the 8 ns–1064 nm pulse signal on PMT4 is only due to LII. The LIF component of the signal from the 80 ps–266 nm pulse is expected to decay relatively fast with a lifetime of approximately 5 ns (see decay time analysis below), whereas the LII component of the signal is expected to decay much slower, with a lifetime in the order of 50 ns and longer

[169, 224]. As the signal on PMT4 from the 80 ps–266 nm pulse is integrated over 100 ns, it is therefore expected that the initial component of the signal will consist mostly of LIF and a smaller LII contribution while the later parts will almost exclusively be due to LII. By beginning the integration of the signal from the 266 nm–80 ps pulse at progressively longer delays after the laser pulse, the proportion of LIF in the resultant signal will therefore decrease and the LII fraction will increase if the LIF and LII timescales are sufficiently separated. Starting the integration of the PMT4 signal at 10 ns, 20 ns, and 30 ns after the 266 nm–80 ps laser pulse, it is shown in Figure 4.10 that for increasing the initial integration time the trend obtained becomes closer to the LII profile obtained from 1064 nm excitation, until finally, over a 30–100 ns window the signal approaches the same trend found from the 1064 nm LII at HAB higher than ~9 mm. The results presented in Figure 4.10 confirm that the LII obtained from 266 nm excitation is indeed affected by LIF, where the LIF component of the signal may be gradually eliminated by judicious integration of the signal. The profiles plotted in Figure 4.10 were normalised by the peak value for better comparison. Once the correct integration window is applied to the signal on PMT4 from the 266 nm–80 ps pulse, similar trends to those obtained from 1064 nm LII can be obtained.

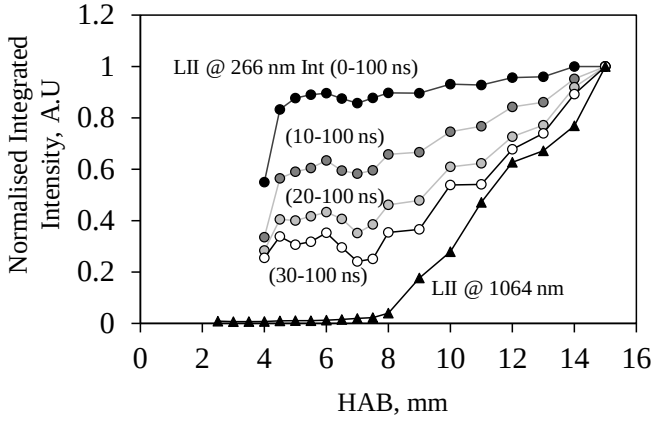

Figure 4.10: Normalised LIE signal collected on PMT4 (575 nm) with an 80 ps laser pulse at 266 nm (circles) integrated over different time range (see labels). Normalised LIE signal collected on PMT4 (575 nm) with 8 ns laser pulse at 1064 nm (triangles) integrated over 100 ns reported for comparison.

A key observation from Figure 4.9 is that a change in the trend of the profiles of ELS and LII measured with the 1064 nm laser in the C/O = 0.77 flame occurs at HAB ~ 6–8 mm. The ELS and LII profiles transition from an approximately constant level to a regime of a rapid increase at HAB~8 mm. The simultaneous increase of ELS and LII is evidence of a

growth process that eventually leads to the formation of large soot structures. Such a transition at HAB≳8 mm from a near constant value to a rapidly increasing level is not observed in the LIF @ 350 nm or the LIF @ 445 nm profiles. The UV and visible LIF display the opposite trends of transitioning from a region of rapid increase then to a regime of near constant value at HAB ~ 5 mm. Also, the ELS measured in the region where there is no LII, i.e., in the C/O = 0.67 flame or for HAB ≲5 mm in the C/O = 0.77 flame, is larger than that predicted for gas phase, which is shown as the shaded grey area in Figure 4.9. This finding of ELS in a region with no LII being significantly greater than the expected gas phase ELS is in agreement with previous measurements in flames at similar conditions [15]. The presence of excess gas phase ELS in region with no LII suggests the presence of small nanostructures that are not able to incandesce but can cause a non-negligible amount of excess ELS over that of the gas phase. Such nanostructures are also most likely responsible for the detected LIF signals which are generally attributed to aromatic structures, sometimes referred as soot precursors. The results reported in this Chapter point to the possibility that the LIF can be attributed to nanostructures, also referred as nanoparticles. The appearance of nanostructures between 1 and 10 nm with high number concentration before the onset of soot particles has also been confirmed by ex-situ measurements using nano-DMA or other scanning mobility particles sizers (SMPS)-like instruments by several groups [13, 35-39]. Furthermore, an evaluation of time decay of LIF signals measured here give further confirmation of the special role of the nanostructures as discussed below.

The axial profiles of the effective decay times (τ_{eff}) for the time-resolved LIF @ 350 nm, LIF @ 445 nm and LII signals are presented in Figure 4.11. The results are reported along the centreline for both the C/O = 0.67 (left) and C/O = 0.77 (right) flames. For the LIF @ 350 nm, values of τ_{eff} ~ 3.5 ns are obtained along the length of both flames with a variation of less than 0.5 ns. Similarly, for LIF @ 445 nm, the effective decay times are also approximately constant, but with a somewhat higher τ_{eff} ~ 5 ns. The LIF @ 445 nm decay times also feature slightly larger variations but still below 1 ns along the flame length and between flames, which could be possibly due to the influence of the LII signal at HAB > 7 mm for the C/O = 0.77 flame. For comparison, in the higher sooting C/O = 0.77 flame where the LII signal is sufficiently high, the LII decay times increase with HAB from 40 to 70 ns, which is consistent with the values reported in the literature for similar flames [23, 52, 53, 169, 224]. The horizontal dotted line in Figure 4.11 marks the effective decay time for PAH molecules, which is of the order of 0.5 ns [117]. It is evident from the results in Figure 4.11 that the measured LIF decay times of 3.5 to 5 ns are larger than those of molecular PAH yet much smaller than the LII decay times measured for soot.

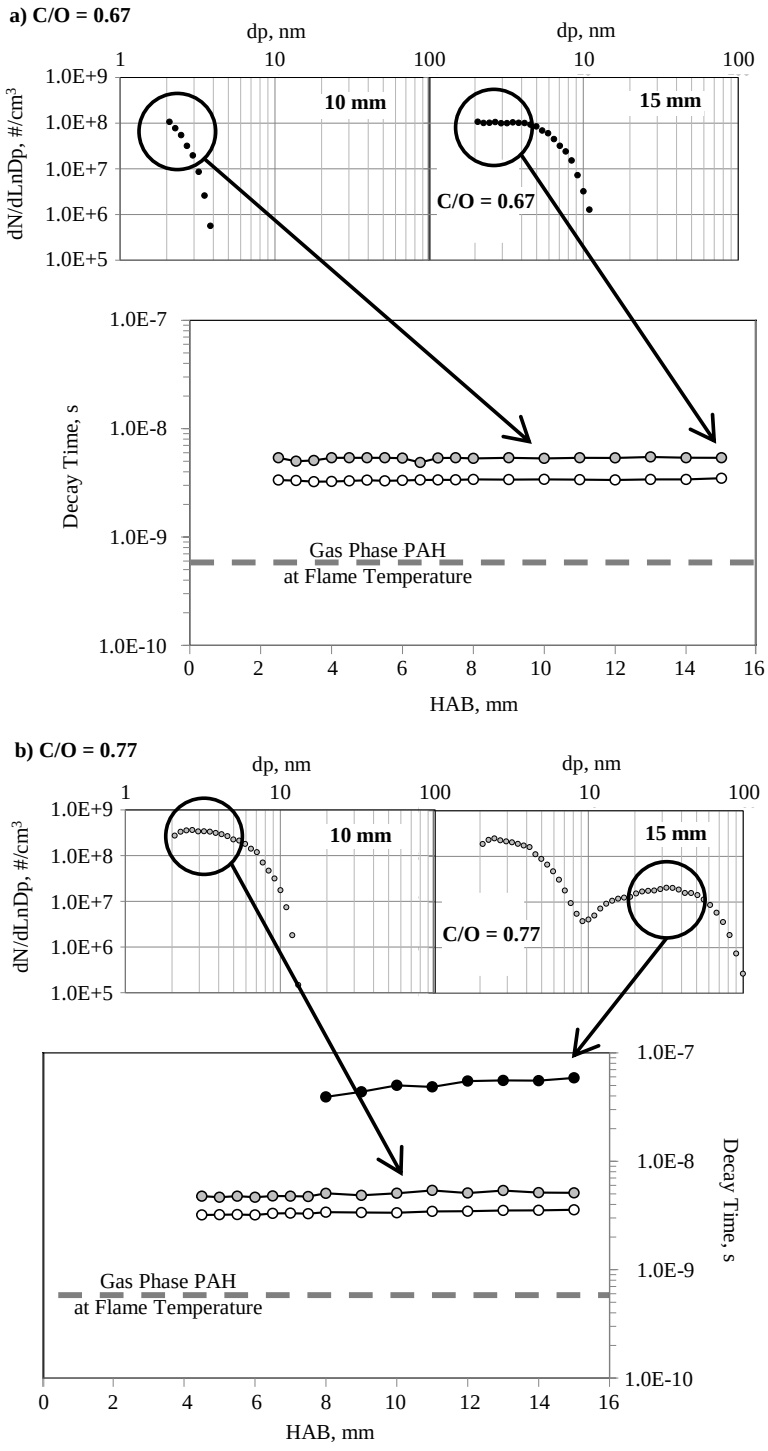

Figure 4.11: PMT signal decay times in the two McKenna burner flames for LIF @ 350 nm (○) and LIF @ 445 nm (●) with 80 ps laser pulse at 266 nm, and for LII (●) with 8 ns laser pulse at 1064 nm. PSDs measured in the capillary flames at determined locations are reported in the top panels. a) C/O = 0.67 and b) C/O = 0.77.

In the top row of Figure 4.11, the size distribution measurements are reported, with the circles identifying the dominant class of particle sizes which are responsible for the decay times shown in the lower part of the Figure. For the C/O = 0.67 flame, it is notable that the largest measured particle size in the particle size distribution (PSD) remains below 10 nm, with a significant peak around 2 nm and a shoulder that starts from 4 nm and reaches 7 nm moving from HAB = 10 mm to HAB = 15 mm. It is emphasised that no LII is detected in the C/O = 0.67 flame, which agrees with the finding that there are no particles larger than 10 nm in the PSD for this flame. The C/O = 0.77 flame displays a broad size distribution over a 10 nm range at HAB = 10 mm and becomes clearly bimodal at HAB = 15 mm, showing particles as large as 80 nm. It is worth noting that small particles with peak values around 2–3 nm are detected in significant amounts at HAB = 10 mm and HAB = 15 mm in the C/O = 0.77 flame. Particles larger than 10 nm are found in the C/O = 0.77 flame in small amounts at HAB = 10 mm and much larger amounts at HAB = 15 mm, corresponding to the trends found in the flame from LII.

The long LIF decay times relative to PAH molecules detected at all HAB for both flames can be explained by the presence of nanostructures with an aromatic character, where the size of the aromatic island, i.e., the number of the condensed aromatic rings, not larger than gas phase PAHs. These nanostructures correspond to the small nanoparticles detected with nano-DMA measurements (see arrows in Figure 4.11). According to the spectroscopic literature on LIF from PAH, in batch samples [136] and in cells [117], the consistently observed UV-centred LIF spectrum in the measurements suggests that a significant increase in the size of the aromatic island is unlikely, and the mean size of the aromatic island itself is not larger than pyrene. This attribution of the LIF signal to condensed phase nanostructures does not mean that some larger gas phase PAHs, e.g., 7 aromatics rings or larger, are not present, but rather, the relevance and contribution of such compounds in the process of formation and nucleation of particles is low. In fact, such species exist in smaller concentrations, compared to pyrene and smaller PAH [225, 226] and thus are unlikely to significantly contribute to LIF signals. Work by Bruno et al. [119, 122, 184] has also shown, perhaps more convincingly, that LIF in flames originates from structures up to 20 nm in diameter in many similar conditions through TRFPA. Although some gas-phase PAHs may contribute to the total LIF signal, it must be only a partial contribution given the longer decay time and UV centred spectrum can only arise from non-gaseous structures, i.e., a condensed phase. This is consistent with the analysis of the decay time of PAH dimers: the presence of a structure with intramolecular interactions increases the quantum yield, i.e., results in a longer light emission decay time. The presence of LIF in the visible region can be attributed to the red-shift due to the interaction between aromatic planes which is typical of dimers. Also, the presence of visible radiation can be a sign of progressive aromatisation processes that transition from the small nanostructure, with a

low aromatic character and liquid-like features, to soot particles with a marked aromatic character and a solid-state lattice structure. These considerations on the physical state of these nanostructures are supported by the absence of any LII signal, i.e. no solid lattice structure, and previous measurements by AFM analysis which has suggested that such nanostructures may also exhibit viscoelastic behaviour [23, 140, 145, 227].

4.3 Conclusion

Results from two experimental set-ups and two laminar flames burners are presented here to elucidate the behaviour of nanostructures as they evolve towards soot. Ex-situ measurements are presented along with spectrally and time-resolved laser emissions which include ELS, LIF and LII collected in flames of varying sooting propensities. From the measurements performed in different premixed conditions the following conclusions are drawn:

Nanostructures rather than soot primary particles and aggregates dominate the early regions of the flames at low HABs. Such nanostructures exhibit a monomodal distribution peaking around 2–4 nm and possess hybrid physico-chemical properties that are somewhat transitional between those of molecules and solid particles. They emit LIF, both in the visible and UV regions but not LII, yet their ELS level is higher than that of molecules but lower than that expected from solid soot particles. Similarly, the LIF decay times of these nanostructures are much larger than those of molecules, yet much smaller than those of soot LII.

Further downstream, nanostructures continue to exist along with soot as evidenced by the persistence of the LIF @ 350 nm and LIF @ 445 nm in conjunction with LII and excessive ELS. These nanostructures interact with larger soot particles although the nature of these interactions is not clear and warrants further investigations. The measured PSD confirm these findings showing bimodal distributions with one peak around 2–4 nm and another around 30 nm showing with particles in the range of 10 to 100 nm and above. The relative number densities between these two peaks change with distance along the flame length.

Collectively, these findings confirm nanostructures dominate the early evolution of soot formation in flames and behave in a hybrid manner, displaying a combination of molecular and solid particle properties and behaviour. The ensemble of similar and complementary techniques presented here highlight the success of the newly developed time-resolved LIE technique. This technique has been successful in simultaneously tracking of nanostructures ranging from near molecular size to soot particles up to hundreds of nanometres.

Chapter 5: Laminar Diffusion Flames

This Chapter explores soot formation in narrow coflow diffusion flames ranging from marginally sooting flames using methane as fuel to obviously sooting, non-smoking ethylene flames. In diffusion flames, the dominant transport processes and the structure of the reaction zones are different from those in the premixed flames, hence there is an impact on the mechanism of soot inception [15, 28-30, 51]. Soot formation in laminar non-premixed flames has been studied in burner configurations ranging from planar [228] to circular [42, 101, 116, 124] to counterflow [50, 51, 129, 229]. More recently, the axisymmetric burner developed at Yale University seems to have become the accepted platform and adopted by the International Sooting Flame Workshop (ISF) [200]. Many measurements on sooting flames for the burner developed at Yale University have been performed, however, studies pertaining to soot inception are limited primarily to LII [27]. The purpose of this Chapter is to shed light on the mechanism of soot inception in these diffusion flames through the application of time-resolved LIF-LII. Comparisons are made, where relevant, with previous measurements and computations for the same burner and earlier time-resolved LIF-LII findings reported for premixed flames. Diffusion flames possess a range of conditions that favour the chemical growth or physical growth mechanism for the formation of nanostructures. Physical dimerisation is known to prevail in the fuel rich pyrolytic zone, while closer to flame front, where oxygen and higher temperatures are present, the chemical growth mechanism is expected to be more effective [15].

5.1 Experimental Setup

There are some key differences in the experimental setup of the time-resolved LIE system and the burner used compared to that described in Chapter 4. The differences are outlined here.

5.1.1 Flame Conditions

The burner configuration adopted here, described in Section 3.3.1, was developed at Yale and consists of a 4 mm ID jet for the fuel mixture surrounded by a 74 mm diameter coflow of air. The bulk flowrate for both the jet and the coflow is common for all flames at 35 cm/s. A number of different sooting propensities are examined from marginally sooting methane flames [167] to obviously sooting ethylene flames [27, 213] and details of the conditions for the investigated flames are presented in Table 5.1 and photographs presented in Figure 5.1 . All but M80 are flames that are targets for the ISF [200]. Time-resolved, pointwise LIE measurements are conducted along the centreline of the flames and some select radial traverses are also presented for the ethylene cases.

Table 5.1: Axisymmetric coflow laminar diffusion flame details.

Flame	Fuel	Fuel flowrate (jet), SLPM	N_2 flowrate (jet), SLPM	Flame length, mm
M65	CH_4	0.172	0.092	28
M80	CH_4	0.211	0.053	37
E32	C_2H_4	0.084	0.179	25
E40	C_2H_4	0.106	0.158	32
E60	C_2H_4	0.158	0.106	50
E80	C_2H_4	0.211	0.053	74

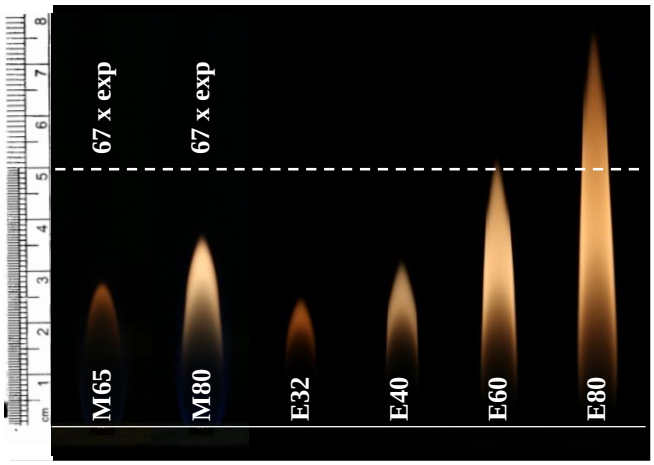

Figure 5.1: Photographs of all laminar diffusion flames. All photographs were taken at same $f_{\#}$ and exposure except for those labelled with extended exposure. Scale in cm.

5.1.2 Time-Resolved LIE

The 266 nm laser energy exhibited by the Ekspla laser at the probe volume for this study was measured to be 0.57 mJ/pulse, resulting in a fluence of 1.2 J/cm^2. The 1064 nm Quanta Ray laser was set to a fluence of 0.6 J/cm^2 as is the case for all the studies presented here. The slit of the spectrometer was set to 20 µm to keep all signals within the dynamic range of the oscilloscope. Each flame was measured incrementally along its axis and at each location, 500 instantaneous acquisitions were recorded and subsequently averaged. Some radial traverses were also measured to assess the formation of soot in the outer regions of the flame at selected heights. The 1064 nm pulse was delayed by over 900 ns after the 266 nm pulse. The reason for this dramatic increase in the delay over the 100 ns used for the premixed flames in Chapter 4 is due to the heavy sooting nature of some of these diffusion flames. As is discussed later, the LII component of the 266 nm LIE signal in heavily sooting regions of these flames becomes significant and take more than 100 ns to decay to negligible values. Thus, to avoid interference between the 266 nm LIE signal and the proceeding 1064 nm LII signal the two were sufficiently separated in time. As discussed in Chapter 4, there was no observed interaction between the two laser pulses that might complicate the interpretation of the LII emission. This conclusion was reinforced by the strong agreement shown between the current LII measurements and previously published SVF measurements by Smooke et al. [27]. Previous work on similar dual laser interactions also showed that there is little impact on SVF determination from LII measurements from the second pulse [150]. SVF presented in the present work uses the 1064 nm LII calibrated against the same ethylene flames data sets available on the ISF website [200] from the Yale

group [27] and does not account for variations in soot refractive index, gas composition and temperature.

5.2 Results and Discussion

5.2.1 Signal Processing

The data in these flames was processed slightly differently than that in Chapter 4 in efforts to unambiguously interpret the signals comprising the LIE. This was not an issue in the premixed flames of Chapter 4, where 266 nm originating LII contributed negligibly to the total 266 nm LIE on PMTs 2 and 3. This is not the case in the densely sooting regions of these diffusion flames. Figure 5.2 shows a typical temporally-resolved signal measured with PMT3, i.e. in the visible region of the LIF, in a zone where no LII is detected. The peak signal that appears only a few nanoseconds after the laser pulse, measured in volts, and can be used to measure LIF intensity. However, for the flames studied here, multiple signals, including LIF and LII, often coexist hence contribute to the peak value of the signal in varying proportions. This impacts the temporal location of the peak signal due to the different time evolutions of these processes in different locations and flames. All 266 nm excited signals reported in this study are based on a "prompt" signal approach, with the results based on the temporally integrated signal from 0 to 10 ns. This "prompt" approach allows the analysis of the component of the 266 nm excited signal that is dominated by fluorescence, rather than LII, and is not sensitive to the small variations in the rise and fall times for the LIF and LII components of the signal. Hence the "prompt" signal employed here provides a more consistent approach to comparing the 266 nm excited fluorescence at different locations and different flames, compared to simply utilising the peak or the integral of the signal. The "prompt" portion of the signal shown in Figure 5.2 is mainly composed of short-lived signals that exhibit a fast exponential-like decay. The "prompt" signal is reported in this Chapter is in units of V.ns (volts x nanoseconds), where the voltage produced by each PMT is corrected for the spectral throughput. The small amplitude ringing artefacts shown in Figure 2, evident at times > 10 ns, are due to transmission line effects generated by the impulsive nature of the signal. The node locations of the ringing artefacts in time are repeatable; hence they are present in the average signal shown in Figure 2. The ringing artefacts are more obvious in the presented signal from the M65 flame where signal levels are the lowest. However, they do not impact any of the results or throughout this thesis.

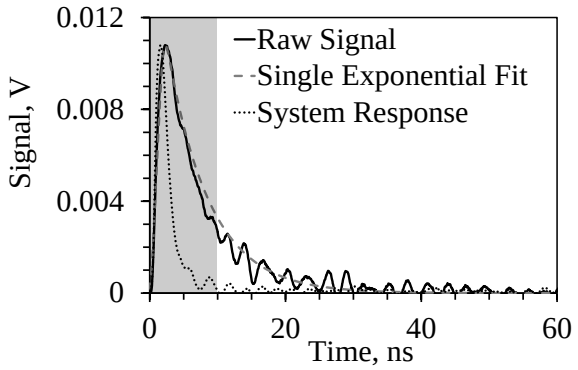

Figure 5.2: LIF Signal against time measured by PMT3 @ 445 nm in M65 at HAB = 22 mm (Solid) alongside single exponential decay fit (dashed) and measured system response (dotted). Also presented is the area considered for "prompt" signal (shaded).

In this study, LIF decay times were extracted using the simpler peak normalised integral method described in Section 3.2.1. The measured convoluted LIF signals are integrated from 0 ns to 200 ns and then divided by the peak. The decay times (τ_{eff}) determined with this method are presented herein. Whilst a bi-exponential fit has been used in previous work, a single exponential is more than sufficient in within these flames where LIF signals present no obvious bi-exponential features. A maximum error of 18% was found comparing a mono-exponential fit with the bi-exponential fit used previously in flat premixed flames in Chapter 4. The actual fitting error is far less than this as highlighted by the fit presented in Figure 5.2. When the UV and visible LIE signal is obviously bi-exponential, such as in the high sooting flame regions, specific decay times are not presented due to challenges of separating the components belonging to LIF and LII.

5.2.2 Methane Flames

LIE measurements along the centrelines of both the M65 and M80 methane flames are presented versus height above burner (HAB) in Figs. 5.3a and b, respectively, with the corresponding LIF decay times reported in Figs. 5.3c and d. The centreline profile of temperature is reported for flame M65 in Figure 5.3c is based on the temperatures computed by Walsh et al. [230]. These computations of temperature and major species were found to agree with Rayleigh thermometry measurements by Kempema et al. [167]. The M65 flame has a small, orange, low-luminosity tip from 23-28 mm HAB, indicating the presence of soot, albeit at low concentrations. LII resulting from 1064 nm excitation is shown in Figure 5.3a for the M65 flame, with the results suggesting that the local soot

concentration is below the detection limit. The very low soot concentration in the M65 flame shows that it is a good flame to analyse trend of the fluorescence intensity and decay time vs. HAB due to the very low potential interference effects from soot. The generation of the LIF signal above the background for the M65 flame begins at HAB = 10 mm, then increases at the same HAB where a rise in temperature is found in Figure 5.3c, indicating that the LIF signal is correlated with heat-releasing reactions in the flame. The LIF intensity, both at 350 nm and 445 nm in Figure 5.3a continues to increase with HAB towards the end of the flame before dropping off in the oxidation zone.

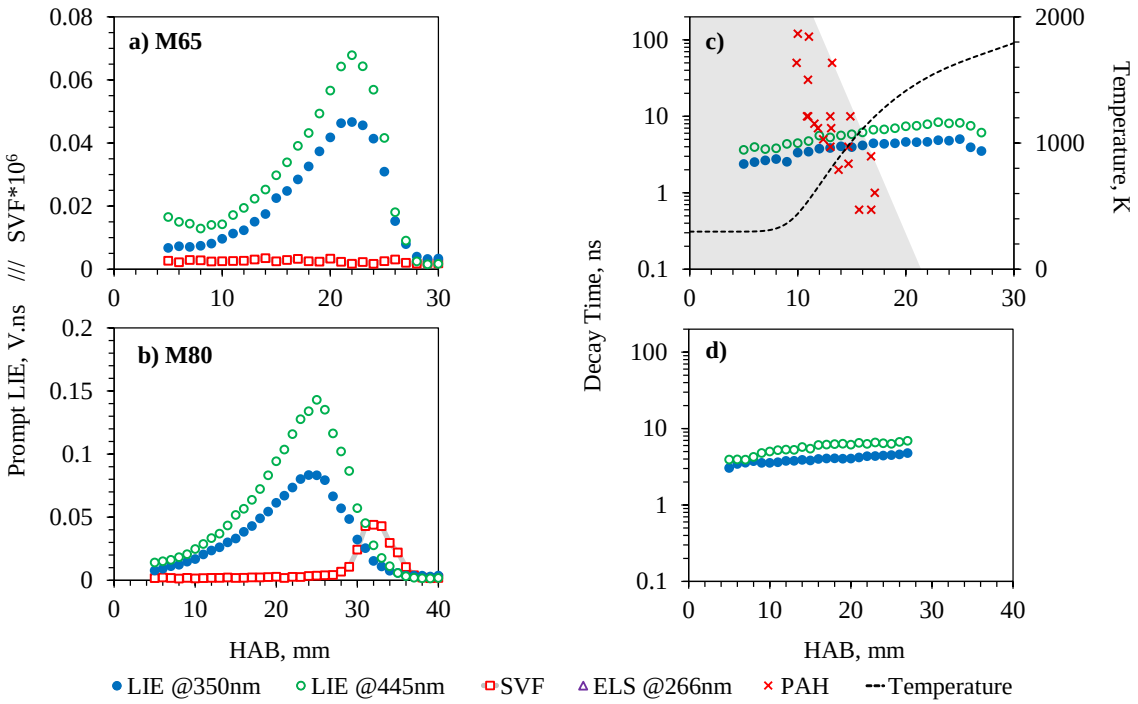

Figure 5.3: a) and b) Prompt LIE and SVF centreline measurements against HAB in methane flames. c) and d) measured LIF decay times plotted alongside molecular PAH decay times measured by Ossler et al. [117] corresponding to the computed temperature of the flame from the work of Walsh et al. [230].

UV excited LIF in sooting or near sooting flames, such as the M65 flame in Figure 3a has often been attributed to PAH molecules known to form in the soot inception region [26, 29, 116, 124]. Utilising previous measurements of PAH fluorescence decay time as a function of temperature, the measured fluorescence decay time and the flame temperature, it is possible to assess if the 266 nm excited LIF in the high aspect ratio diffusion flames explored in this Chapter are due to PAH. Utilising the temperature and the PAH decay time measurements of Ossler et al. [117], the decay times of naphthalene, fluorene, anthracene

and pyrene are plotted at the corresponding temperatures within the flame as shown in Figure 5.3c. A broad region representing the range of fluorescence decay times expected from PAH considering the variation of the decay time for different species and the temperature is shown in Figure 5.3c shaded in grey. Decay times for PAH larger than pyrene are not considered as their quantum efficiency, spectral emission and fluorescence decay time are not expected to be significantly different, and most probably exist in smaller concentrations, compared to the four representative PAH considered [225, 226]. The presence of strong quenching species such as O_2 and H_2O will only decrease the predicted PAH fluorescence decay times shown in Figure 5.3c. From the predicted PAH decay times shown in Figure 5.3c, a rapid decrease fluorescence decay time with temperature is predicted, with decay times less than 1 ns at temperatures approaching 1200 K.

Measured decay times for the M65 flame are shown in Figure 5.3c vs. HAB for both LIF at 350 nm and 445 nm, with decay times ranging from 2 ns near the burner exit to 8 ns near the end of the flame. In the low-temperature region of the flame at HAB < 10 mm, the measured decay times of 2-4 ns are much smaller than the expected PAH decay times of 10-100 ns. In the absence of strong quenchers such as oxygen, an explanation for the short decay time at HAB<10 mm could be due to CH_4 being a strong PAH quencher or the bulk of the UV LIF excited signal to not be due to PAH. Multiphoton photofragmentation of methane from 266 nm excitation is expected to be a very small contribution to the signal in the methane flames, however, due to the very low LIE signal levels in the M65 flame, it can be seen in Figure 5.3a that for HAB ≤ 7 mm, some of the 445 nm signal could possibly be attributed to CH_4 photofragmentation. From HAB 10-18 mm where the temperatures are less than 1000 K, the fluorescence decay times correspond to similar decay times expected from PAH at these temperatures. For HAB > 18 mm both decay times measured at 5-8 ns are much longer than the sub 1 ns decay times predicted for PAH at these temperatures. The significant difference in decay time indicates that the origin of the fluorescence certainly in the high-temperature region of the flame is from similar nanostructures found previously in premixed flames (Chapter 4). Hence the increase in LIF cannot be solely explained by a concentration increase of PAH because of the corresponding increase in decay time seen in Figure 5.3c. Previous measurements using time-resolved fluorescence polarisation anisotropy (TRFPA) [98, 122, 184] have also confirmed the presence of fluorescent particles with much larger effective diameters than molecular PAH in non-sooting regions of diffusion and premixed flames.

As both the 350 nm and 445 nm emission show a similar trend to each other for both the LIF “prompt” component and the fluorescence decay time for all HAB despite the large temperature charges, it seems reasonable to hypothesise that the nanostructures concluded to be responsible for the LIF for HAB > 18 mm are the same source of the fluorescence

emission for HAB < 18 mm, thus ruling out PAH emission as the source. Fluorescence decay times are a function of several variables including temperature, the concentration of quenching species and particle structure [51, 117, 136] and thus attempts to attribute decay times to an average particle size would be speculative, without further information. However, it would be reasonable to assume that these nanostructures are somewhere between 1 nm and 10 nm diameter as previously observed in both lower aspect ratio diffusion [122, 184] and premixed flames [98] (Chapter 4).

The centreline LIF measurements for the M80 flame are shown in Figure 5.3b, which show a very similar centreline trends to the M65 flame, with the exception of a detectable SVF. The M80 flame is visibly sooting, with 1064 nm excited LII observed from HAB = 29 mm to the tip at 37 mm. In the sooting region of the M80 flame, the LIE signals from 266 nm become a combination of LIF, LII and potential interferences from sublimated species such as C_2 and C_3 [183]. The impact of the emerging 266 nm LII signal results in a steep increase in decay time measured where LII is detectable. Interpreting the decay time in the sooting region becomes difficult and the current method is no longer appropriate due to obvious multi-exponential components to the signal. For this reason, decay times are not presented in these regions (HAB > 28 mm) where multiple LIEs contribute to the signal. Metrics that rely on longer integration times, such as the decay times are greatly affected by the LII component of the signal, however, the "prompt" part of the signal as used in Figure 5.3b is still very much dominated by LIF in this low sooting flame. Prior to the onset of soot, the decay time for the M80 flame in Figure 5.3d, displays a trend of increasing LIF decay time with increasing temperature, similar to the M65 flame. Even though temperature measurements are not available for this flame, the temperature profile can be expected to be similar to that seen in M65. In the high-temperature regions of the flame the LIF decay times in this flame are again much larger than that expected of molecular PAH at high temperatures, and thus can be attributed to nanostructures.

Based on the rise and decay of LIF in M65 and M80 flames, some similarities and some differences can be observed. The LIF signal increase is quite similar in terms of slope once normalised by the maximum value, which suggests that the formation process in both flames involves the same pathways. However, it is interesting to note that in the M65 flame where no LII is detected the LIF signal rapidly decreases approaching the oxidation zone and thus the end of the flame. On the other hand, in the M80 flame the LIF decrease appears to decrease at a lower rate with respect to HAB, suggesting that in these conditions the small nanostructures are converted in soot before the oxidation zone and only after that the oxidation takes place. No ELS was detected above the system sensitivity limit for the M65 and M80 flames despite there being a detectable, albeit small, amount of soot from 1064 nm excited LII found in the M80 flame. The detection limit of ELS is a result of the huge

range of ELS signal levels present in these sooting flames. Because in the heavily sooting flames ELS intensity rises orders of magnitude higher than the background gas phase it is difficult to finely resolve lower ELS levels. Further measurements with higher sensitivity would be required to determine if any emissions in the region of 250-280 nm on PMT1 are due to elastic scattering or LIF, which is known to extend down to at least 280 nm [51] or lower [99].

5.2.3 Ethylene Flames

Similarly to methane flames, LIE measurements along the centreline on the set of ethylene flames are presented in Fig 5.4. Due to the wavelength and intensity of the 266 nm laser used, photofragmentation of ethylene was observed close to the burner exit producing a signal proportional to ethylene concentration on all the PMTs. Assuming that 100% of the LIE signal recorded by all PMTs before the reaction zone is due to photofragmentation, the "prompt" signals are corrected based on ethylene concentration and consumption. The consumption of ethylene is computed by simple CANTERA [231] (open-source chemical kinetics software) diffusion flame calculation using the GRI 3.0 mechanism for computing species which is then matched to the temperatures of Smooke et al. [27]. Figure 5.5 shows this correction performed on the E32 flame, as an example, as this is the flame with the most severe correction. The "prompt" signal correction method employed does not remove any contribution of the ethylene fragmentation signal on the temporal decay. To avoid erroneous interpretation in Figure 5.4, decay times have been excluded for the ethylene flames close to the jet exit plane where decay times are expected to be impacted by the presence of photofragmentation. Additionally, due to the higher sooting propensity of ethylene flames, the "prompt" LIF and LIF decay times in the downstream regions are also challenging to interpret due to the presence of interferences from soot. As with the M80 flame, the decay times deemed to be impacted by LII are omitted. In all the ethylene flames investigated LII has been detected, which is not surprising due to the higher sooting propensity of ethylene compared to methane. Unlike the methane flames, ELS is detected above the system sensitivity for all the ethylene flames and shown in Figure 5.4 on a logarithmic scale to enable trends in ELS to be observed over a wide dynamic range. Error bars are placed on the ELS measurements presented in Figure 5.4 to show the potential LIF contribution to the ELS signals. It is known that LIF signals extend down deep into the UV [51], around 280 nm, and thus can be present on PMT1. In sooting regions of all flames this deep UV fluorescence signal contributes negligibly to the ELS signal. However, at low HAB where ELS is low, and LIF signals are at their peak, the interference of LIF on PMT1 can be significant.

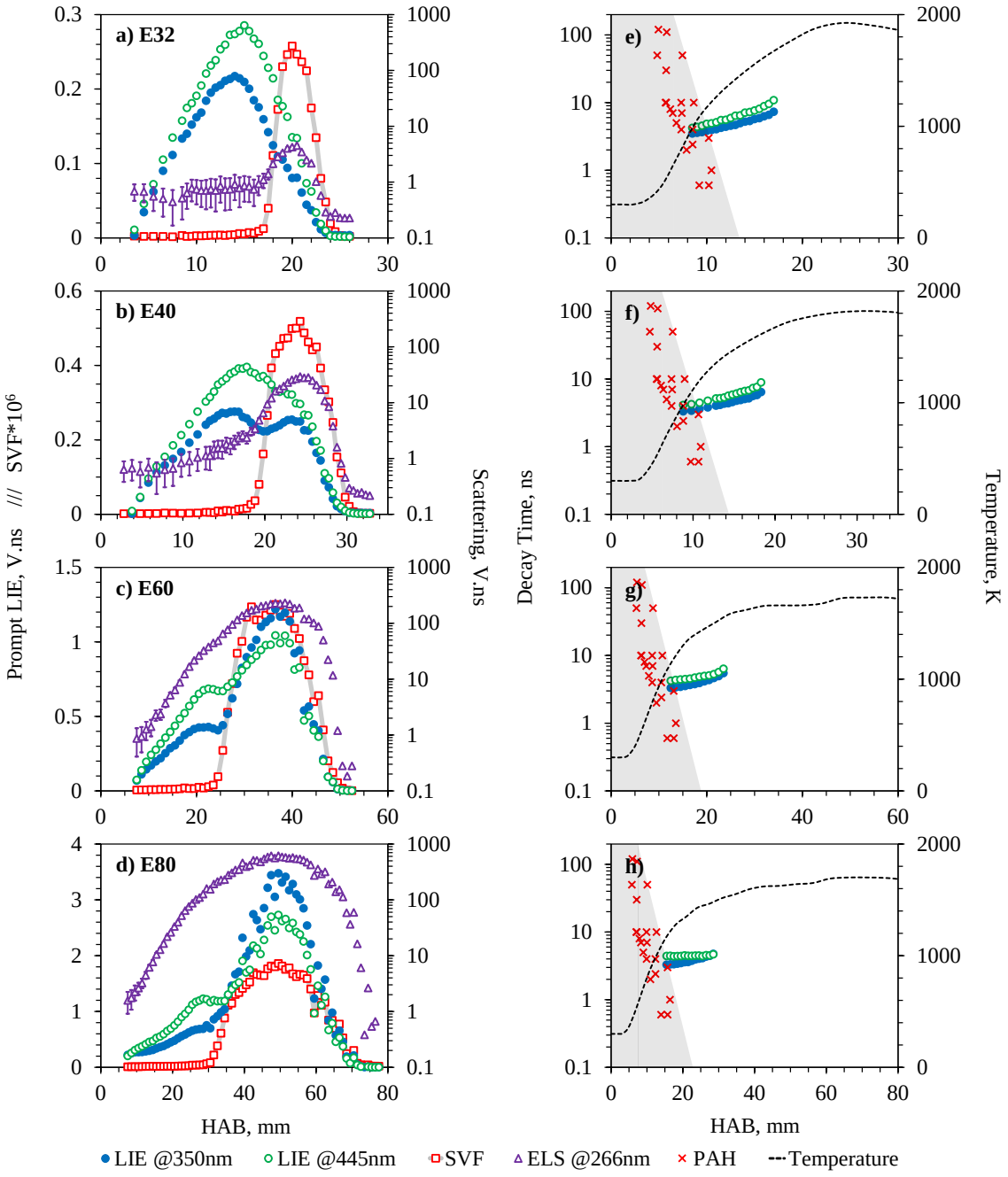

Figure 5.4: a), b), c), and d) Prompt LIE and SVF centreline measurements against HAB in ethylene flames. e), f), g) and h) Calculated LIF decay times plotted alongside molecular PAH decay times measured by Ossler et al. [117] corresponding to the computed temperature of the flame from the work of Smooke et al. [27].

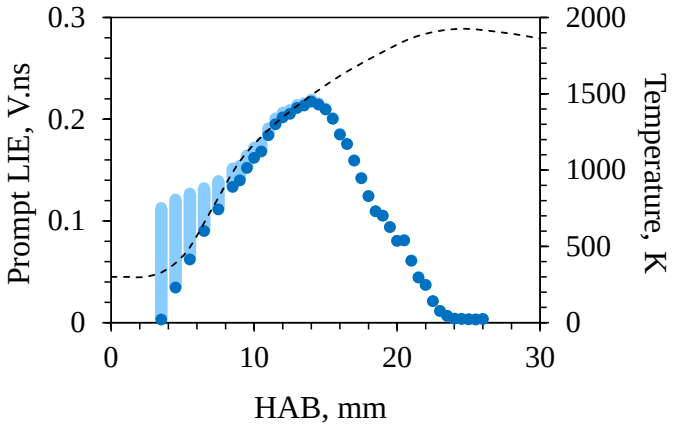

Figure 5.5: LIE @ 350 nm with ethylene correction (●) and without correction and difference as faded (●). Corresponding temperature also presented (dashed).

For the lowest ethylene concentration case, the E32 flame reported in Figure 5.4a and e, some similarities in the LIF profile compared to M80 can be seen: LIF reaches a maximum (around HAB = 14 mm for the E32 flame) before the occurrence of soot and continues to decrease with HAB when soot is detected with LII (at HAB = 18 mm for the E32 flame). The LIF signal decays to the background level at the end of the oxidisation region at the same HAB where no more LII from soot is present in both flames. Despite the broad similarities of the structure of the LIF vs. HAB for the E32 and M80 flames, the E32 flame features LIF intensities double that of the M80 flame and SVF levels approaching an order of magnitude greater than the M80 flame. The increased soot formation results for the E32 flame indicate that while coagulation of smaller nanoparticles is important for continued soot growth the mechanisms of surface growth is becoming more dominant in the ethylene flames. A detectable ELS signal is evident in the E32 flame, with uniform scattering signal in the non-sooting region where no LII is detected, progressing to a peak that correlates with the location and width of the sooting region.

Measurements in the E32 flame highlight the signal valley created between the peaks of UV LIF and LII signals which is often referred to as the “dark region” which has been observed in several studies [95, 116, 124, 232]. The rapid decrease of UV LIF before the occurrence of soot shows a strong resemblance to the trend of UV absorbing nano-organic carbon (NOC) measurements conducted by D’Anna et al. [101] in diffusion flames that have a particle size range estimated to be between 2 nm and 4 nm. Complementary investigations by the Naples group [122, 184] show that particles in this “dark region” have a higher quantum yield at longer wavelengths, compared to the nanostructures observed upstream of this region. Consequently “dark region” particles exhibit longer fluorescence

emission wavelengths and have sizes up to 20 nm measured through TRFPA. Relative to the marginally sooting methane flames, the ethylene flames feature a larger fluorescence intensities and longer fluorescence decay times. Considering that the fluorescence signal from nanoparticles can be considered to be proportional to the number of nanoparticles [186], the significantly higher LIF signals found in the ethylene flames compared to the methane flames can be attributed to a greater nanoparticle concentration. By virtue of the higher nanoparticle concentrations in the ethylene flames, particle coagulation rates will be increased, creating larger particles that are still capable of fluorescence emission. The enhanced production of larger nanoparticles in the ethylene flame compared to the methane flames agrees with the findings of longer decay times in the ethylene flames, hence larger nanoparticles.

Moving from the E32 flame to the higher sooting E40, E60, and E80 flames, a strong increase in the ELS signal with HAB in the regions where no soot is detected, as shown in Fig 5.4b, c and d. The rapid initial increase in ELS with HAB in the non-sooting region of the flame along the centreline is faster than the growth of the LIF signal and suggests that in the early zone of a diffusion flame, it is possible to find fluorescing nanostructures with sizes that can vary from 2 to 20 nm [184] which would contribute to a significant ELS signal in excess to the gas phase. The formation and growth of these small nanostructures are influenced by the abundance of gas phase molecular precursors such as PAH, hydrocarbon fragments and acetylene which increases with ethylene concentration in the fuel stream. Because of increasing fuel concentration in the ethylene flame series, the flame length increases and thus so does the residence times of nanoparticles in the pyrolytic region. Due to the increased residence time and precursor concentrations, the reaction pathways lead to more abundant and slightly larger nanostructures in the non-incandescent parts of the flames in the ethylene flames. It is also worth noting that ELS continues to increase after the first LIE peak and before the onset of significant SVF, suggesting that nanostructures continue to grow in the “dark region” with larger ELS cross-sections, in agreement with previous work [122]. Note, the smoothness of the axial traverses in the E80 flame was slightly compromised by some flame flickering resulting in the less smooth LIE trends presented in Figure 5.4d.

The decay times measured along the centreline of the ethylene flames are presented in Figs. 5.4e, f, g and h, showing that they are larger than those expected for gaseous PAH [117] at the given flame temperatures < 900 K [27]. Although the computed temperatures presented in [27] were not found to be unanimously in agreement with thermocouple measurements, strong agreement was shown in the location and magnitude of the initial rise in temperature along the centreline [233] and thus makes them suitable for this purpose. Decay times increase with HAB for all flames, although the E80 flame only shows a marginal increase

in decay times and maintains relatively low decay times in comparison to all the other flames studied here. It would be difficult to use decay times to provide useful information on particle size or structure without further information. ELS, on the other hand, provides an obvious indication that nanostructure size is generally increasing with HAB and in flame conditions that lead to higher SVFs.

Considering only the LIF measurements before the onset of soot by the detection of 1064 nm LII, the evolution of the spectrum emitted by the nanostructures can be explored through the ratio of LIF @ 350 nm and LIF @ 445 nm (UV/VIS). The UV/VIS LIF ratios are presented in Figure 5.6 with the two methane flames presented in Figure 5.6a and ethylene flames in Figure 5.6b. For the non-sooting M65 flame, the UV/VIS ratio remains close to 0.75, after an initial rise, corresponding to a LIF spectrum likely peaking between 350 nm and 445 nm, suggesting that the fluorescent structures on the nanoparticles are primarily comprised of smaller aromatic species not significantly larger than pyrene, based on this rough spectrum [26, 115, 185]. On these considerations, the resulting spectra are more skewed towards PAHs with a small number of rings when considering the redshift of PAH LIF at high temperatures [117]. Because this ratio does not change, it indicates that there is no significant evolution in the nanostructures towards more aromatic features when moving downstream. Interestingly this lack of evolution coincides with the absence of detectable 1064 nm LII, suggesting that the evolution toward soot particles from these small nanostructures might need to first step into an aromatisation process, and exhibit a redshift in its spectrum. In contrast, the M80 flame ratio is initially close to 0.75 and then decreases moving downstream, indicating a shift in the spectrum towards longer wavelengths and consequently an increase in the size of the dominant aromatic island responsible for LIF, similar to that observed by Hayashida et al. [124] and Kobayashi et al. [232]. It could also be possible that these nanostructures evolve towards a more graphitic structure, having layers of small aromatics stacked, as has been found in lower temperature pyrolytic zones [51] which could explain the redshift of the signal. The decrease of the LIF signal intensity in the downstream region can be attributed partially to a decrease of the quantum yield of the nanostructures, and of course to the evolution towards soot particles, i.e., to larger structures having the capability to emit an LII signal rather than LIF. This second aspect would be confirmed by the rise of the LII just after the decrease of the LIF signal and would follow the known growth pathway for the combustion-generated particles.

The sooting ethylene flames all exhibit a similar transition towards a red-shifted spectrum with increasing HAB as shown in Fig 5.6b. Considering all the ethylene flames, the LIF ratio moves to lower values with increasing HAB, a similar trend but a greater shift compared to the sooting M80 flame. In the E60 and E80 flames, the LIF ratio decreases to

ultimately lower ratios downstream indicating that in the pyrolytic formation of soot, higher soot concentrations are preceded by nanoparticles comprised of aromatic fluorophores with increasing ring numbers and more rigid structures. Comparing the methane flames with ethylene flames, the LIF ratio reaches a similar low value of around 0.55 in both M80 and E80 before the onset of soot, with the E80 flame being much more heavily sooting than M80. The red-shifted spectrum for both the M80 and E80 flames is due in part to the relatively large residence times that these nanostructures have before soot starts and confirms once again the important role of the residence time in the study and the determination of the evolution of the particles in flames.

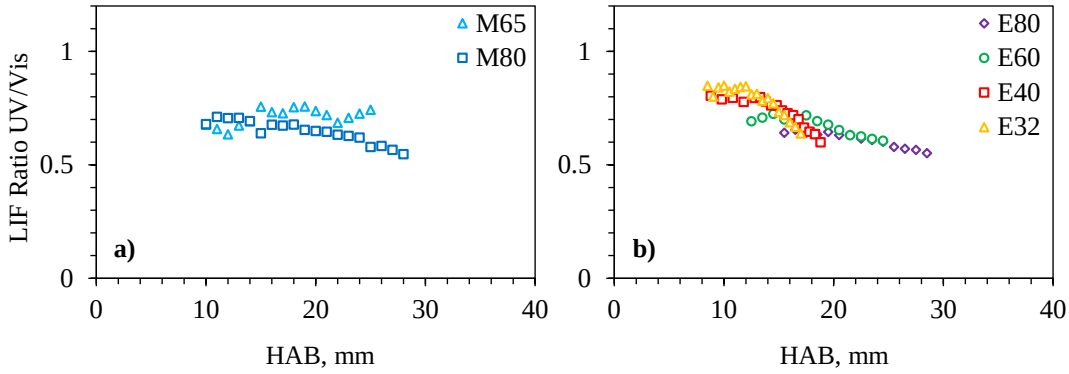

Figure 5.6: LIF ratio UV/Visible against HAB a) methane flames and b) ethylene flames.

As seen in Figure 5.4, cases E40, E60 and E80 present a dual peak (bimodal structure) in the LIF measurements traced along the length of the flame. Because the 266 nm LIE measurements are being used to quantify the soot nanostructure based on the LIF signal, it is important to understand if this particular feature is genuine or an artefact due to interferences from other emissions. LII is known to contribute a non-negligible amount to the total (0 – 200 ns) integral 266 nm LIE signal even in the flames of lower SVF (E32 and M80) due LII's impact on signal decay time determination.

In order to assess the correlation of the later stages of the 266 nm LIE signal with LII excited with 1064 nm and previous SVF measurements [27] a comparison of these signals is shown in Figure 5.7. The temporal tail of the 266 nm LIE signal at 575 nm is defined as the integral of the signal between 60 and 200 ns where the LIF contribution of the signal has decayed to negligible values, similar to that explored in Chapter 4. Both peak and integrated 1064 nm LII signals for the E60 flame are reported which agree well with previous SVF measurements [27]. All curves in Figure 5.7 are normalised to have their maximum value of unity. The similarity of all the curves in Figure 5.7 indicates that soot

particle size and differences in bath gas composition have a minimal impact on the determination of SVF whether peak, “prompt” or longer integrated signal are used. The remaining part of the 266 nm LIE signal (0 to 60 ns) will still contain LII alongside any LIF. In the higher sooting flames (E40, E60, and E80) the location of the second “prompt” LIE peak strongly correlates with the location where 1064 nm LII is measured. Thus, it would be reasonable to assume that a significant portion of this “prompt” signal in the second peak is driven by the interaction of 266 nm with soot. While LII from 266 nm excitation is expected, the “prompt” LIF HAB trend does not completely correlate with 1064 nm LII, as shown in Figure 5.4.

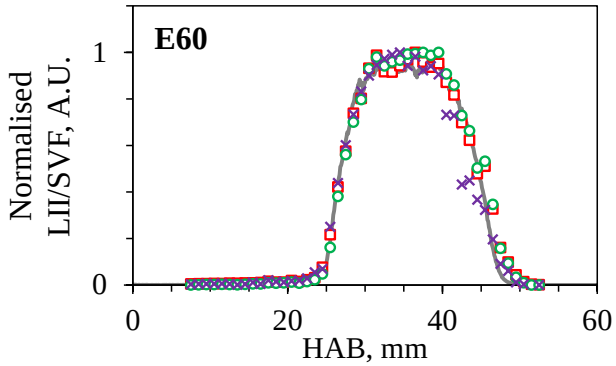

Figure 5.7: LII comparison in E60 flame. All measurements are normalised by the maximum value. 1064 nm LII peak (□), 1064 nm LII integrated 0-200 ns (○), 266 nm LIE integrated 60-200 ns (X) and SVF determined from LII (solid line) by Smooke et al [27].

Whilst the second peak in the “prompt” LIE signal in the highly sooting ethylene flames cannot be solely attributed to 266 nm LII, it is possible that it is due other interactions of the 266 nm pulse with soot. With the use of 266 nm and particularly at the intensity utilised in this work, it would be expected that sublimation and possibly some photo-dissociation processes of soot would lead to the ejection and subsequent excitation of C_2, C_3, carbon clusters and possibly other molecular species resulting in a fast LIE signal. Although care was taken to place the PMTs away from regions in the spectrum known for significant peaks due to C_2 swan bands and C_3 swing bands [176, 183], some overlap is possible given the 30 nm collection bin of each PMT. A few studies using deep UV laser wavelengths (193 nm and 248 nm) have shown that a substantial mass loss and particle disintegration from soot can occur even at modest fluencies with little particle heating [179-181]. Even though a single photon at 266 nm (37595 cm^{-1}) does not have enough energy to break a σ bond between carbon atoms in a soot particle which has a bond energy of 43800 cm^{-1} such

as a 193 nm photon does (51814 cm^{-1}), it is possible that similar processes might possible through a multiphoton interaction due to the short 80 ps 266 nm laser pulse.

In order to better understand the signal components from UV excitation where soot is present, the E60 flame at a HAB = 35 mm is explored with a variety of 266 nm laser energies, with a particular focus on the "prompt" LIE signal in a heavy sooting flame region. The same UV laser and optics as outlined in Chapter 3 were utilised for this test so the spot size did not change. However, the laser fluence was varied from 0.11 to 4.2 J/cm^2 by changing the laser energy with the half-wave plate polarisation cube combination.

The response of the LIE signal at 350 nm is presented in Figure 5.8a in the time domain for a range of fluence levels. The signals are presented with a logarithmic vertical axis to highlight the similar features of the signals over a broad dynamic range. It is evident from Figure 5.8a that all the signals display a broadly similar behaviour with the initial portion of the signal featuring a fast rise and fall close to the system response limit. The initial fast rise and fall portion of the signal over the first few nanoseconds cannot be attributed to LIF from the same nanostructures observed in other upstream non-sooting regions of the flame as the time decay is much shorter. The initial fast rise and fall portion of the signal is only significant where the SVF is large and thus was not found as an interference source in previous studies of premixed flames in Chapter 4 where sooting levels were much lower. After the initial rapid rise and fall, the signal exhibits a gradual decay that is expected to be from a combination of LIF and LII, with LII dominating the signal at times greater than 20 ns. The LII dominated portion of the signal for all fluence levels displays a similar decay rate, indicating that only a small amount of the total soot mass is sublimated even for the highest fluence case of 4.2 J/cm^2.

In order to quantify the relative emission intensity at different times, the signal for each fluence level is integrated over three different windows in time as presented in Figure 5.8b. The first window from 0 to 3 ns represents the fast rise and fall component, the second window from 3 to 10 ns represents the portion of the signal where nanostructure LIF would be expected to be significant and the third window from 60 to 200 ns represents the segment of the signal that is due to be exclusively from LII. The integrated signal in each of the three windows has been normalised such that the integrated signal in each window at a fluence of 1.2 J/cm^2 is unity to be consistent with the fluence used for all other measurements reported in this Chapter. A dashed line in Figure 5.8b is shown to indicate what would be an ideal linear response with the laser fluence.

No correction has been made for the expected LII interference component in the first and second windows, or for any nanostructure LIF onto the first window. Although the total number of photons received from LII is large over the entire signal duration, the number

of photons received from LII in the first window is expected to be relatively low, based on estimates achieved by extrapolating the approximately exponential decay of the LII from later time stages (> 20 ns), noting that an exponential decay is a straight line in the log-linear Figure 5.8a. An accurate correction in the time domain for LII interferences is not possible, as there is expected to be a portion of the LII signal that rises and falls rapidly at the system limit response. A fast initial LII signal will be present when the surface of the smallest incandescable soot particles [43, 234] is at a temperature sufficiently close to the soot sublimation temperature and the laser pulse is present to drive sublimation. During the laser pulse, it is possible that the smallest particles will be losing significant mass due to sublimation and will produce a strong signal that is only present when the laser pulse is present. The third window in Figure 5.8b represents the LII, the response of this region with fluence is a power law like with an exponent less than unity, which is expected for an LII process progressing from the linear regime to plateau regime [43, 174]. As the spatial profile of the 266 nm beam is Gaussian-like and not strictly a flat-top profile, a region of zero or negative slope with fluence is not observed in Figure 5.8b even at the highest fluence levels examined.

The signal in the first window displays a near linear trend with the laser fluence up to 1.7 J/cm^2, which indicates that the origin of the signal in this window is not strongly dependent on LII. It is possible the origin of the high-intensity initial portion of the signal is either fluorescence of aromatic compounds coating the soot particles being volatised or excitation of sublimation products. Even for the lowest fluence level examined 0.11 J/cm^2, some sublimation will be expected to occur. For fluences larger than 1.7 J/cm^2 in the first window, the sub-linear fluence dependence is due to either saturation effects of the material being fluoresced or the saturation of the mechanism causing the production of the material being fluoresced. Further experiments with additional techniques will be required to definitively determine the origins of the fast high-intensity signal in the first temporal window region.

The signal in the second temporal window where LIF from nanostructures is expected to contribute features a sub-linear power dependence indicating that there is some LII present in this region but not so much as to completely correlate with the trend observed for the third window that is expected to be exclusively from LII. The signal found in the 3-10 ns region would appear to have component with a decay time that is comparable to nanostructure LIF found in upstream regions where soot is not present. The “prompt” signal from 0-10 ns which is a combination of the first and second windows in Figure 5.8b is used for much of the analysis in this Chapter. As such it is important to ascertain the nature of any SVF based interferences on this measured whether they are LII based or other mechanisms which is proportional to SVF. A short LII signal generated by means of soot

mass loss is still emitting quasi-blackbody emission and thus should emit a larger intensity @ 445 nm than at @ 350 nm, corresponding to a black body temperature of 3500-4500 K [30, 43-47]. Such blackbody emission is not present in Figure 4c and d, where the "prompt" LIE @ 350 nm is greater than that @ 445 nm in the sooting regions of E60 and E80 flames. The "prompt" 266 nm LIE signal that comprises the second peak is without a doubt not solely due to LII.

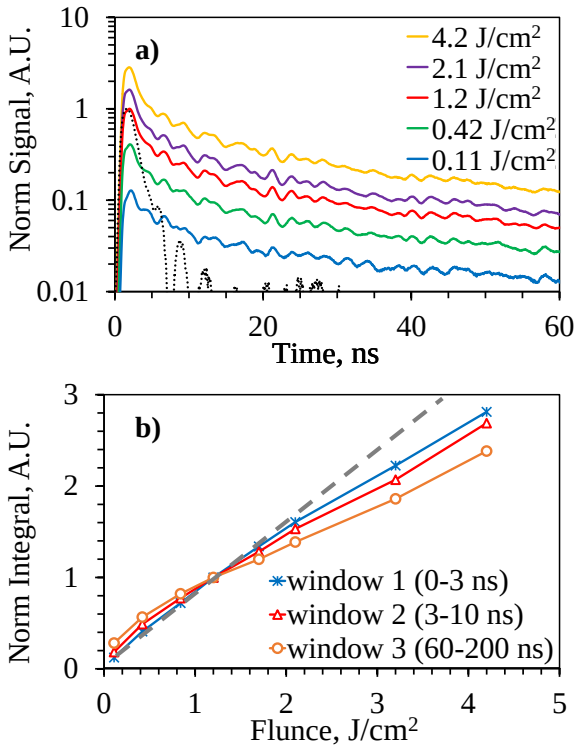

Figure 5.4: 266 nm LIE emission @ 350 nm in a high-sooting region (E60 at HAB = 35 mm) for a range of laser fluence levels alongside system response (dotted). a) Signal level vs. time and b) relative emission in three temporal windows.

If the interference on the "prompt" LIF signal occurs as a result of LII or other mechanisms that are related to the presence of soot, then it is possible a correction can be made for this interference source based on the local SVF. To determine if a relationship between the interference on the "prompt" LIF and the SVF is consistent for all flames at all locations examined, the "prompt" LIF signal at 350 nm vs. the SVF is shown in Figure 5.9. The SVF in Figure 5.9 is determined from the delayed integral (60 – 200 ns) of the 266 nm LIE measurement at 575 nm as correlated in Figure 5.7. If all data in Figure 5.9 were to sit with minimal scatter on some curve (linear or other) with respect to SVF, then that would indicate that most of the "prompt" LIF signal is due to interferences from soot. Equally, if

a large scatter exists in the data with realisations with very low "prompt" LIF and large SVF, then that would indicate that there are negligible soot interferences in the "prompt" LIF signal. However, what is found in Figure 5.9 is that there is a group of data points sitting on a linear positive slope line which is termed here as the interference limit line. Below the interference limit line, no data points are observed and above this line data points with a broad range of "prompt" LIF and SVF values are found. The interference limit line represents the maximum interference from soot, such that LIE values that lie on the line are potentially 100% soot-derived emissions, whereas values above the line contain some genuine LIF. As the interference limit line, shown in in Figure 5.9 is linear, this indicates that the "prompt" LIF interference mechanism is linearly proportional to the SVF. This further implies the mechanism for the interference is more likely due to sublimation rather than surface ablation or ejection of volatile compounds from the surface of the soot. If the interference was due to surface ablation, then the expected dependence would be an interference line with a power law relation ($SVF^{2/3}$). This is because the relationship between the approximately volumetric LII processes ($\propto d^3$) and the surface process ($\propto d^2$) of ablation. This dependence on ($SVF^{2/3}$) was not observed, thus ablation is not likely to be the source of interference. As the interference limit line is consistent across all flames at all locations, it indicates that the correction with SVF is essentially independent on the structure of the local soot for the conditions examined. A similar trend and scatter to the 350 nm data presented in Figure 5.9 exists for the "prompt" LIF @ 445 nm with SVF.

Utilising the interference limit line for the 350 nm and 445 nm PMT data, a correction for soot interferences has been applied to the "prompt" LIF measurements presented in Figure 5.10. The difference before and after the soot interference correction applied to the "prompt" LIF signal is shown in Figure 5.10 to illustrate the region and extent of the correction. It is evident that the SVF correction works well for flames E32 and E40 so that the "prompt" LIF is reduced to very low levels where soot occurs. Flames E32 and E40 present similar corrected LIF trends to the non-sooting M65 flame and the uncorrected M80 flame where 1064 nm LII is detected, exhibited in Figure 5.3a and b. Here there is no second increase of LIF where soot is detected; the LIF signal continues to decrease suggesting an evolution of the small nanostructures into large soot particle and aggregates. A decrease in LIF intensity is also present in the heavier sooting ethylene flames just prior to the second peak and hints at a similar trend of decreasing detectable nanostructure concentration where soot starts to be present in appreciable amounts.

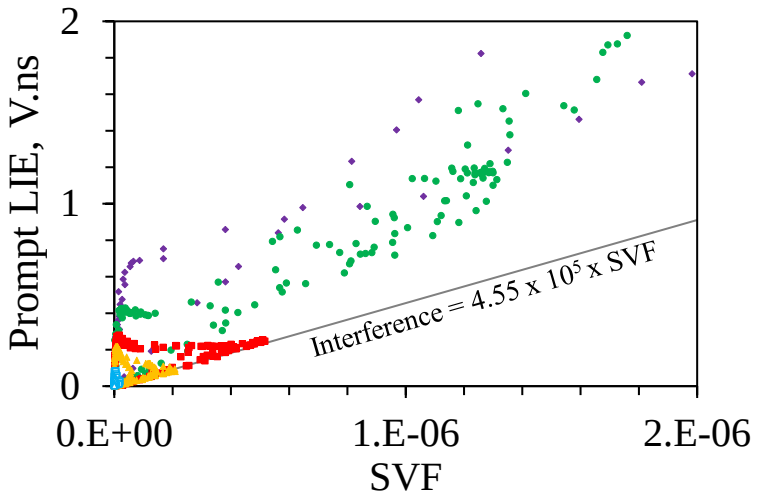

Figure 5.9: Scatter plot of prompt LIE vs. SVF. M65 (Δ), M80 (□), E32 (▲), E40 (■), E60 (●) and E80 (♦). SVF maximum linear interference extrapolated from data (solid line).

Unlike the trends found in the methane and E32 and E40 flames, after the SVF correction in the E60 and E80 flames, there is still a re-increase in fluorescent nanostructures downstream in the sooting region, indicating that at least some of the signal contributing to the second peak is genuine LIF. The resurgence of nanostructure LIF in the sooting regions of the E60 and E80 flames does not fit with the picture of particle formation supported by previous studies made in different operating conditions [116, 124, 235]. Considering the progress in the understanding of the chemical kinetics of the formation of nanostructures known to fluoresce, based purely on kinetic arguments it is difficult to see how the presence of the second peak of LIF in the E60 and E80 flames can be explained.

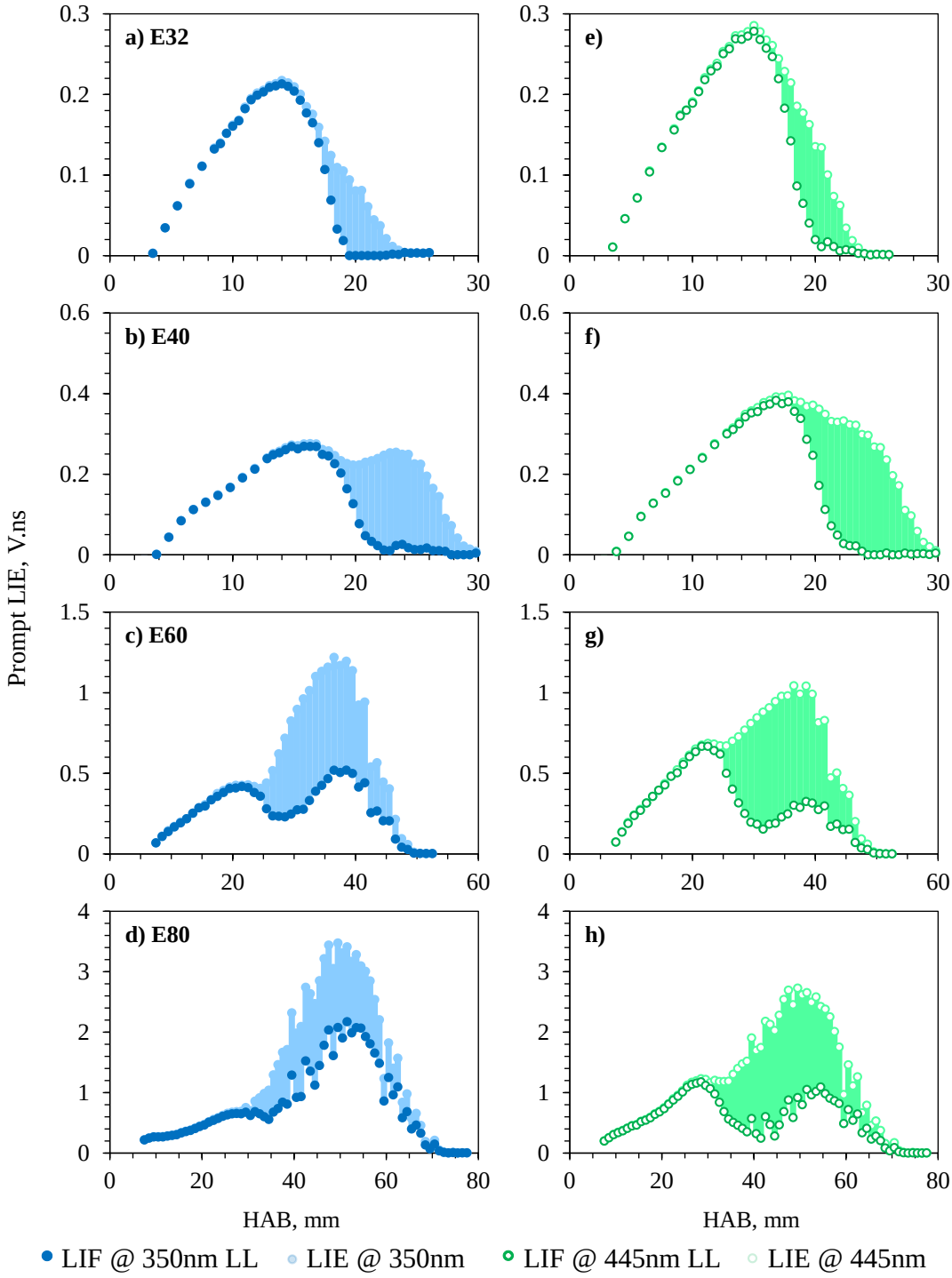

Figure 5.10: Lower limit (LL) of prompt LIF centreline measurements corrected for maximum linear interference from SVF for ethylene flames. Uncorrected LIE measurements and shaded area corrected as semi-transparent for comparison.

A possible explanation for the remaining second LIF peak in the sooting region of the E60 and E80 flames involves the structure of the diffusion flame itself, whereby at downstream locations closer to flame tip, particles from the centreline mix with particles produced in the outer regions or wings of the flame closer to the flame front. Figure 5.11 helps illustrate the specifics of the soot structure within these flames, from the planar SVF measurements of Smooke et al. [27]. Looking the E60 flame compared to the E32 flame it becomes obvious that a different structure emerges as where the peak soot formation occurring off the centreline. To further illustrate this possible transport of material from the wings, Figure 5.12 reports the radial profiles for the E32, E40 and E60 at three different HABs, namely at the peak centreline SVF (top), at the maximum soot formation rate i.e. on the maximum increase of the LII signal (middle) and before soot is detected (bottom). The LIF presented in these Figures have been corrected for the maximum interference proportional to SVF. These three heights can describe with sufficient precision the spatial evolution of particles within the flame.

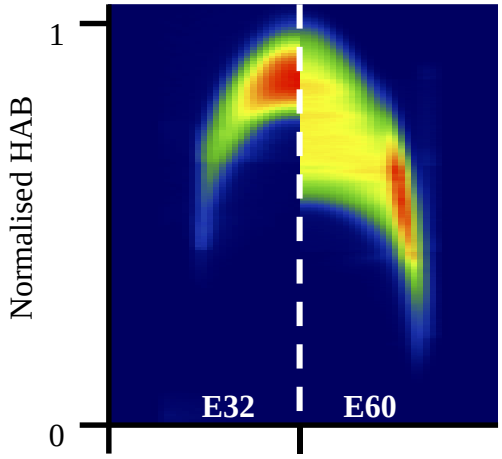

Figure 5.11: Structure of sooting region in height normalised E32 and E60 flames. Colour map presents zero (blue) to maximum SVF (red) [27] normalised for each flame.

For the radial traverses taken at the lowest height for all flames (lower panel in Figure 5.12) where no soot is detected on the centreline, it is possible to measure soot on the outer regions, as is evident from the presence of LII toward the edge. Also for the lowest height cases, the LIF signal in the E32 and E40 flames is a maximum on the centreline and decrease with radial distance, whereas in the E60 flame features a local maximum off the centreline in the wing region at the same radial location as the peak SVF. Moving downstream (middle and top panels of Figure 5.12), it is seen that in the E32 and E40 flames that the radial profiles of LIF decrease in a similar Gaussian-like decay at all axial

locations, whereas in the E60 flame the LIF wing peak is still prominent at all axial locations. Similarly, moving to the top panel of the E60 flame, the SVF is a maximum on the centreline whereas the 266 nm LIE shows a weak but detectable peak in the flame wing. The position of the LIF peak in the wing region of the E60 flame moves inward with increasing HAB, showing that the reaction zone moves closer to the centreline due to the closure of the flame tip. It can be considered that the material present on the tip of the flame to be a mixture of material originating from processes occurring from both along the centreline and from the wings of the flame. The presence of strong fluorescence quenching species such as oxygen is to be expected both in the wings as well as near the tip of the flame and would lead to an underestimation of the LIF peak in the wings and tip of the flame.

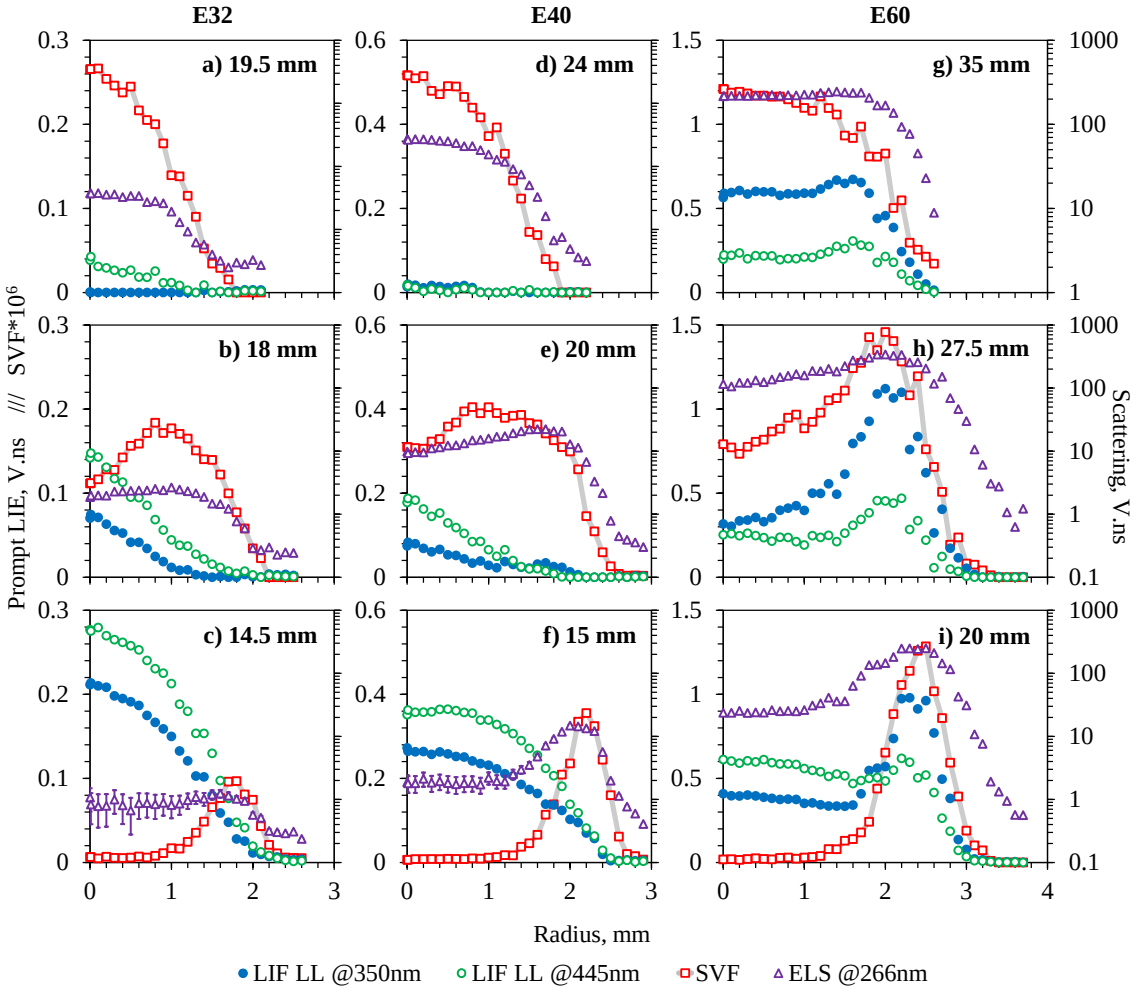

Figure 5.12: Prompt LIE and SVF measurements at various HAB against radial position in E32 (a, b and c), E40 (d, e and e) and E60 (g, h and i) and flames. LIF measurements presented have been corrected for maximum linear interference from SVF.

The longer lengths of both the E60 and E80 flames enables much larger soot concentrations to be formed in the wings of the flames due to longer residence times at high temperatures. These features could explain, at least in part, the second peak in the 266 nm LIE signal at the flame tip: the small nanostructures produced on the outer zone are convected toward the flame tip and merge with those coming from the pyrolytic zone along on the centreline. The observed shift in the importance of particle production and transport from the wings for the high sooting flames agrees with previous results by Smooke et al. [27] and shown in Figure 5.11, that show that the low sooting ethylene flames (E32 and E40) feature a much stronger particle formation on the centreline compared to the higher sooting ethylene E60 and E80 flames where particle production was found to be much higher in the wings. It is worth noting that the formation processes along the centreline compared with that on the wings are very different. The wings of the flame can, in some way, be compared with counter-flow diffusion flames where the mixing of fuel and oxidiser are dominated by diffusion. However, in this coflow diffusion flame, the combustion formed particles in the wings of the flame are convected downstream towards higher HAB experiencing a long residence time in a highly reactive fuel-rich environment. A comparison with similar measurements in a counter-flow flame [51] shows some similarity in the shifting of the spectrum moving towards the oxidiser side. Nanostructures found on the oxidiser side tend to have a blue-shifted spectrum akin to that found in rich premixed conditions [97], where polymerisation of aromatic units into oligomers is favoured. Overall, the measurements and picture formed from the high aspect ratio sooting laminar diffusion flames reported in this Chapter will help in the understanding of the particle formation pathways and pose a challenge to modellers to successfully predict the origin and evolution of the nanoparticles in these flames.

5.3 Conclusion

The time-resolved LIE technique was extended to diffusion flames in this Chapter. LIF contribution primarily from aromatic nanostructures was determined in upstream regions of methane and ethylene coflow diffusion flames. The non-sooting M65 flame shows no significant nanostructure evolution before LIF emissions reduce at the oxidative flame tip. However, structural transitions facilitate soot formation even in the marginally sooting M80 flame, where the LIF emission shifts towards a red-shifted spectrum suggesting an increase in the aromatic and stacked nature of the nanostructures. A red-shifted spectrum with increasing HAB is also present in the sooting ethylene flames and coincides with a strong increase in ELS. In the upstream regions of the flames, an appreciable scattering signal above the gas phase levels with no measurable SVF, highlighting that the mean

nanostructure size must also be increasing with the residence time in the pyrolytic flame region. A reduction in the quantum yield results in the decrease in LIF intensities approaching the soot formation region in these flames as nanostructures become more graphitic and tend to incandesce instead of fluorescing. The nanostructures are known to still be present in this “dark region” as ELS measurements continue to increase before the steep increase of SVF. Higher nanostructure concentration is found to proceed the higher SVF found in fuel rich high-sooting flames, although not proportionally, suggesting surface growth strongly contributes to increasing SVF moving downstream.

LIF measurements become challenging in sooting regions of the flames examined, and interference from LII and other soot derived emissions were found. A linear interference trend with SVF was observed, and corrections for the soot based interferences were made to the “prompt” LIF signal. The lower sooting flames (M80, E32 and E40) show LIF signals decreasing to negligible values within the sooting downstream regions well before oxidation at the tip. The longer, higher sooting flames (E60 and E80) showed a peculiar re-increase in the LIF signal along the centreline in the downstream sooting zone. The presence of LIF from nanostructures in the sooting zone is believed to be genuine and a consequence of the high aspect ratio of these diffusion flames allowing particle formation in the outer regions, or wings, of these flames to be transported downstream to the centreline at the flame tip. The particle formation in the outer regions of the flames was identified by a wing structure found in both LIF and LII, where the presence of oxygen and higher temperatures facilitate a different soot formation pathway similar to counter-flow diffusion flames. In the outer regions of the flames less aromatic (blue-shifted spectrum) nanostructures co-exist with larger soot particles and are convected downstream, merging with the centreline. These high aspect ratio diffusion flames pose interesting and challenging features that highlight parallel soot formation pathways.

Chapter 6: Laminar Partially Premixed and Diluted Flames

While a number of interlinked factors including pressure, temperature and fuel chemistry play significant roles in the formation of soot and nanostructures, the effect of partial premixing is particularly relevant in real combustion devices and emissions [14, 20]. Small amounts of partial premixing with air in ethylene flames is known to slightly increase soot volume fraction (SVF), precursor particles as well as aromatics such as benzene and naphthalene [191, 235, 236]. Mass spectrometry measurements have shown that the addition of oxygen enhances the formation of intermediate C3 hydrocarbons which are known precursors of benzene, whilst also increasing the formation of oxygenated hydrocarbons [235, 237]. However, the concentration of other hydrocarbons in these flames decreases, primarily due to reduced fuel concentration [238], while oxygen addition increases the rate of soot formation [236, 239]. Competing effects of increased reaction rate and reduced fuel concentration need to be considered in determining the evolution of soot in partially premixed flames. This purpose of this Chapter to address this distinction. A combination of temperature measurements, and time-resolved LIE are used to investigate the growth of soot and soot nanostructures within a set of partially premixed and a set of N_2 diluted coflow diffusion flames.

6.1 Experimental Setup

6.1.1 Flame Conditions

The burner used in this study is the same laminar coflow burner in Chapter 5 and detailed in Section 3.3.1. The model flame chosen for this study was the 60% ethylene, 40% nitrogen by volume flame (E60, as in Chapter 5), a target for the ISF [200] (ISF-3 Coflow 3) which has already been explored in previous publications [27, 213, 233]. This flame was used as the base to investigate the effects of premixing and dilution on the formation of soot and nanostructures. A set of partially premixed flames was created by adding air to the jet whilst keeping the flowrate of fuel constant. Equivalence ratios (ϕ defined on the base of the fuel jet stream composition) from 24 to 3 were investigated. It is important to note that the addition of air increases the jet bulk velocity (U_{bulk}) and reduces the fuel concentration, as the fuel flowrate is kept constant between these flames. For this reason, a complementary set of flames was also investigated to identify the effects of dilution, where additional nitrogen was added instead of air for each of the premixed cases. All the diluted cases have $\phi = \infty$, however, share the same fuel dilution and U_{bulk} with the equivalent premixed case. Flame details are reported in Table 6.1 together with acronyms used in the text to easily identify them: partially-premixed flames are labelled PP24 through PP3 and nitrogen diluted flames are labelled DN24 through DN3. Time-resolved, pointwise LIE measurements and thermocouple temperature measurements are conducted along the centreline of these flames. Photographs of the flames can be found in Figure 6.1, while flame heights can be found in Table 6.1. Some additional flames (E32, E40 and E80) from the list of ISF target flames [200] are comparatively discussed later and are detailed in Table 5.1.

Table 6.1: Partially Premixed (PP) and Diluted (DN) flame details.

Set	Flame	ϕ	Jet U_{bulk}, cm/s	Flame length, mm	C_2H_4 flowrate (jet), SLPM	N_2 flowrate (jet), SLPM*	Air flowrate (jet), SLPM
Base	***E60***	∞	35	50	0.158	0.106	0.000
PP	***PP24***	24	48	49	0.158	0.106	0.094
	PP18	18	52	48	0.158	0.106	0.126
	PP12	12	60	46	0.158	0.106	0.188
	PP6	6	85	41	0.158	0.106	0.377
	PP4	4	110	36	0.158	0.106	0.565
	PP3	3	135	33	0.158	0.106	0.754
DN	***DN24***	∞	48	50	0.158	0.200	-
	DN18	∞	52	51	0.158	0.232	-
	DN12	∞	60	51	0.158	0.294	-
	DN6	∞	85	54	0.158	0.483	-
	DN4	∞	110	62	0.158	0.671	-

All air coflow **velocities are 35 cm/s.**

*For PP cases N_2 flowrate is in addition to the nitrogen present within jet air flowrate.

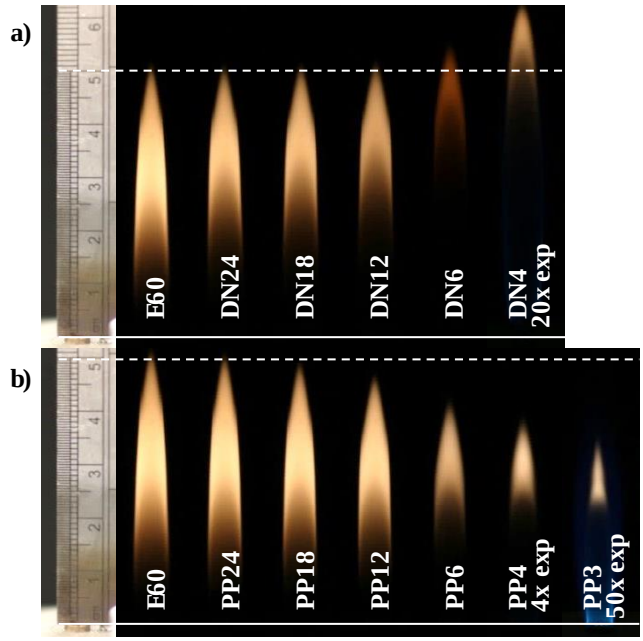

Figure 6.1: Photographs of a) DN and b) PP cases. All photographs were taken at same $f_{\#}$ and exposure except for those labelled with extended exposure. Scale in cm.

6.1.2 Time-Resolved LIE

The setup for the LIE measurements are identical to that for diffusion flames in Chapter 5. However, due to the limited knowledge of the temperature close to the jet, the same ethylene fragmentation corrections made in Chapter 5 could not be made here. Upstream areas of the flames that possessed some fragmentation interference are omitted for clarity. Similarly, the downstream LIF measurements containing interference from soot are omitted, as downstream LIF was not a focus of this particular study.

6.2 Results and Discussion

The flame lengths of the DN cases, shown in Figure 6.1a, do not change between E60 and DN12. Flame DN6 begins to detach from the burner, while DN4 is a lifted flame. Flame DN3 was not possible to stabilise as it was beyond blow-off. The location of soot formation in the DN flames moves downstream with increasing dilution as indicated by the luminous regions of in the photographs. In the PP cases, Figure 6.1b shows that the flame height decreases with increasing premixing, and the location of soot remains relatively constant,

just above 25 mm along the centreline, similar to the features reported by De Falco et al. [191] and McEnally et al. [235]. In both the PP and DN cases, the length of the sooting region decreases with reduced fuel concentration and hence increasing jet velocity. At around the same fuel concentration level in flames PP6 and DN6, the flame structure changes, where there is a significant reduction in the luminosity of the outer annulus of the flame, indicating a significant drop in the soot production on the wings.

Centreline thermocouple temperature measurements, performed with an uncoated R-thermocouple with a bead size of 225 µm, are presented in Figure 6.2 for the PP and DN cases. The rapid insertion technique was used here, is the same as that presented in Chapter 4, and corrections for radiation and soot covering the bead were applied following a procedure developed by Commodo et al. [191]. These measurements, as in Chapter 4, were conducted at the Università degli Studi di Napoli Federico II by Mariano Sirignano. The PP cases in Figure 6.2b) show a general trend of increasing temperature with increased premixing is noted downstream of 16 mm, despite the reduced fuel concentration in the flames with greater degrees of partial premixing. The results show similarities to previous measurements performed in larger diameter partially premixed coflow diffusion flames [191, 235]. These past measurements have normalised centreline trends on the height of the maximum temperature (H_T), however, this has not been done in the current work as it complicates some of the trends presented later. The DN cases in Figure 6.2a) show a general trend of decreasing temperature exist with increasing dilution for all height above burner (HAB).

It is noted that premixing in the manner presented here, there is a trade-off that the temperatures present between flames will not be constant. Whilst this does make it difficult to separate the specific effect of O_2 from that of temperature, one could argue that in practical combustion environments, these go hand in hand and increasing temperature is itself a consequence of increased reactions due to the oxygen. Some studies aimed at isolating effects of dilution and temperature, by dilution with H_2 [240] or preheating reactants prior to burner outlet [241, 242] have shown that temperature, dilution and oxygen content have some independent impacts on foot formation. Reduction of soot production due to dilution was found to be due to both the lowered temperature and reduced fuel concentration [240, 241]. Addition of oxygen, on the other hand, appears more complex and dependant on fuel chemistry. The study by Gülder [242] indicates that the presence of oxygen aids soot formation in propane and n-butane, but it supresses soot formation in methane. However, separating all these effects was not possible with the current flame set and thus the effect of temperature has not been separated from premixing in this discussion. The potential for future studies into the separate effects of temperature,

dilution and oxygen are important. Even so, the selected flames were favourable due to their similar characteristic flame lengths.

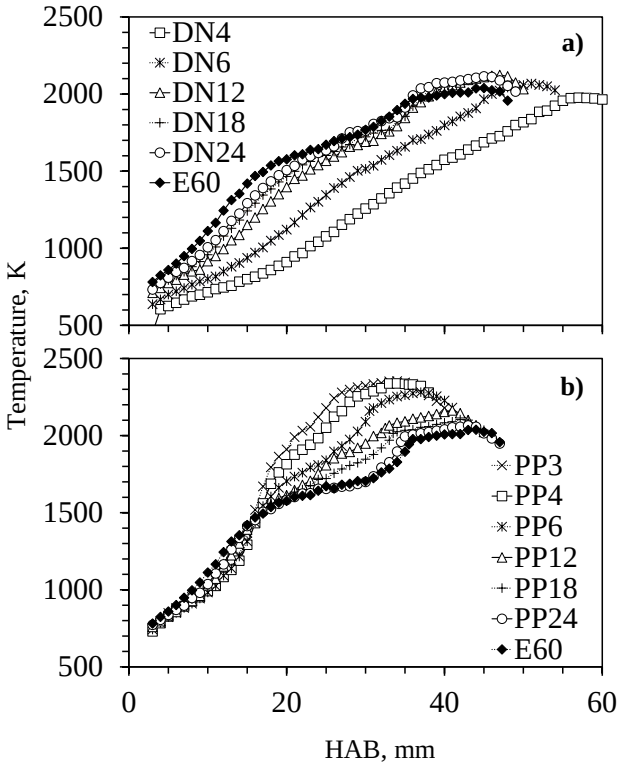

Figure 6.2: Centreline temperatures for the a) DN and b) PP flames.

Measurements of the centreline LIF @ 350 nm for both the DN and PP cases are reported in Figure 6.3. For the same reasons presented in Chapter 5, the "prompt" integrated (0 – 10 ns) signals are presented here. Interferences in the LIF signal from LII in the presence of soot at greater than ~100 ppb and photofragmentation of ethylene at HAB < 15 mm complicates the interpretation of the LIF signal. Details of the possible corrections made are also given in Chapter 5, however, corrections due to photofragmentation are not made due to the uncertainty in the temperature measurements close to the burner exit plane. Conduction along the thermocouple wires is the likely cause of high temperatures (> 600 K) measured at HAB = 3 for all PP and DN flames, when these temperatures are expected to be closer to the temperature of the incoming fuel mixture (300 K). At locations where the temperature was measured to be less than 1400 K, some ethylene is expected and thus these LIF measurements are not reported. Similarly, to the diffusion cases presented in Chapter 5, a correction to the downstream LIF measurements can be made to remove the LII component. However, downstream measurements containing LII and potential LIF

originating from the converging of the wings was also removed in this data as this study is focused on the centreline formation of nanostructures and soot.

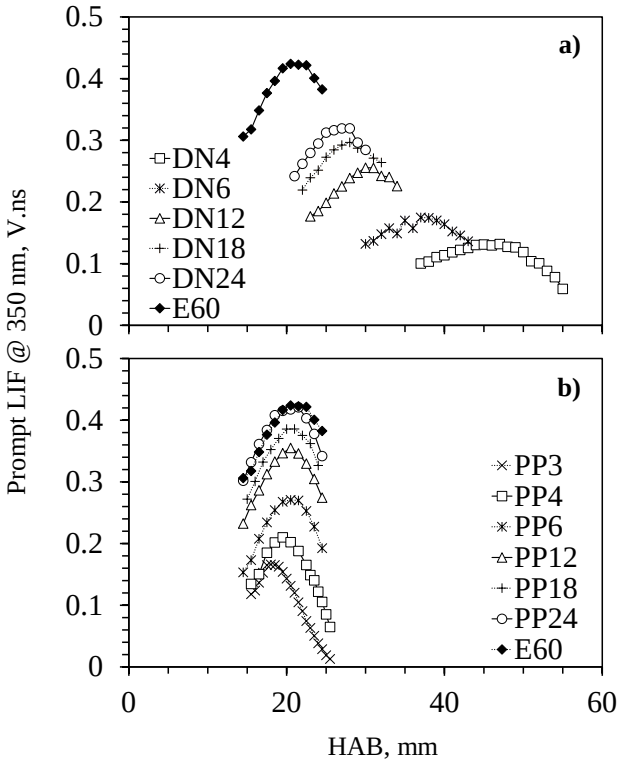

Figure 6.3: Prompt LIF @ 350 nm centreline profiles for a) DN and b) PP cases.

The LIF decay times for the DN and PP flames in regions not affected by ethylene photofragmentation or soot interference are presented in Figures 6.4a and d. The decay times are determined using the simpler peak normalised integral method also used in Chapter 5 and described in Section 3.2.1. In all flames, the effective time decay for both DN and PP cases are longer than 3 ns at HAB = 15 mm and increases moving downstream into regions of higher temperature. The increase in decay time with HAB is in stark contrast to the behaviour of gas phase PAH that show rapidly decreasing fluorescence lifetimes with increasing temperature [117]. The decay times presented are also above any measured gas phase PAH decay times at the measured flame temperatures. The long LIF decay times indicate that the majority of LIF originates from larger nanostructures with aromatic moieties and molecular like electronic energy levels similar to those measured in premixed flames (Chapter 4). It would be reasonable to assume that these nanostructures are somewhere between the sizes of the gas phase PAH and the smallest soot particles, namely

between 1 nm and 10 nm in diameter, as previously observed in both diffusion [122, 184] and premixed flames [98].

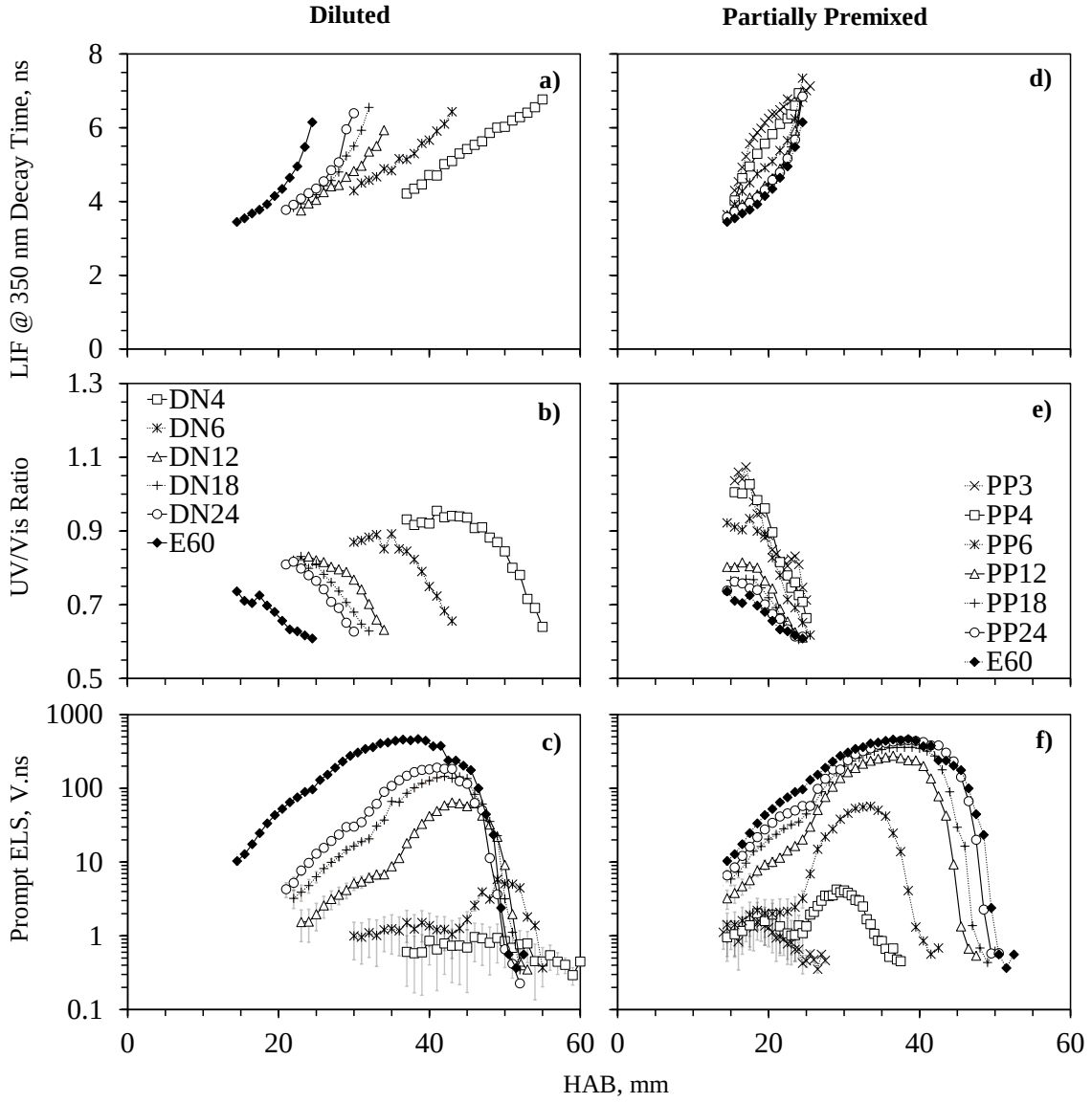

Figure 6.4: Exponential decay times for LIF @ 350nm vs HAB for a) DN and d) PP cases. b) and e) show corresponding UV/Vis LIF ratios (350nm/445nm). c) and f) show corresponding ELS intensities.

The presence of long-lived LIF coincides with significant amounts of ELS as seen in Figures 6.4c and f, particularly in the higher sooting flames. An error band is placed on the ESL measurements to indicate the potential interference of deep UV LIF in the ELS

measurement as discussed in Section 3.1.6. In the higher sooting flames (PP12 to PP24 and DN12 to E60), the scattering signal detected in the upstream region before the onset of soot is well in excess of that expected from gas phase given flame temperatures. The change in rate of increase of ELS ($d^2ELS/dHAB^2$) in this region also exceeds that of LIF ($d^2LIF/dHAB^2$), suggesting that average particle size is increasing moving downstream.

The evolution of the fluorescence emission spectrum of the nanostructures with HAB can be broadly monitored by considering the ratio between LIF @ 350 nm (UV) and LIF @ 445 nm (Vis), which is presented in Figure 6.4b and e DN and PP cases respectively. All flames show a transition from a higher UV/Vis ratio to a lower ratio of around 0.6, which corresponds to a redshift in the spectrum. A shift towards longer wavelengths could indicate an increase in the size of the dominant aromatic island responsible for LIF, similar to that concluded by Hayashida et al. [124]. Alternatively, it could indicate that an evolution of nanoparticles to a more graphitic structure which would also exhibit longer lived LIF [51]. It is also noted that higher levels of premixing (PP3 and PP4) initially at low HAB show a very blue-shifted spectrum, highlighting the impact of small amounts of oxygen in an otherwise pyrolytic environment. It would seem that newly incepted nanostructures formed in the presence of oxygen consist of smaller PAH units exhibiting blue-shifted fluorescence emissions [26, 115, 185]. The pyrolytic zone of laminar diffusion flames initially exhibit a red-shifted spectrum in comparison to rich premixed flames [21, 51, 124]. A shift from an initially red-shifted spectrum to a blue-shifted spectrum is observed with increasing partial premixing and provides a link from the nanostructures formed in diffusion flames and rich premixed flames.

LII measurements, converted to a SVF in the same manner given in Chapter 5, are presented in Figure 6.5a and b for both the DN and PP cases respectively. The base flame, E60, shows that soot production emerges at HAB = 25 mm and the volume fraction increases rapidly until around 30 mm. The SVF plateaus at around $1.25x10^{-6}$ before the oxidation rate becomes larger than the growth rate after HAB = 40 mm, reducing the SVF towards the flame tip. Prior to the onset of soot, LIF from nanostructures prevails, as seen in Figure 6.3. LIF intensity, hence nanostructure concentration initially increases and peaks at HAB = 20 mm, after which it begins to decrease again before the onset of soot at 25 mm. The decrease in LIF after the peak should not be entirely attributed to a reduction in particle concentration or size, but a significant contribution can be associated to a transition of the nanostructures towards more graphitic assembly as particles likely exhibit lower fluorescence quantum yield causing particles to incandesce instead of fluoresce. This general growth process is well accepted [15, 28, 30] and present in all the flames.

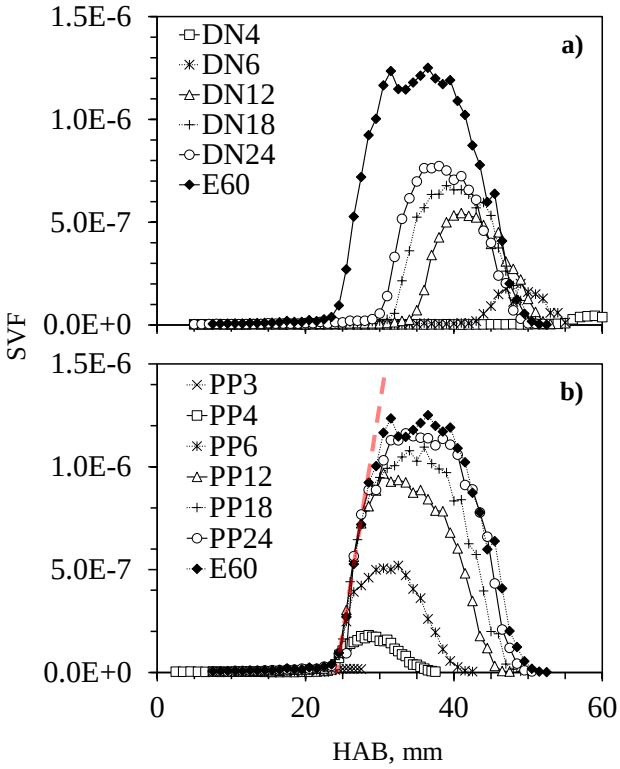

Figure 6.5: Centreline SVF from LII in a) DN and b) PP cases. Red (dashed) line highlights maximum soot growth.

Figure 6.5a shows that increasing dilution results in a reduction in the peak centreline SVF and a downstream shift in the location of soot emergence. A similar observation can also be made for the preceding nanostructure concentration in Figure 6.3a, where LIF intensity decreases with higher dilution levels and also shifts downstream to larger HAB. The PP cases, on the other hand, do not show this downstream shift for either LIF (Figure 6.3b) or soot (Figure 6.5b). The peak centreline SVF present in the PP cases also shows a decrease with increased premixing, however, not as large or as rapid as the equivalent DN cases. Previous studies in partially premixed flames have reported a slight increase in SVF with small amounts of premixing [191, 235, 236]. Although this is not observed in the current study, there is not a significant decrease in SVF from E60 to PP12. It is evident that partial premixing with air results in higher SVF, as well as higher LIF signals, compared with dilution, which is consistent with the results of McEnally et al. [237, 238]. The reasons for increased precursor formation that in turn leads to increased soot formation seems to be an enhancement of specific radicals promoted by oxygen, that then leads to the formation of benzene and other aromatics. The occurrence of the propargyl radical (C_3H_3), is likely

enhanced with the presence of oxygen, much like other C_3X species, allowing the self-reaction and formation of benzene [235, 243].

Irrespective of the level of premixing, Figure 6.5b shows that all the PP cases share HAB = 25 mm as the location for soot emergence. Due to the range of U_{bulk} between E60 and PP3, the residence time at HAB = 25 mm will not be consistent between flames, and will, in fact, represent shorter residence times for increasing levels of premixing. A similar statement regarding the reduced residence time with increased premixing can be made for the nanostructure formation reported in Figure 6.3b. Not only is the location of soot formation consistent with all the PP cases, but also the spatial rate of soot growth (*dSVF/dHAB*), marked as a dashed line in Figure 6.5b is similar between all cases. Much like HAB and residence time, *dSVF/dHAB* does not correspond to a consistent *dt* value for all flames and thus the highlights that the rate of soot growth (*dSVF/dt*) increases dramatically with premixing. The enhanced growth process of soot has been previously noted [236] and is also found in the LIF UV/Vis ratio presented in Figure 6.4e. The transition from a blue-shifted spectrum (higher ratio value) to a red-shifted spectrum (lower ratio value) along HAB must also happen in a shorter time frame at higher levels of premixing. A combination of UV/Vis ratio and LIF decay time yields insight into the transition of fluorescent nanostructures from simpler aromatic structures to those with larger aromatic islands and featuring a more stacked and rigid arrangement due to Van der Waals interactions between poly-aromatic planes. All flames (PP and DN) exhibit a transition towards a UV/Vis ratio of around 0.6 and a decay time stretching towards 7 ns just prior to the onset of soot. Although the LIF spectrum and decay time are impacted by temperature and concentration of quenching species [51, 117, 136], this common behaviour of PP and DN cases indicates that an average common precursor structure is arrived at, regardless of the flame conditions, just prior to the onset of soot.

The increase in nanostructure and soot formation rate in the partially premixed flames raises the following question: what is the particle flux in these flames? In the current study, no increase in LIF or SVF with premixing level was observed. However, the increase in flame velocity means there is a higher turnover of these particles. Without knowledge of the flow field in these flames, a detailed assessment cannot be made, but underlying trends can be extracted subject to a few assumptions. Mass or volume flux measurements generally involve analysing an entire planar slice perpendicular to the flow. However, since pointwise measurements are obtained, the peak location of SVF and LIF will be used as representative samples for each flame. To calculate the true flux, and in the absence of flow field measurements, the assumption is made here that the local velocity at the same HAB in each flame is proportional to U_{bulk} with considerations for the expansion of gases due to temperature. For PP the cases a similar HAB exists for both peak LIF (HAB = 20 mm) and

SVF (HAB ≈ 30 mm). The scaled volume flux of soot (SVfx ∝ SVF×$U_{bulkTad}$) and nanostructures (NVfx ∝ LIF×$U_{bulkTad}$) are obtained using $U_{bulkTad}$ as representative velocities, under the previous assumptions, and are presented in Figure 6.6. $U_{bulkTad}$ is defined as the bulk velocity increased due to temperature driven gas expansion for each PP flame given the temperatures presented in Figure 6.2b. The author acknowledges that the assumptions made here are somewhat crude, but believes the underlying trends presented remain valid[†]. The same assumptions, however, cannot be justified for the DN cases due the large range of HAB where soot initiates and therefore flux analysis of the DN cases are not presented. A more robust estimate of SVfx and NVfx was calculated for the ISF target flames used in Chapter 5 (E32, E40, E60 and E80), using the simulated residence time presented by Smooke et al. [27] and then normalised to be plotted alongside the PP cases in Figure 6.6. Normalised SVfx and NVfx are plotted against fuel % in the jet allowing a comparison of dilution effects on particle production. For the ISF target flames, the U_{bulk} is kept constant while fuel concentration is varied. Figure 6.6a shows a nearly linear relationship of SVfx with fuel flowrate for the ISF flames. The PP cases, on the other hand, show a dramatically different trend with an increase in SVfx with small amounts of premixing (PP24 to PP12) compared to the E60 base case. Higher levels of premixing (PP6 to PP3) then show a decrease in soot flux. Even though local soot concentration decreases with premixing, due to reduced fuel concertation, the total production of soot in these flames with a small amount of premixing increases. Figure 6.6b presents the NVfx for the same flames. Similarities in the trends can be seen with near linear relationship of NVfx against fuel flowrate for the ISF cases. The PP cases show an increase in NVfx with increasing premixing up to around PP4. SVfx is decreasing at these levels of premixing, yet further oxygen addition continues to aid in the formation of nanostructures. When considering the effects of partial premixing on emissions, the results reported in this study highlight that the increasing importance of nanoparticles in government emission regulations [14] are well justified in placing a greater emphasis with the number density of emitted particles rather than mass. In other words, the flux of nanostructures is increasing in seemingly lower and lower sooting conditions. Hence, a decrease in SVF or SVfx does not indicate a decrease in the nanostructure formation. Furthermore, the additional oxygen in the premixed cases also increases the concentration of oxygenated hydrocarbons [235]. Such oxygenates are typically more toxic than other similar sized hydrocarbons.

[†] Subsequent to the submission of this thesis, computations were conducted by Università degli Studi di Napoli Federico II to compliment this analysis. This analysis does consider buoyancy in addition to gas expansion and has a minor impact on the calculation of soot and nanostructure flux. However, by and large the underlying trends remain as asserted and presented here. The addition of this further analysis could be made to the thesis, however, the author prefers the original discussion as the same conclusions are reached without the extended preface of computational results and additional layers of assumptions needed for this analysis. The author prefers the existing simpler presentation where assumptions are minimised, the analysis is easier to follow and its shortcomings are highlighted for the benefit of the reader.

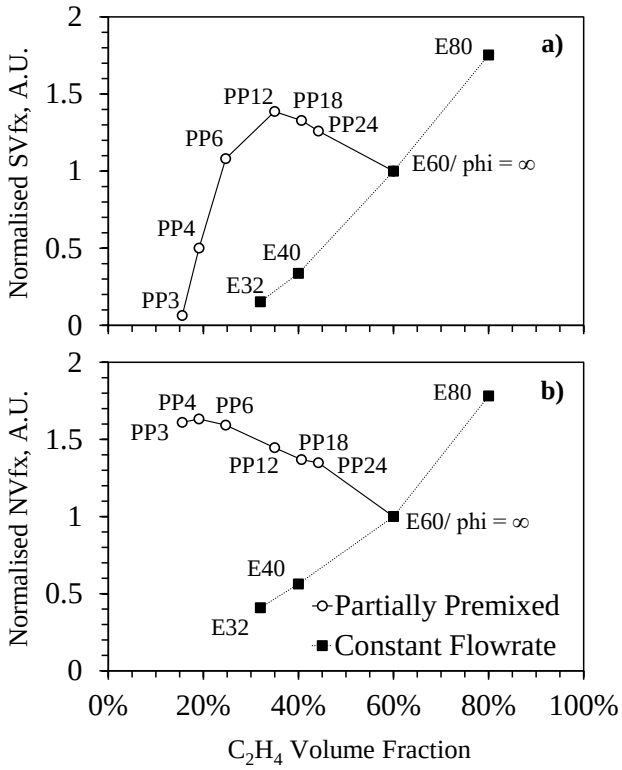

Figure 6.6: a) Normalised SVfx and b) Normalised NVfx vs. fuel % for Partially Premixed (PP) and constant flowrate ISF target (E) flames.

Similar to the results reported by reported by McEnally et al. [235], it is found in this work that the peak LIF signal in a flame provides a good indicator of peak SVF in the flame according to the trend presented in Figure 6.7a. A consistent relationship exists regardless of dilution, premixing or jet velocity, as DN, PP and ISF flames all fall on the same line. Soot formation requires a certain concentration of nanostructures and increases if nanostructure concentration increases. The impact of dilution (due to the addition of air) becomes evident in Figure 6.7b which presents SVfx vs. NVfx for the ISF and PP flames. The ISF cases present flames where the fuel concentration is varied in a different way to the DN or PP flames. For the ISF cases NVfx increases as fuel flowrate increases, while all flames maintain the same U_{bulk} by varying the nitrogen flowrate accordingly. Thus, NVfx is proportional to nanostructure concentration in the ISF cases, consequently, SVfx then follows NVfx. In the PP flames, the total jet flowrate increases with increasing premixing resulting in NVfx not being proportional to nanostructure concentration. Even though NVfx increases with increasing premixing, up till around PP4, the nanostructure

concentration decreases due to increase in total flowrate. Initially, between PP24 and PP12, small amounts of oxygen increase the radical pool and the reaction rate counteracting the effects of dilution. Further oxygen addition, from PP12 to PP3, has a limited return on the formation rate and the dilution of the nanostructures limits their coalescence into soot particles, thus reducing the total soot production while maintaining a similar nanostructure production. The physical processes that govern primary soot formation appear to be more affected by global dilution than the sometimes more chemical processes governing nanostructure formation. The effect of concentration on soot formation is already well established through investigations of flames at high pressure [244, 245], where higher concentration (due to pressure) results in a higher soot yield (amount of fuel carbon converted to soot). As a final remark, it seems that the NVfx cannot increase beyond a certain value which is determined by the amount of fuel and the level of premixing. Such a finding is relevant when considering the prediction and the control of condensed phase nanostructure in real combustion devices.

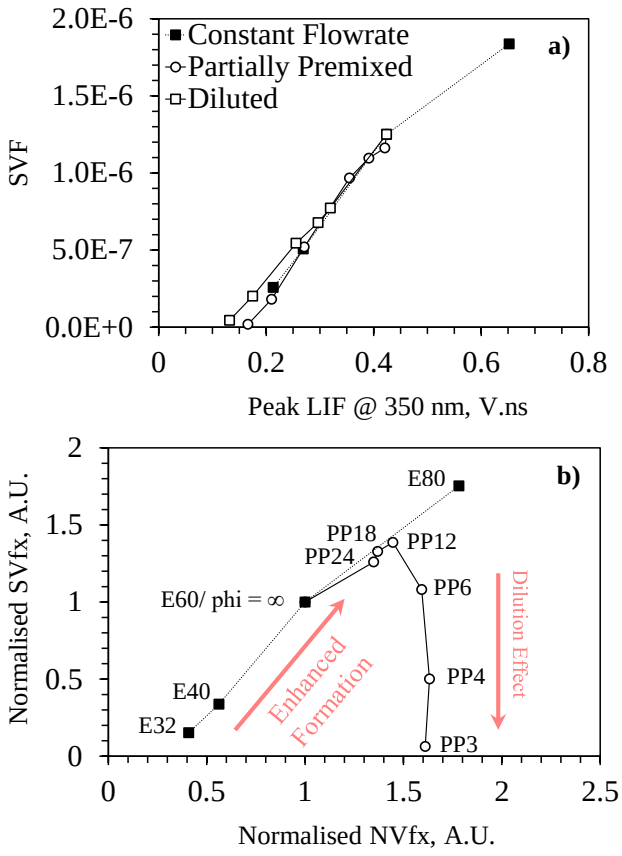

Figure 6.7: a) Peak SVF vs. Peak LIF @ 350 nm for constant flowrate (ISF targets), PP and DN cases. b) SVfx vs. NVfx for constant flowrate (E) and PP cases.

6.3 Conclusion

The effects of partial premixing and dilution on soot formation in coflowing diffusion flames were investigated through time-resolved LIF, LII, ELS and thermocouple measurements. Partial premixing was achieved by adding air to a jet of ethylene and nitrogen. Premixing in this manner increases the total flowrate, and partially premixed flames exhibit competing effects of enhanced reaction rate and dilution effects. For this reason, the partially premixed flames were compared with an equivalent non-premixed case, sharing the same level of dilution. Partial premixing showed enhanced nanostructure and soot formation over the equivalent diluted cases. However, both PP and DN cases showed a general decrease in volume fractions of both nanostructures and soot due to the impact of reduced fuel concentration. Even though all PP flames exhibited a lower SVF compared to the E60 base case, flames with low levels of premixing show an increase in total soot formation. This increase in SVfx is preceded by an increase in nanoparticle flux. NVfx continues to increase with additional premixing, highlighting that SVF or SVfx is not a good indicator of nanoparticle flux and vice versa. Nanoparticle flux enhancement due to premixing is a result of increased reaction rates whilst being less affected by global dilution. Soot flux, on the other hand, is greatly affected by global dilution, as the physical coalescence of nanostructures into primary soot is reduced due to lower nanostructure concentrations. This is a pertinent point for the practical combustion devices that operate in partial premixed conditions, with concerns about size and number of particle emissions, as small amounts of partial premixing noticeably increases the total particle flux. Irrespective of the increased reaction rate in the PP cases or dilution effect in the DN cases, nanostructures are found to proceed towards a common redshifted spectrum and longer decay times just prior to the onset of soot, indicative of evolution towards a more rigid stacked graphitic-like structure.

Chapter 7: Turbulent Diffusion Flames

The previous Chapters highlight the extensive literature available on laminar soot formation and its precursors. However, the same cannot be said for turbulent conditions. Whilst studies pertaining to SVF and size [55, 56, 58, 60, 61, 63, 218, 244] employing the use of LII, scattering and other techniques are valuable, the ability to probe soot simultaneously with other quantities gives further insight into how local flame conditions impact soot. Many studies have described the simultaneous interaction and dependence of soot with temperature [59, 246], velocity fields [247] and hydroxyl (OH) defined flame fronts [57, 62, 248]. However, studies on the nature and evolution of soot precursors remain scant [49, 99], and fewer still that use a simultaneous approach [248]. The study presented here aims to make a contribution in this space.

Soot exists in turbulent flows in the form of wrinkled soot layers that are distributed radially over the flame, in comparison to the oxidative OH flame front which often exists on the peripheral and does not penetrate towards the centre of the flame [57, 62, 218, 248]. The location of reaction zones and soot formation are consequently not constant in time and the intermittency of various species (and associated measurements) is very important in the description of turbulent combustion [55, 59, 249]. Studies in acoustically forced time varying laminar flames have relevance to turbulent combustion and provide insight into the interactions of unsteady flow fields with soot, PAH and OH layers [250, 251]. The flickering/oscillating flame shows that both instantaneous and time-averaged soot concentrations dramatically increase in these unsteady flow fields in comparison to their steady state counterparts. On the other hand, turbulent flames that experience high strain rates, due to high jet velocities/Reynolds numbers see a reduction in SVF [58, 247, 248].

Further study into turbulence effects of soot and its precursors, is needed and is a goal of the ISF workshop [200].

It is worth noting that although this turbulent flame study is presented last in this thesis, it was chronologically one of the first studies conducted, processed and published by the author [2]. Consequently, some of the methodology is not the same as in Chapters 5 and 6. The use of the "prompt" signal in Chapter 5 was valuable in discerning the contribution of LIF and LII to the total 266 nm LIE signal. Using the "prompt" signal here was not preferred over taking a longer integral as the "prompt" component is more susceptible to background fluctuations in the instantaneous signal. Additionally, the sooting propensity of the flame investigated was similar to that of the C/O = 0.77 premixed flame of Chapter 4 where the contribution of LII to the 266 nm LIE was determined to be marginal. The insights gained from this study required a different approach and focuses on the presence or absence of soot and nanoparticles in an intermittent turbulent flame. A simple piloted jet flame of Reynolds number Re = 10,000 and a mix of ethylene and nitrogen as the fuel provided a suitable sooting flame for this investigation. Investigating turbulent conditions is vitally important to describing what happens in many practical combustion technologies.

7.1 Experimental Setup

7.1.1 Flame Conditions

A turbulent piloted diffusion ethylene/nitrogen flame was stabilised using the turbulent jet burner described in Section 3.3.3 and consists of a 4 mm diameter jet surrounded by a pilot. The ethylene/nitrogen dilution was kept at 1/1 by volume, and the Reynolds number is 10,000. The ethylene/nitrogen mixture exited the jet at 25 °C before being ignited by the pilot. The visible length of the flame is about 0.6 m as seen in Figure 7.1 and it is blue in the first 100 mm or so near the pilot and visibly sooting further downstream. The pilot was a stoichiometric premixed hydrogen, acetylene and air mixture that matches the H/C ratio of ethylene and provides 5% of the total heat release. This flame was shielded with an air coflow velocity of 5 m/s, provided by a contracting square duct as described in Section 3.3.3. Further details are given in table 7.1. Time-resolved LIE measurements are conducted along the axis of the flame and radially at a few selected heights; HAB = 150, 245 and 340 mm. These three positions represent three distinct areas of interest, on the time-averaged flame: 150 mm, a quite bluish region of the flame before the onset of soot, 245 mm the onset of yellow luminosity containing soot growth, and 340 mm at the peak of yellow luminosity close to peak of the average SVF. These positions are indicated in Figure

7.1. The axial locations were explored up to a HAB = 370 mm. This height was limited by the usable range of the vertical traverse that the burner was mounted to, and thus locations further downstream were not probed. Previous measurements have also defined three nominal but distinct regions in sooting turbulent flames [62, 248]: 1, growth region defined by rapid soot growth and where the stoichiometric reaction zone remains outside and separate to location of soot and precursors. 2, mixing region where large wrinkling of the flame front occurs vortical structures stretch soot layers, and is possibly marked with a decrease in precursor presence. 3, is the oxidation dominated region where soot and OH fields overlap. The current measurements only concern the first two regions, at approximately 245 mm and 350 mm HAB respectively, due to the limitations of the vertical traverse. However, the fate of precursor particles is mostly confined to these first two regions.

Table 7.1: Turbulent flame details.

Jet	
Reynolds Number	10,000
C_2H_4 Flowrate, SLPM	11.01
N_2 Flowrate, SLPM	11.01
Pilot	
H_2 Flowrate, SLPM	0.489
C_2H_2 Flowrate, SLPM	0.489
Air Flowrate, SLPM	6.99
Wind tunnel air coflow velocity of 5 m/s	

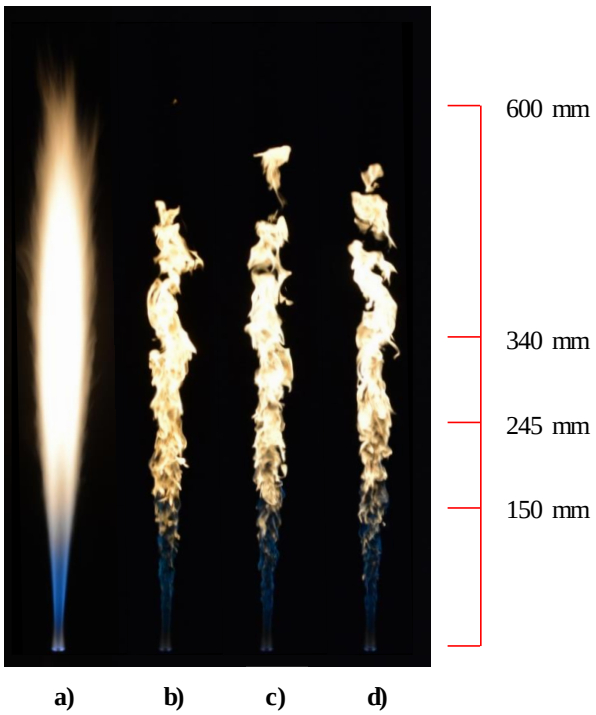

Figure 7.1: Photographs of Flame: 10,000 Reynolds number ethylene/nitrogen (1/1 by volume). 4 mm diameter Jet with 15 mm diameter pilot. Air coflow of 5 m/s. a) $f_{\#}$ = 29, exposure = 1 s. b), c) and d) $f_{\#}$ = 4.2, exposure = 1/4000 s.

7.1.2 Time-Resolved LIE

For the temporally resolved LIE technique to be valuable in the context of turbulent flames a key requirement is that it is capable of resolving individual instantaneous measurements. This means that for each laser pulse a sufficient amount of light needs to enter the spectrometer and reach the PMTs resulting in a signal that is easily distinguishable from the background noise of the system and environment. This is referred to here as the signal to signal to background (S/B) ratio as to distinguish it from signal to noise (S/N) ratio which generally refers to fluctuations inherent in the measurement system as opposed to the probe/environment. This condition is not crucial for the laminar flames explored in Chapters 4, 5 and 6 as these flames are steady in time and thus numerous individual signals are averaged to smooth out any shot to shot fluctuation. The same luxury is not possible in this turbulent flame and each individual signal needed to be resolved in terms of peak value, integrated value and time decay. At each location, 2500 instantaneous measurements were recorded to have a sufficiently large sample to characterise the flame statistically.

To maximise the light entering the spectrometer, the 266 nm Ekspla laser energy was increased to 1.2 mJ resulting in a fluence of 2.4 J/cm^2. The use of higher fluence for LIF measurements was shown in Chapter 4, Figure 4.5b, to have no impact on the time decay of the signal. However, this is only true where LII originating from the 266 nm laser is not present. In Chapter 5 it was conversely shown that in densely sooting regions that the total LIE signal (LIF and LII included) does not react uniformly with increased laser fluence. This being said, the relative contribution of LII to the total LIE signal can still be assessed by the determined decay time of individual signals. Because decay times do not dramatically begin to increase moving downstream into areas where incandescent soot in present, as seen later in the Chapter, indicating that LII contributes insignificantly to the total 266 nm LIE in this flame. Increasing the fluence of the 1064 nm pulse for the pure LII measurements is not practical as it would move it into a regime of excessive soot sublimation. Thus, the fluence of the 1064 nm pulse remained at 0.6 J/cm^2, as it is for all the other studies. To further increase the signal received by both laser pulses the slit width of the spectrometer was set to 100 µm. These differences in the experimental setup unfortunately make it difficult to compare specific values between this and other studies, however, the trends can be compared. Furthermore, to aid in mitigating the random aspect of noise and background fluctuation in the signals, the data presented here takes the entire integral rather than the "prompt" used in previous Chapters.

It is worth noting that when 1064 nm LII was detected on PMT4, a signal was also present in the PMT3 and PMT2. This is due to the blackbody radiation typical of LII signal which extends to the edge of UV-visible spectrum. A high level of background noise due to the fluctuating flame luminosity is present on PMT4, whose wavelength bin lies in the centre of the visible spectrum. Consequently, in these turbulent flame measurements, PMT3 was used to evaluate individual signals of 1064 nm LII, as they were less affected by background fluctuations. Regardless, the mean and conditioned mean trends, discussed further in Section 7.2, of PMT3 and PMT4 are qualitatively identical.

The separation between the 1064 nm pulse and the preceding 266 nm pulse was only 70 ns. Even in this much higher velocity flame, much larger delays could have been used and both probes could easily still be considered simultaneous (exiting the same packet of gas). A larger separation was not necessary as no significant long living LII was detected from the 266 nm emission. Additionally, this shorter separation time allowed for a more economical data processing as data contained less individual data points. An example of an instantaneous measurement that contains both obvious 266 nm LIF and 1064 nm LII is presented in Figure 7.2. It highlights the high S/N and S/B achieved by the setup and also the limited long living LII component present from the 266 nm pulse.

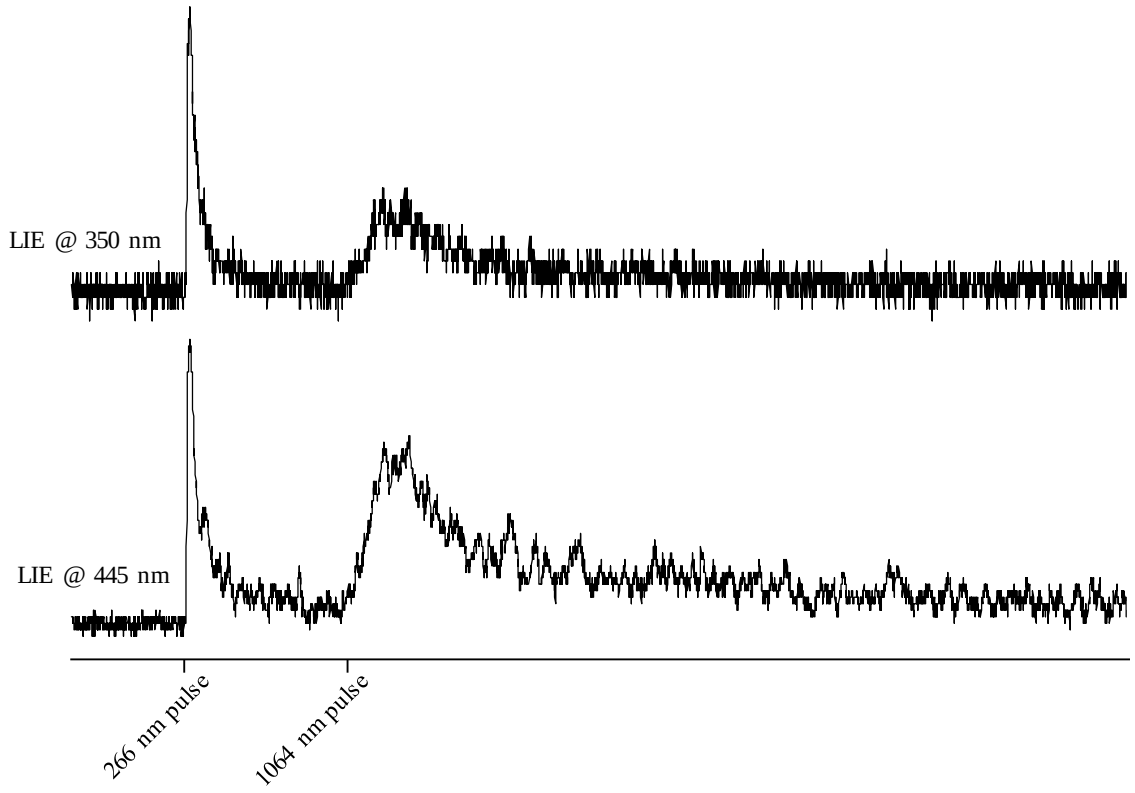

Figure 7.2: Instantaneous signal examples.

A potential issue in turbulent flames, particularly with a multi-laser technique, is that of beam steering [252]. This is the phenomena where changes in refactive index of the medium, generally due to local temperature gradients, that the laser passes will divert the laser off its original course. Due to the vertical orientation of the spectrometer slit, and the short distance over which the beam resides within the flame, the influence of beam steering is unlikely to be of concern for the measurements reported here.

In this study, LIF decay times were extracted using the simpler peak normalised integral method described in Section 3.2.1 and used in Chapters 5 and 6. This method is computationally far more economical than the direct multi-exponential curve fitting method, thus making it suitable for processing the comparatively large amount of data collected in this turbulent flame.

7.2 Results and Discussion

A key reason why looking at the unconditioned mean in turbulent flames can be misleading is due to impact of flame intermittency [55, 59, 249]. Due to the turbulent nature of the mixing that occurs downstream in turbulent flames, the unconditioned mean measurement of LIF, for example, will contain a number of near-zero instances as a result of measuring a pocket of unreacting air entrained from the outside. In this flame, downstream of 150 mm, flame intermittency becomes a relevant factor. High levels of intermittency corrupt the mean signal level when analysing processes of soot formation in turbulent flames and this is evident from the Probability Density Function (PDF) plots of the LII signal which show a very broad scatter. Figure 7.3a reports integrated LII signal at HAB = 340 mm on the centreline. The spike of values close to zero are due the intermittency of LII signals and can hardly be attributed to a genuine LII signal. In fact, measured values refer most likely to an inherent noise in the recorded signal. This noise is due to the collection electronics as well as background luminosity of the flame. To overcome this problem, data conditioning was applied as follows: Signals without a sufficiently high S/B ratio were removed as seen in Figure 7.3a resulting in a more monomodal distribution. S/B for each instance was defined as the temporal peak divided by the standard deviation of background fluctuation ($\sigma_{background}$) in the signal prior to the LIE as shown in Figure 3.1. In Figure 7.3b, the radial profiles of the unconditioned and conditioned mean signal for the LII at 340 mm are reported. The conditioned mean values are reported for different cut-offs in the S/B ratio. These cut-offs were defined as a multiple of the standard deviation of the signal noise, as seen in Equation 7.1. In this way the cut-off is adaptive to the local instantaneous background luminosity levels present that vary through the flame and shot to shot. A minimum cut-off level of five standard deviations was determined to adequately separate intermittent signals from genuine LIF or LII signals. A mathematically identical technique has been used similarly to look the active instances of the flame [248] where the population of "zero" (or intermittent) values define what is known as the "intermittency index" [253]. Mahmoud et.al [59] conditioned SVF measurements on instantaneous temperature, focusing on reacting or reacted instances, to very similar effect.

$$Peak_{\text{non-intermitent}} > cutoff \times \sigma_{background} \tag{7.1}$$

The different S/B ratio cut-offs chosen show that radial trend was insensitive to this cut-off although the absolute values are affected. A downwards trend moving to the edge of the flame can be seen in the unconditioned mean value. Data conditioning reveals the presence of a different trend, suggesting that soot formation is enhanced closer the edge of the flame. The decrease of the signal intensity seen in the unconditioned mean value is due

to the intermittency of the flame rather than a slowdown of in the instantaneous and local soot formation process as similarly observed by Qamar et al. [249] and the temperature conditioned profiles of Mahmoud et.al [59]. At outer radial locations (radius > 15 mm), the intermittency becomes so high that less than 10% of the collected data points remain after conditioning and hence results are not shown for these locations. While the conditioning applied in Figure 7.3 could be improved with additional measurements to provide sufficient statistics for more radial locations, the method applied here is adequate to show expected trends for LIF and LII in the locations measured in this flame. It is acknowledged that if measurements were possible in the far downstream regions of this flame, much more than 2500 shots per location would be necessary to properly resolve a conditioned mean.

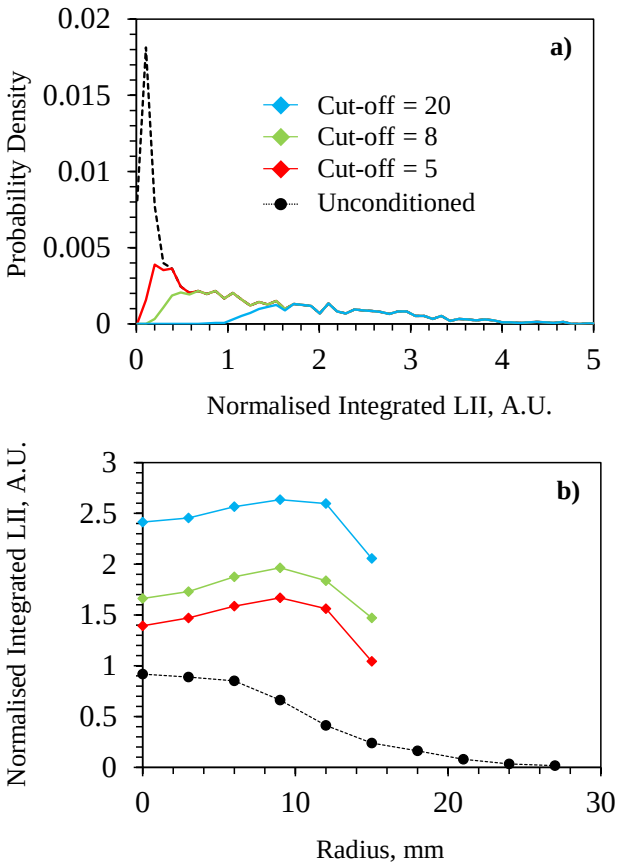

Figure 7.3: a) PDF of integrated LII signal at 340 mm on centreline with various cut-off levels and b) relative mean radial profiles derived from cut-offs.

Figure 7.4 shows the same conditioning applied to the LIF @ 350 nm at 150 mm HAB. Figure 7.4a presents the conditioned PDFs at different radial locations while Figure 7.4b plots the unconditioned and conditioned mean profile. Conditioning the data in this manner

draws focus to instances of the flame when soot or nanoparticles are present. LIF @ 350 nm has a defined monomodal distribution, exhibiting the influence of the intermittency just at the edge of the flame. In Figure 7.4c conditioned LIF @ 350 nm signals measured on the centreline at HAB = 340 mm show that this conditioning maintains only signals that have decay times above 2 ns as seen in Figure 7.4c. The presence of time decays between 1 and 2 ns can be related to the presence of quenching species or to the detection of some species having shorter fluorescence lifetimes. Whilst it might be possible to detect some shorter-living LIF signals, these signals do not make the S/B cut-off and thus by definition are not strong enough to further evaluate.

Figure 7.5 reports both the conditioned and unconditioned mean axial profiles of the laser-induced emission signals. Signals at lower HAB were detected but contained interference from ethylene photofragmentation from the 266 nm laser pulse. Because the laser fluence used in this study is much higher than that used in the studies of Chapters 4, 5 and 6, photofragmentation of ethylene is more significant here. Fragmentation signals are initially high closer to the burner jet exit but decline rapidly approaching 100 mm HAB and it is possible to say that photofragmentation becomes negligible after 125 mm. Measurements below this are presented in grey to highlight the photofragmentation issue while the remaining axial profiles provide an overview of the soot formation through the flame. Note that all data presented in this Chapter is normalised on the peak unconditioned centreline mean values as seen in Figure 7.5.

ELS has been conditioned slightly differently as, scattering is attributable to gas phase species through to solid soot particles and thus it is difficult to discriminate against a specifically gas phase, nanostructure or soot. As ELS tends to favour larger particles due to its d^6 relationship, the LII measurements were used to condition the scattering, meaning that conditioned ELS here is representative of soot scattering. Both ELS and LII track well the larger soot particles. Discernible levels of soot, based off the unconditioned mean, begins above 200 mm HAB on the centreline. The conditioned mean, on the other hand, shows that there are some pockets of soot do, albeit very rarely, occur as low as 175 and 200 mm HAB. Figure 7.6 shows the spread of intermittency as defined by LII (a) and LIF (b) interpolated from the axial and radial data. The intermittency factor is defined as the number of non-intermittent instances over the total number of shots taken. Although LII shows high level of intermittency in upstream regions, this instantaneous sparseness of soot is not due to large eddies or wrinkling of the flame entraining pockets of air, but rather shows that the majority of instances have not had sufficient residence time to form soot. For both soot and nanostructures intermittency increases radially but each show different trends moving downstream. LIF intermittency increases with increasing HABs because of air entrainment in the mixing region and possibly due to instances of reduced fluorescence

quantum yield of nanostructures as they coagulate into primary soot particles. LII intermittency initially increases moving downstream due to the increasing formation of solid soot particles, however, begins to decrease again as the competing effects of air entrainment and soot burnout increase downstream and resembles that observed in previous studies [55, 249].

The unconditioned axial mean LII in Figure 7.5 suggest that at the highest HAB measured, the mean soot concentration is approaching its maximum. However, the conditioned LII indicates that the local soot growth is continuing. Additionally, throughout the preceding soot growth region from 200 to 370 mm HAB, the presence of LIF has persisted. Conditioned LIF @ 350 nm shows an initial rise before plateauing around 225 mm HAB. Conditioned LIF @ 445 nm, on the other hand, continues to increase until 350 mm HAB. Both LIF @ 350 nm and 445 nm begin to show departure of the conditioned mean from the unconditioned mean at 250 mm HAB. These trends show that nanostructures are consistently formed along the centreline, with some interference from wrinkling of the flame in this mixing region, similar to that observed by Lee et al. [248] and Franzelli et al. [62]. This wrinkling can be observed in Figure 7.1 above 250 mm HAB in the short exposure photographs. The slight increase, or at the worst plateauing, of the conditioned LIF above 250 mm HAB indicates that nanostructures are continually being produced throughout the measured regions of the flame, despite the soot growth. Parallel to this, the evolution of the average nanoparticle towards a structure with larger aromatic constituents can be seen in Figure 7.7 via the red spectral shift with decreasing UV/Vis ratio and the minor increase in LIF decay times moving downstream. The increase in decay time, in some instances may be due to a minor presence of LII in the 266 nm LIE signal. The shift in decay time is not as pronounced as it is the laminar diffusion flame cases, Chapters 5 and 6, and appears to be more akin to the rich premixed flames seen in Chapter 4, where little change in decay time was observed both in sooting and non- sooting conditions. However, a direct comparison here is challenging as the instantaneous or averaged temperature is not known. It is worth noting that the UV/Vis ratio presented in Figure 7.7 is produced using the values for entire integral, and not “prompt” signal as in Chapters 5 and 6. Consequently, the severity of the redshift is exaggerated by the fact that the LIF @ 445 nm has a more obvious increase LIF decay time. Consequently, it would appear, that compared to laminar diffusion flames, the inception of nanostructures, in this turbulent diffusion flame initially consists of smaller PAH units. The evolution of the average nanostructure also appears to follow a more chemically driven pathway, where nanostructure grow through polymerisation of aromatic units into oligomers, like that observed in premixed flames [97, 205]. Growth via this mechanism is expected to have a lesser effect on decay time in comparison to more layered, and packed PAH clustering held together by van der Waals forces [51]. The enhanced mixing in the turbulent conditions

absolutely impacts the formation mechanisms of soot. In regions further downstream than those measured, the presence of nanostructures will likely begin to decline as pockets of nanostructures and soot begin to interact more with the oxidising flame front [248].

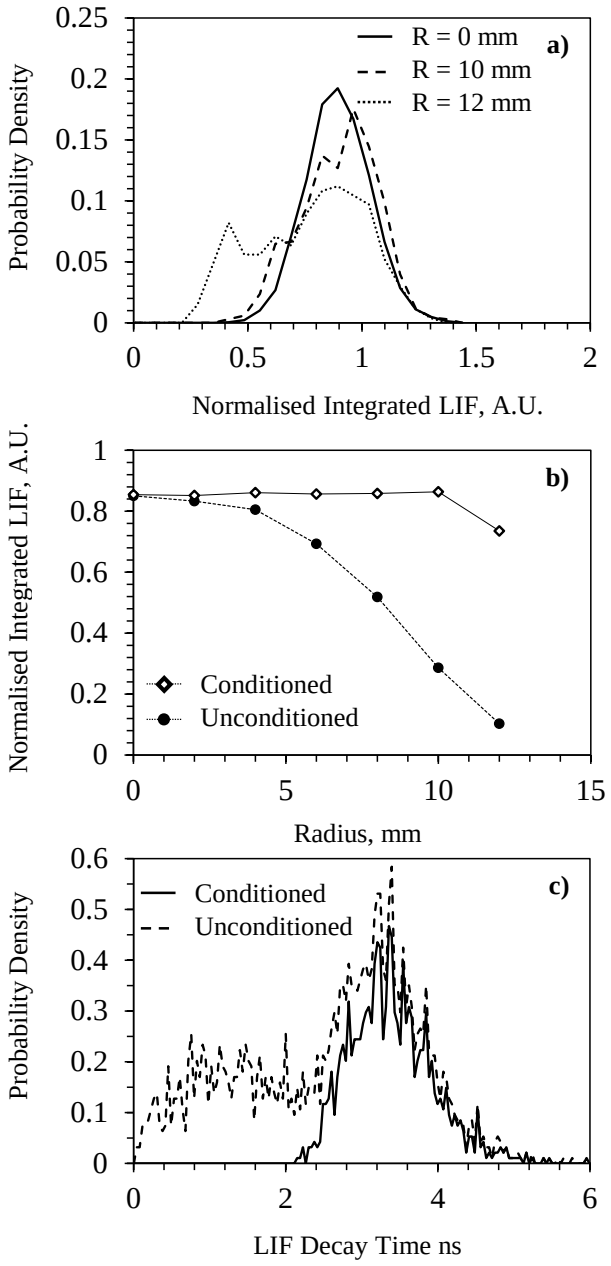

Figure 7.4: a) Conditioned PDFs of LIF @ 350 nm at HAB = 150 mm: radius = 0, 10 and 12 mm. b) Unconditioned and conditioned mean profile for LIF @ 350 nm at HAB = 150 mm. c) Unconditioned and conditioned PDF of evaluated decay times on the centreline at 340 mm.

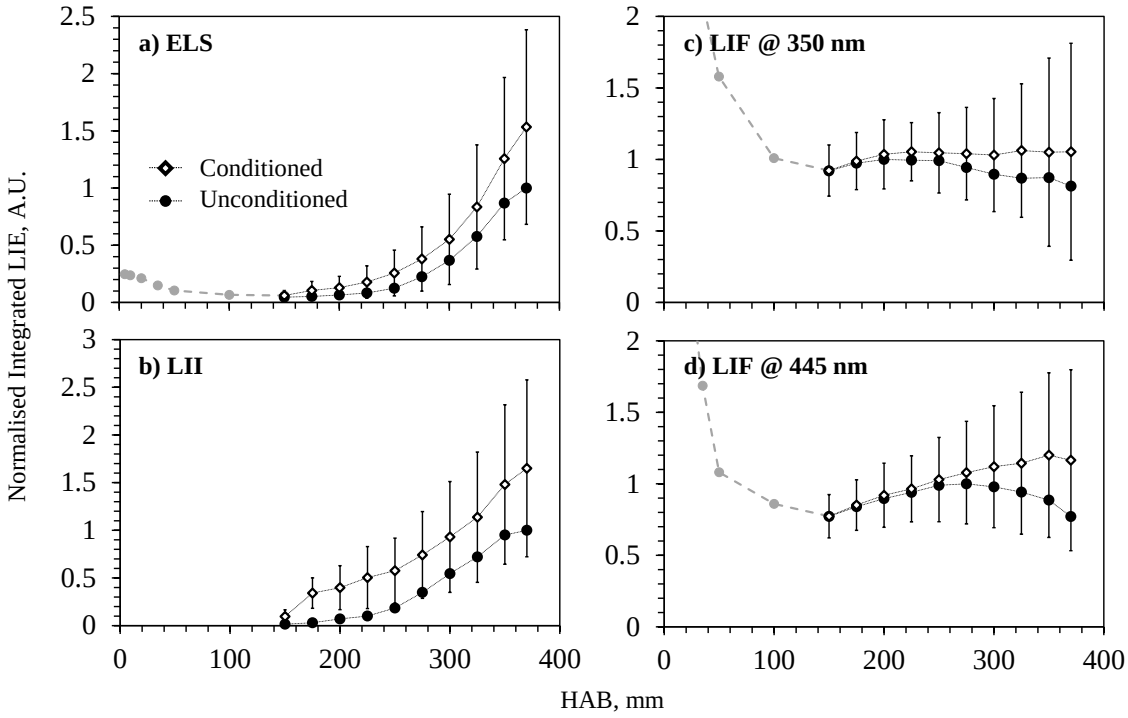

Figure 7.5: Conditioned and unconditioned mean integrated LIE signal along centreline of turbulent flame with standard deviation of the signal conditioned signals. a) ELS, b) LII c), LIF @ 350 nm d) and LIF @ 445 nm. Measurements substantially impacted by photofragmentation are presented in grey.

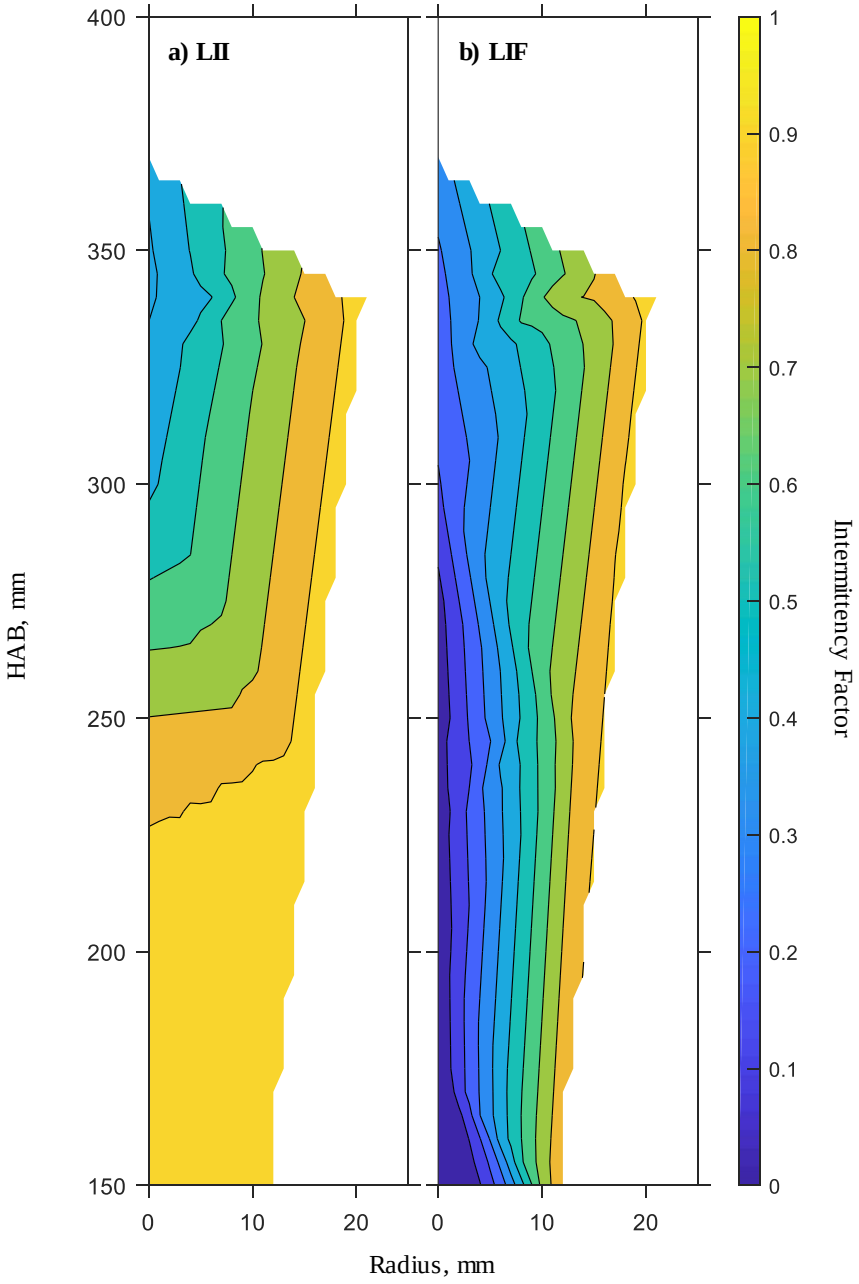

Figure 7.6: Intermittency factor contours of a) LII and b) LIF.

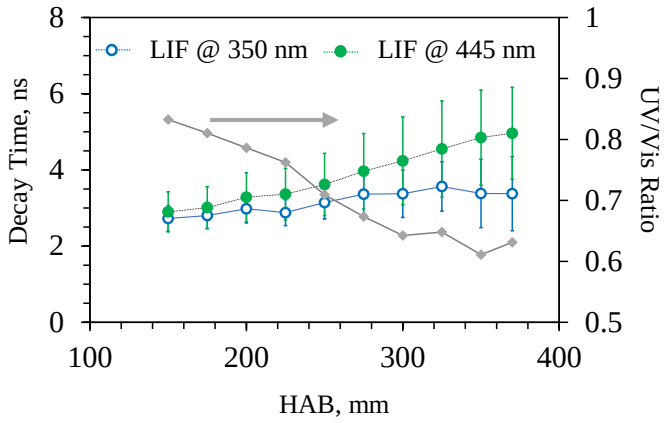

Figure 7.7: Axial conditioned mean LIF decay times and UV/Vis intensity ratio.

Figure 7.8 displays the conditioned radial profiles at 150 mm, 245 mm and 340 mm for the LIF @ 350 nm and LII. In terms of the flame structure, there is no defined peak in either 350 nm or 445 nm LIF radial profiles, which show that nanoparticles are formed uniformly across the flame. This trend is evident only after the conditioning is applied, as evidenced by Figures 7.3b and 7.4b. This is very different to the radial trends seen in Chapter 5, of the laminar diffusion flames and some trends of NOC seen in other turbulent diffusion flames [99]. LII, on the other hand, is not detected at 150 mm and is observed at 245 and 350 mm HAB. The LII signal in these planes do show some structure, similar to laminar diffusion soot wings seen in Chapter 5, with the conditioned average peak occurring between 8 and 12 mm off the centreline for both 245 and 350 mm HAB. However, these structures are not well defined and agree with other soot measurements in turbulent flames [59, 248]. It is known that increased turbulence, and thus strain rate, leads to higher degree of radial soot uniformity [247, 248] meaning that soot concentration is mostly governed by residence time in these cases, providing it is not completely suppressed [58]. But increased Reynolds number also reduces local soot concentration due to increased mixing rate [247, 249, 254] and the overlapping of oxidising OH layers [62, 248].

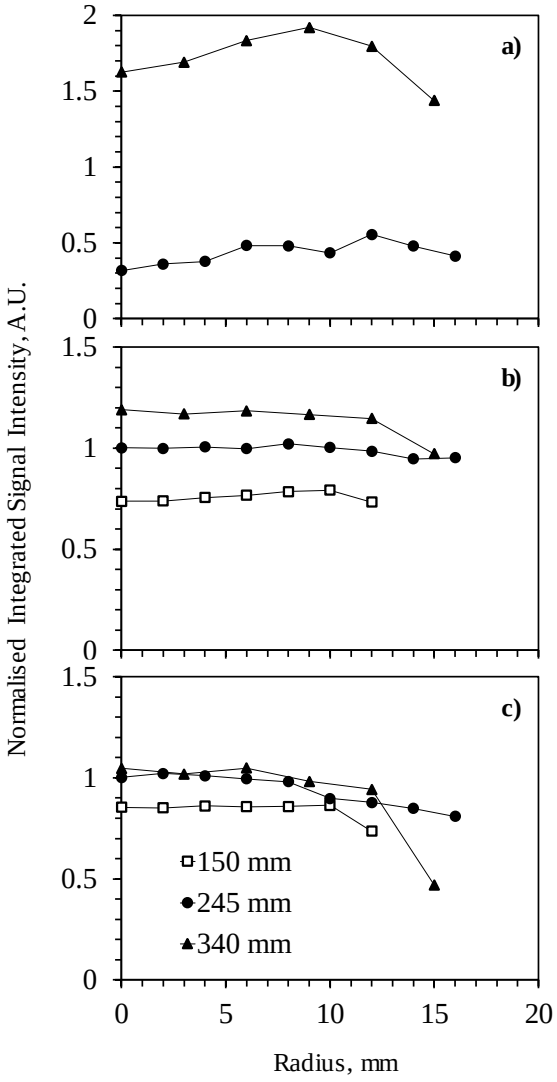

Figure 7.8: Conditioned radial profiles measured at HAB = 150, 245 and 340 mm for the three different LIEs: a) LII, b) LIF @ 445 nm and c) LIF @ 350 nm.

Downstream in the flame, there is a large production of soot while LIF is still detectable. Similar observations on the spatial co-existence of soot and nanostructures have previously been made via TEM measurements in turbulent ethylene and acetylene flames [159]. From the conditioned mean alone, it is not possible to draw conclusions on the instantaneous relation between the two signals. Since signals from the PMTs are collected simultaneously, there is the possibility to verify the simultaneous presence of nanoparticles and soot. Figure 7.9 highlights the dynamics of the production of both nanoparticles and soot in turbulent combustion, reporting the scatter plot of LII and LIF @ 350 nm occurrence at 245 mm and 340 mm on the centreline. The occurrences indicated in grey are those that

were rejected either in the LII conditioned mean or in the LIF @ 350 nm conditioned mean. At both locations, a large number of instances were detected when there was no LII but significant LIF @ 350 nm. Conversely, comparatively few instances were detected when LII was present without significant LIF. Unsurprisingly the soot concentration (LII) is lower with less scatter at 245 mm than at 340 mm due to the difference in average residence time between the two locations. This plot confirms that nanoparticles are formed or at least present when large soot particles are detected. This is consistent with the mean profiles reported earlier and confirms the co-presence of nanoparticles and larger soot, not just spatially but instantaneously as well. These scatter results are also generally in agreement with similar plot produced by Franzelli et al. [62]. Although some oxidation is likely to be occurring at 340 mm and higher, this region of the flame is very much dominated by soot growth and even inception.

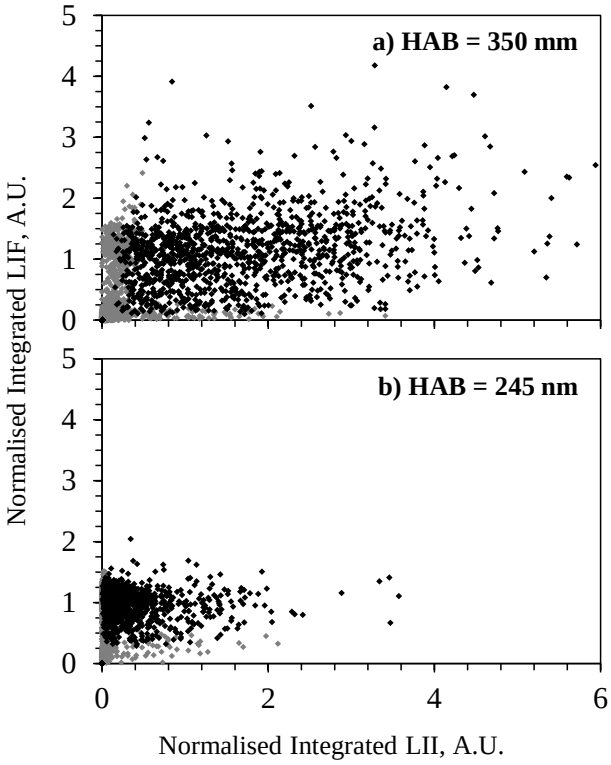

Figure 7.9: Scatter plot of LII vs. LIF @ 350 nm signal on the centreline at a) HAB = 340 mm and b) HAB = 245 mm. Measurements that met the conditioning for both LII and LIF @ 350 nm are in black. Measurements discharged by S/B threshold for one or both signals are displayed in grey.

7.3 Conclusion

Application of the time-resolved LIE setup to a turbulent flame has demonstrated the technique's capability to resolve transients of LIF and LII in turbulent flames. Instantaneous measurements with resolvable signal levels for intensity and decay time allowed the detection and tracking of nanostructures and soot simultaneously within this sooting diffusion flame. Data conditioning allowed the observation of intermittency and active particle formation and growth instances within the flame. Much like what is observed in laminar flames nanostructure formation precedes the formation of soot. However, moving downstream the presence of nanostructures remains in the presence of incandescent soot. The simultaneous acquisition of LIF and LII signals highlights that nanostructures and soot often co-exist both spatially and instantaneously in downstream regions of the flame, unlike laminar diffusion flames. In downstream regions, there are instances where nanoparticles are largely detected without the presence of soot. However, there are very few instances found where significant soot is present without nanostructures also being detected. Reaching the end of average soot growth region, particle inception is still active. While instantaneously the flame shows a spread of LIF and LII intensities due to turbulence, spatially soot formation is more defined. Turbulent mixing results in relatively flat conditioned mean LIF and LII radial profiles and presents average nanostructure inception and evolution with some similarities to rich premixed flames. An initially blue-shifted spectrum and relatively low LIF decay times indicate favouring of the chemical growth pathway that is preferred in non-pyrolytic conditions.

Chapter 8: Concluding Remarks

8.1 General Conclusions

The primary objectives of this thesis were to develop a time-resolved laser-induced emission (LIE) technique capable of capturing instantaneous emissions in turbulent conditions and secondly to confirm the hybrid nature of nanoparticles (semi-solid structure while retaining molecular qualities) in combustion. Nanoparticles that exist between the largest PAH and the smallest primary soot particle exhibit absorption and fluorescence similar to that of the constituent PAH. Investigation in rich premixed flames, containing and not containing soot, showed that LIF is present in areas where nanostructure of the size between 2 and 10 nm are found. This fluorescence presented long exponential lifetimes (> 2 ns) at elevated temperatures which cannot be attributed to gas phase PAH, but rather to PAH moieties bound within semi-rigid structures such as those measured by DMA. Whilst this revelation is not strictly new, its acceptance in current literature is rather understated and often neglected in the interpretation of fluorescence measurements. Long lived fluorescence is invariably found in other flames and conditions at or beyond the sooting threshold.

The implementation of the in-house designed and manufactured LIE system with highly sensitive photomultiplier tubes (PMT) is shown here to adequately capture resolvable instantaneous ELS, LIF and LII emission signals. Investigations in a sooting turbulent flame provided unique insight into soot formation by assessing simultaneous LIF and LII measurements. The co-existence of nanostructures and soot in downstream regions is identified by the co-existence of LIF and LII. This shows that in the turbulent environment produced by a diffusion flame with a Reynolds number of 10,000, continuing particle

inception contributes to the soot growth in downstream regions, well beyond the initial nanostructure inception region.

Measurements in laminar premixed, partially premixed and diffusion flames were utilised to corroborate theorised particle inception pathways and their relevance to the specific thermochemical evolution in each flame. Inference on the nature of the nanostructures is made based on the spectrum and the decay times. Rich premixed flames in literature present some evidence to suggest that, under these conditions, soot inception proceeds via the polymerisation of PAH into loose oligomers. This translates to shorter emission wavelengths, similar to that of its constituent PAHs and relatively short LIF lifetimes, as is demonstrated here. These characteristics are also shared by the turbulent flame studied, highlighting the influence of turbulent mixing on the resultant soot formation. Laminar diffusion flames, on the other hand, presented obvious redshifted LIF and longer decay times that can be attributed to a layered nanostructure formed from peri-condensed PAH interacting via van der Walls attractive forces. Nanostructures formed in partially premixed flames exist somewhere between premixed and diffusion extremes. Increasing partial premixing exhibits incepted nanostructures with blue-shifted spectrum, similar to the premixed cases, however, continued growth is similar to that seen in diffusion flames via a more physical growth mechanism exhibiting red-shifts and increasing decay times. Additionally, the partially premixed study highlighted that dilution effects hide the enhancement of soot formation in the presence of small amounts of oxygen in an otherwise pyrolytic region.

8.2 Recommendations and Future Work

Whilst the technique has proven valuable in producing some quantitative and semi-quantitative results, its capability to probe the nature of nanostructures and soot particles is far from exhausted.

There remains significant scope for further extension and development of the technique with respect to elastic light scattering (ELS) and time-resolved Laser-Induced Incandescence (LII). Time-resolved LII can be used as a tool for average soot particle sizing, where a model accounting for absorption, conduction, radiation and other contributors (with inherent assumptions) predicts the primary particle diameter [43]. While LII in this work was used primarily as a marker for soot particles and in some cases soot volume fraction, pursuing soot modelling in future work will increase the richness of the technique and extend its capability to assessing the nature of soot particles. Some recommendations are made to improve the suitability of the 1064 nm LII for modelling.

By making the spatial laser beam profile “top hat” will result in uniform heating of the probed soot particles, as opposed to a Gaussian beam profile that unevenly distributes its energy across the beam. Additionally, it would be beneficial to operate LII at lower fluences to exist below the sublimation threshold to avoid complicating the particle sizing model by eliminating the sublimation terms in the model. Whilst this means that particles will not heated up to the sublimation point (≈ 4000 K), this is mitigated by the fact that LII is measured at multiple wavelengths (PMT2, 3 and 4) and pyrometry can be used to determine LII temperature [255]. Multi angle scattering in literature has been used to great effect and presents the possibility to compliment the technique with the ability to assess soot aggregates radius of gyration [256, 257] and fractal dimensions [148, 258, 259]. Additionally, the combination of calibrated ELS and LII, gives the possibility to extract particle diameter (d63) due to the difference of size dependence of LII and ELS signals.

The temporal resolution of the Laser-Induced Fluorescence measurements potentially lends itself to time-resolved fluorescence anisotropy (TRFPA). TRFPA allows the measurement of the depolarisation time of the fluorescent particle that can be used to assess the particle diameter, some more details are given in Section 2.2.2. This is a valuable technique for the sizing of fluorescent nanostructures [119, 122, 184], without the need for ex-situ measurements.

The experimental system and technique developed in this thesis shows great promise in investigating turbulent combustion. In this thesis, only the study of one turbulent flame is presented and leaves the vast possibilities for additional studies. The aim of this thesis was not to be a parametric investigation of all possible parameters in a turbulent flame. However, preliminary work has recently begun using and refining the system and technique reported in this thesis to explore Reynolds number, fuel type and the influence of dilution and premixing in turbulent flames, a few of many avenues for future work.

Appendix A: Burner Dimensions and Assembly Drawings

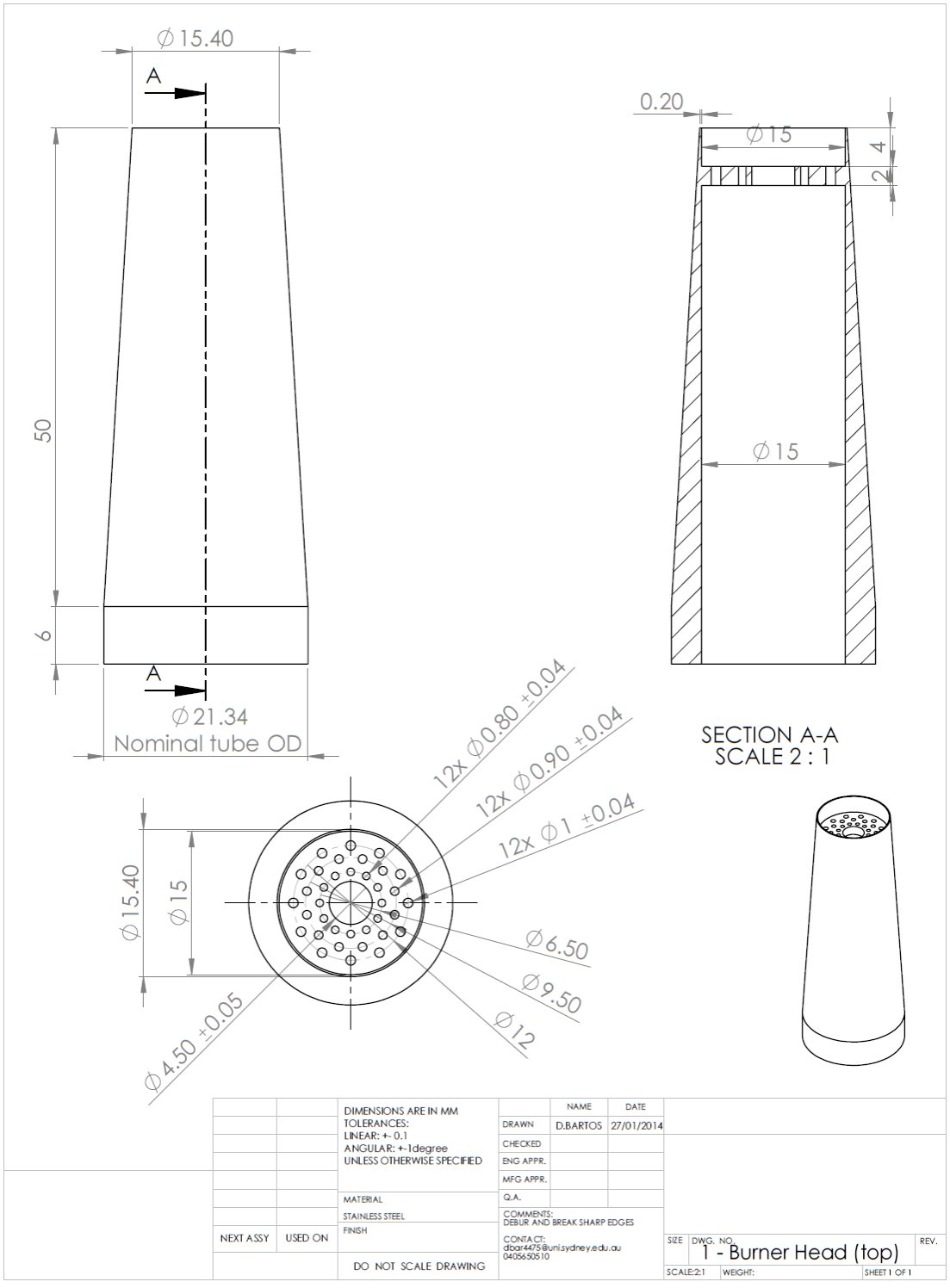
∅15.40
A
50
6
A
∅21.34
Nominal tube OD
0.20
∅15
4
2
∅15
SECTION A-A
SCALE 2 : 1
12x ∅0.80 ±0.04
12x ∅0.90 ±0.04
12x ∅1 ±0.04
∅15.40
∅15
∅6.50
∅9.50
∅12
∅4.50 ±0.05
DIMENSIONS ARE IN MM
TOLERANCES:
LINEAR: +- 0.1
ANGULAR: +-1degree
UNLESS OTHERWISE SPECIFIED
MATERIAL
STAINLESS STEEL
FINISH
NEXT ASSY
USED ON
DO NOT SCALE DRAWING
NAME
DATE
DRAWN
D.BARTOS
27/01/2014
CHECKED
ENG APPR.
MFG APPR.
Q.A.
COMMENTS:
DEBUR AND BREAK SHARP EDGES
CONTACT:
dbar4475@uni.sydney.edu.au
0405650510
SIZE
DWG. NO.
1 - Burner Head (top)
REV.
SCALE:2:1
WEIGHT:
SHEET 1 OF 1

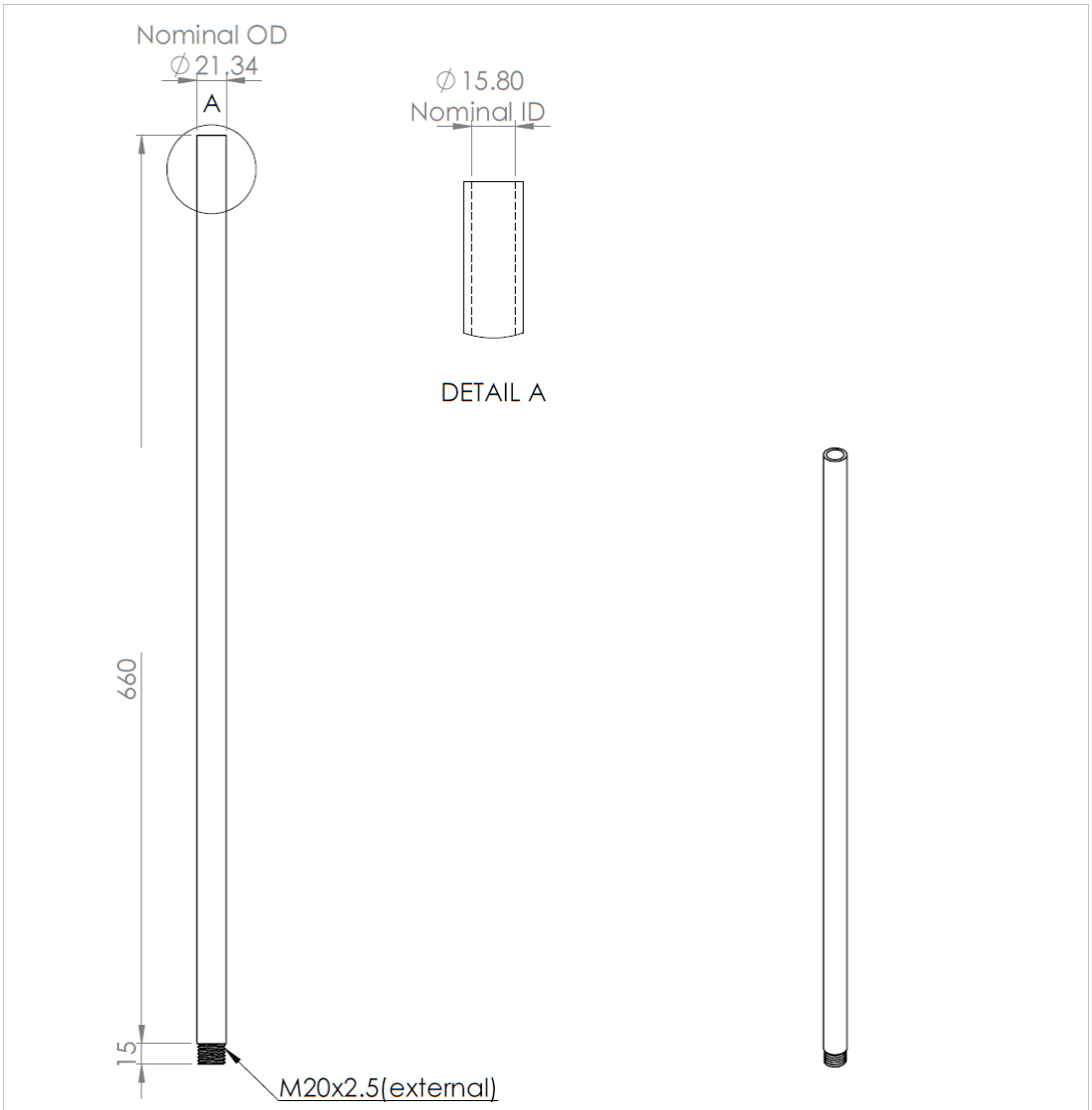

		DIMENSIONS ARE IN MM TOLERANCES: LINEAR: +- 0.1 ANGULAR: +-1degree UNLESS OTHERWISE SPECIFIED		NAME	DATE
			DRAWN	D.BARTOS	27/01/2014
			CHECKED		
			ENG APPR.		
			MFG APPR.		
			Q.A.		
		MATERIAL STAINLESS STEEL	COMMENTS: **CONFIRM DIMENSIONS BEFORE CUTTING TUBE TO LENGHT** DEBUR AND BREAK SHARP EDGES		
NEXT ASSY	USED ON	FINISH			
		DO NOT SCALE DRAWING	CONTACT: dbar4475@uni.sydney.edu.au 0405650510	SIZE / DWG. NO. 2 - Burner Head (bottom)	REV.
				SCALE:1:4 WEIGHT:	SHEET 1 OF 1

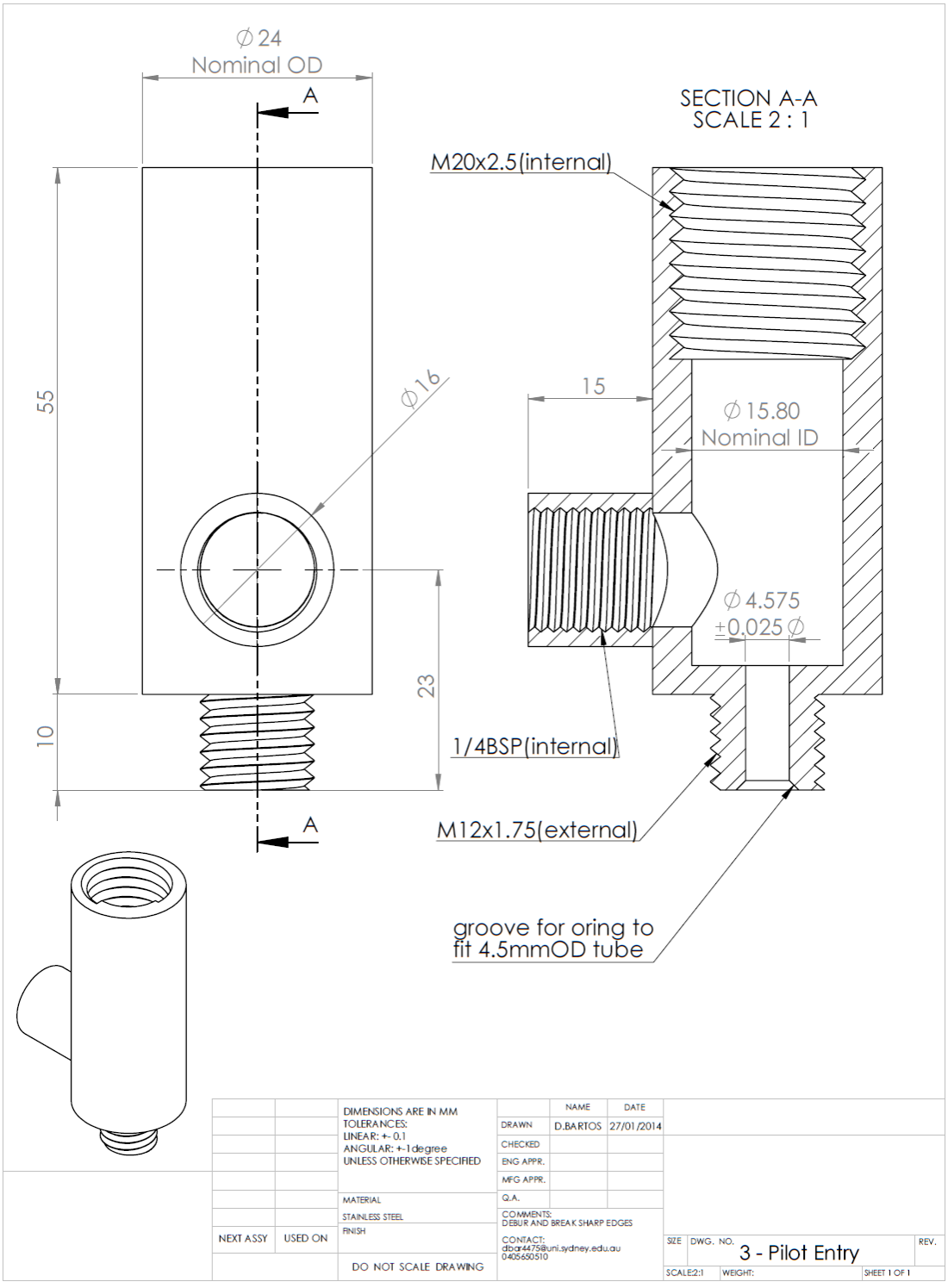
∅24
Nominal OD
A
SECTION A-A
SCALE 2 : 1
M20x2.5(internal)
55
∅16
15
∅15.80
Nominal ID
∅4.575
±0.025∅
23
10
1/4BSP(internal)
M12x1.75(external)
A
groove for oring to
fit 4.5mmOD tube
DIMENSIONS ARE IN MM
TOLERANCES:
LINEAR: +- 0.1
ANGULAR: +-1 degree
UNLESS OTHERWISE SPECIFIED
MATERIAL
STAINLESS STEEL
FINISH
NEXT ASSY
USED ON
DO NOT SCALE DRAWING
NAME
DATE
DRAWN
D.BARTOS
27/01/2014
CHECKED
ENG APPR.
MFG APPR.
Q.A.
COMMENTS:
DEBUR AND BREAK SHARP EDGES
CONTACT:
dbar4475@uni.sydney.edu.au
0405650510
SIZE
DWG. NO.
3 - Pilot Entry
REV.
SCALE:2:1
WEIGHT:
SHEET 1 OF 1

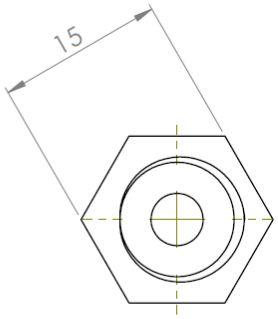

SECTION A-A

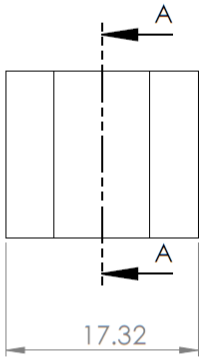

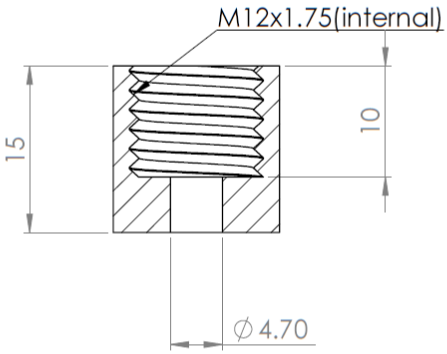

		DIMENSIONS ARE IN MM TOLERANCES: LINEAR: +- 0.1 ANGULAR: +-1degree UNLESS OTHERWISE SPECIFIED		NAME	DATE
			DRAWN	D.BARTOS	27/01/2014
			CHECKED		
			ENG APPR.		
			MFG APPR.		
		MATERIAL	Q.A.		
		STAINLESS STEEL	COMMENTS: DEBUR AND BREAK SHARP EDGES		
NEXT ASSY	USED ON	FINISH	CONTACT: dbar4475@uni.sydney.edu.au 0405650510		
		DO NOT SCALE DRAWING			

SIZE	DWG. NO.	REV.
	4 - Seal Nut	
SCALE:2:1	WEIGHT:	SHEET 1 OF 1

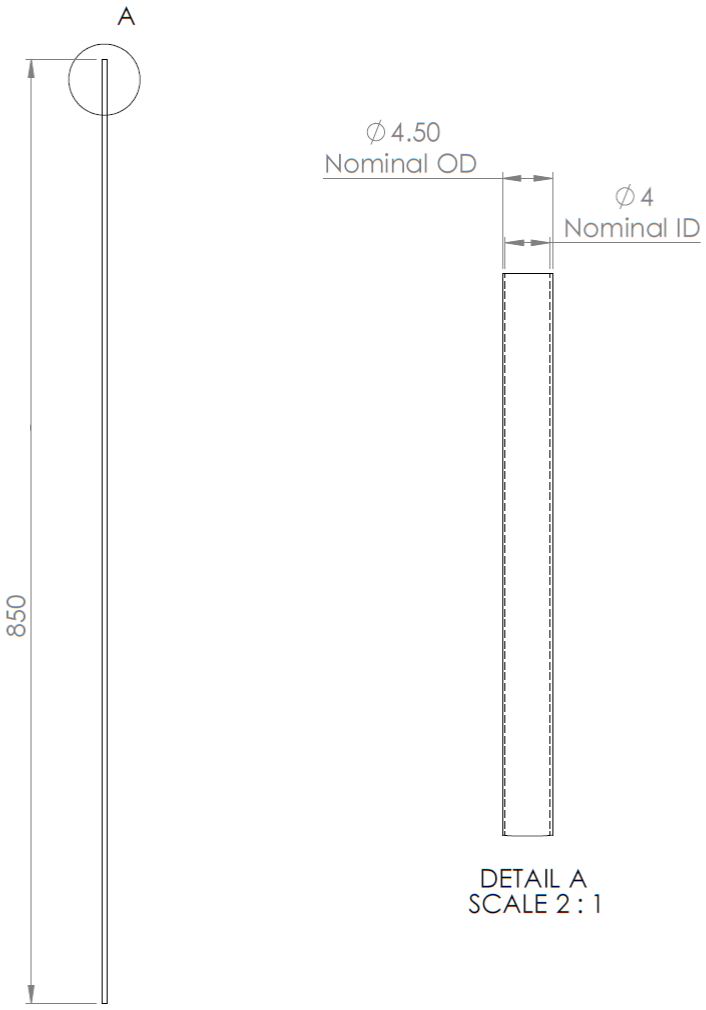

		DIMENSIONS ARE IN MM TOLERANCES: LINEAR: +- 0.1 ANGULAR: +-1degree UNLESS OTHERWISE SPECIFIED		NAME	DATE
			DRAWN	D.BARTOS	27/01/2014
			CHECKED		
			ENG APPR.		
			MFG APPR.		
		MATERIAL	Q.A.		
		STAINLESS STEEL	COMMENTS: **CONFIRM DIMENSION BEFORE CUTTING TUBE TO LENGTH** DEBUR AND BREAK SHARP EDGES CONTACT: dbar4475@uni.sydney.edu.au 0405650510		
NEXT ASSY	USED ON	FINISH			
		DO NOT SCALE DRAWING			

SIZE	DWG. NO. 5 - Jet Tube	REV.
SCALE:1:2	WEIGHT:	SHEET 1 OF 1

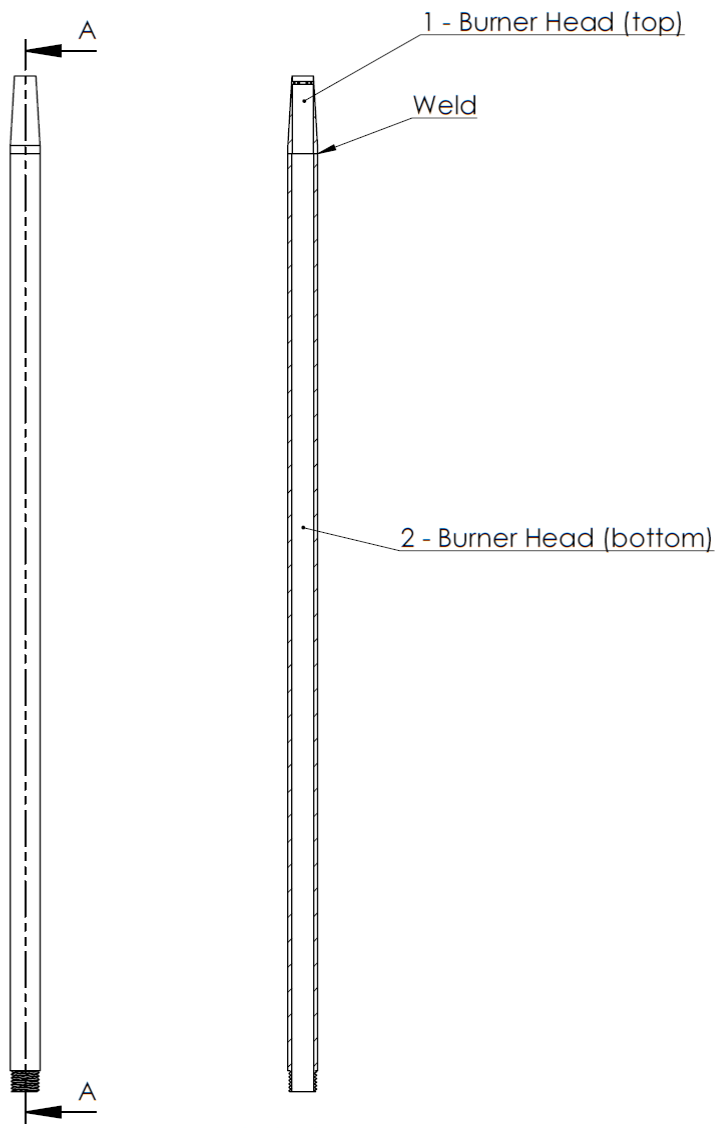

SECTION A-A
SCALE 1 : 4

		DIMENSIONS ARE IN MM TOLERANCES: LINEAR: +- 0.1 ANGULAR: +-1 degree UNLESS OTHERWISE SPECIFIED		NAME	DATE
			DRAWN	D.BARTOS	27/01/2014
			CHECKED		
			ENG APPR.		
			MFG APPR.		
		MATERIAL	Q.A.		
		STAINLESS STEEL	COMMENTS: DEBUR AND BREAK SHARP EDGES		
NEXT ASSY	USED ON	FINISH	CONTACT: db.ar4475@uni.sydney.edu.au 0405650510		
		DO NOT SCALE DRAWING			

ASSEMBLY NOTES

PARTS:
1 - Burner Head (top)
2 - Burner Head (bottom)

SIZE	DWG. NO.	REV.
	Assem - Burner Head	
SCALE:1:4	WEIGHT:	SHEET 1 OF 1

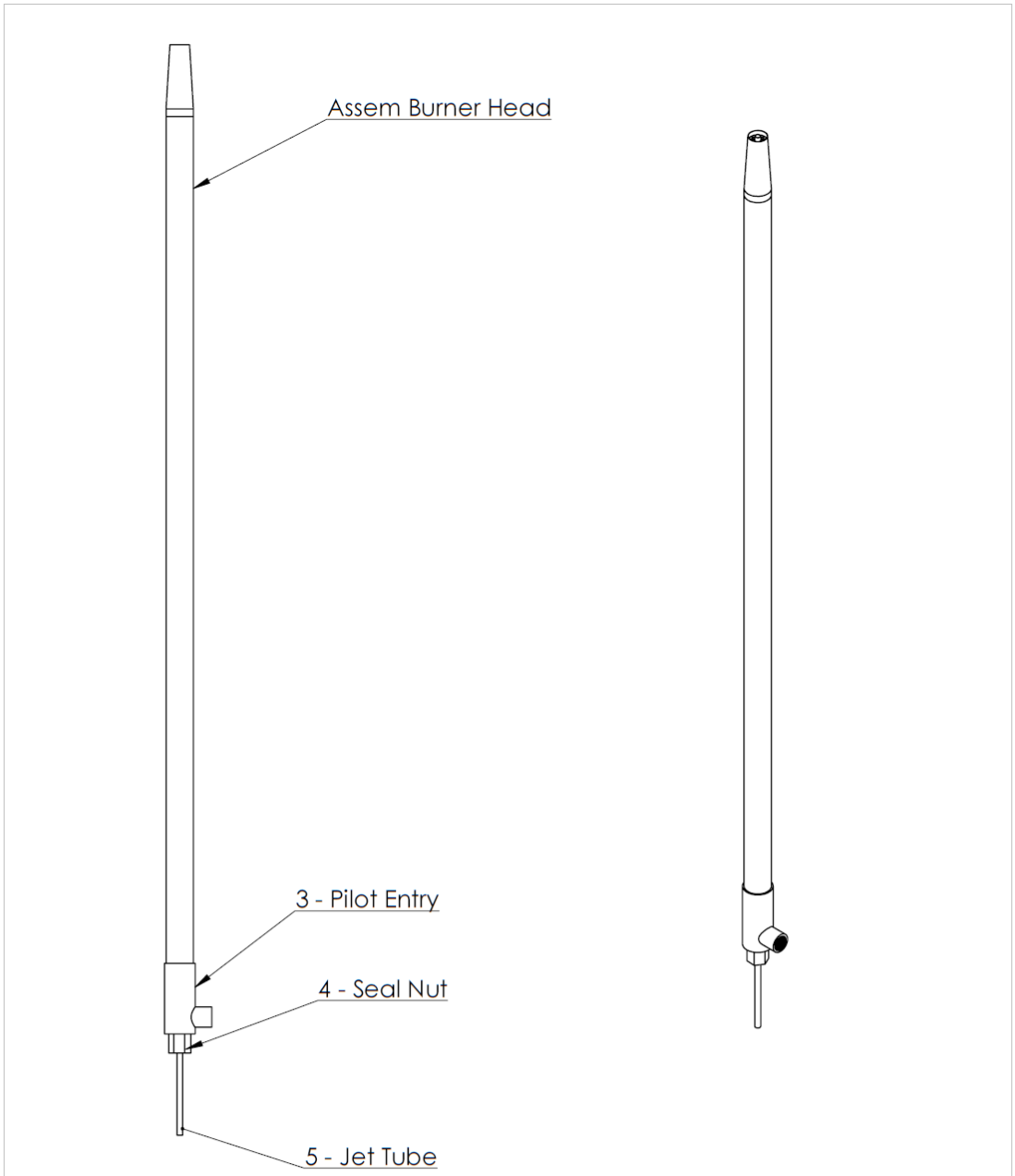

		DIMENSIONS ARE IN MM TOLERANCES: LINEAR: +- 0.1 ANGULAR: +-1degree UNLESS OTHERWISE SPECIFIED		NAME	DATE
			DRAWN	D.BARTOS	27/01/2014
			CHECKED		
			ENG APPR.		
			MFG APPR.		
			Q.A.		
		MATERIAL STAINLESS STEEL	COMMENTS: DEBUR AND BREAK SHARP EDGES		
NEXT ASSY	USED ON	FINISH	CONTACT: dbar4475@uni.sydney.edu.au 0405650510		
		DO NOT SCALE DRAWING			

ASSEMBLY NOTES

PARTS:
Assem Burner Head
3 - Pilot Entry
4 - Seal Nut
5 - Jet Tube
o-ring

SIZE	DWG. NO.	REV.
	Assem - Complete	
SCALE:1:2	WEIGHT:	SHEET 1 OF 1

References

[1] M. Sirignano, D. Bartos, M. Conturso, M. Dunn, A. D'Anna, A.R. Masri, Detection of nanostructures and soot in laminar premixed flames, Combustion and Flame 176 (2017) 299-308.
[2] D. Bartos, M. Dunn, M. Sirignano, A. D'Anna, A.R. Masri, Tracking the evolution of soot particles and precursors in turbulent flames using laser-induced emission, Proceedings of the Combustion Institute 36 (2017) 1869-1876.
[3] I.E. Agency, World Energy Outlook 2017, 2017.
[4] I.p.o.c. change, Climate Change 2013: The Physical Science Basis, 2013.
[5] D.W. Dockery, C.A. Pope, X. Xu, J.D. Spengler, J.H. Ware, M.E. Fay, B.G. Ferris, F.E. Speizer, An Association between Air Pollution and Mortality in Six U.S. Cities, The New England Journal of Medicine 329 (1993) 1753-1759.
[6] G. Oberdörster, E. Oberdörster, J. Oberdörster, Nanotoxicology: An Emerging Discipline Evolving from Studies of Ultrafine Particles, Environmental Health Perspectives 113 (2005) 823-839.
[7] I.M. Kennedy, The health effects of combustion-generated aerosols, Proceedings of the Combustion Institute 31 (2007) 2757-2770.
[8] T. Osunsanya, G. Prescott, A. Seaton, Acute Respiratory Effects of Particles: Mass or Number?, Occupational and Environmental Medicine 58 (2001) 154-159.
[9] C.A. Pope Iii, D.W. Dockery, Health effects of fine particulate air pollution: Lines that connect, Journal of the Air and Waste Management Association 56 (2006) 709-742.
[10] A. Sydbom, A. Blomberg, S. Parnia, N. Stenfors, T. Sandstrom, S.E. Dahlen, Lungmedicin, f. Medicinska, u. Umeå, m. Institutionen för folkhälsa och klinisk, Health effects of diesel exhaust emissions, European Respiratory Journal 17 (2001) 733-746.
[11] C.A. Pope, D.W. Dockery, J. Schwartz, Review of Epidemiological Evidence of Health Effects of Particulate Air Pollution, Inhalation Toxicology 7 (1995) 1-18.
[12] B.J. Finlayson-Pitts, J.N. Pitts, Tropospheric Air Pollution: Ozone, Airborne Toxics, Polycyclic Aromatic Hydrocarbons, and Particles, Science 276 (1997) 1045-1052.
[13] L.A. Sgro, A. De Filippo, G. Lanzuolo, A. D'Alessio, Characterization of nanoparticles of organic carbon (NOC) produced in rich premixed flames by differential mobility analysis, Proceedings of the Combustion Institute 31 (2007) 631-638.
[14] E. Commission, Emissions in the automotive sector. http://ec.europa.eu/growth/sectors/automotive/environment-protection/emissions/index_en.htm.
[15] A. D'Anna, Combustion-formed nanoparticles, Proceedings of the Combustion Institute 32 (2009) 593-613.

[16] Y.J. Kaufman, R.S. Fraser, The Effect of Smoke Particles on Clouds and Climate Forcing, Science 277 (1997) 1636-1639.
[17] V. Ramanathan, G. Carmichael, Global and Regional Climate Changes Due to Black Carbon, 2008.
[18] T.C. Bond, S.J. Doherty, D.W. Fahey, P.M. Forster, T. Berntsen, B.J. DeAngelo, M.G. Flanner, S. Ghan, B. Kärcher, D. Koch, S. Kinne, Y. Kondo, P.K. Quinn, M.C. Sarofim, M.G. Schultz, M. Schulz, C. Venkataraman, H. Zhang, S. Zhang, N. Bellouin, S.K. Guttikunda, P.K. Hopke, M.Z. Jacobson, J.W. Kaiser, Z. Klimont, U. Lohmann, J.P. Schwarz, D. Shindell, T. Storelvmo, S.G. Warren, C.S. Zender, Bounding the role of black carbon in the climate system: A scientific assessment, Journal of Geophysical Research: Atmospheres 118 (2013) 5380-5552.
[19] J. Hansen, L. Nazarenko, Soot Climate Forcing via Snow and Ice Albedos, Proceedings of the National Academy of Sciences of the United States of America 101 (2004) 423-428.
[20] S.R. Turns, An introduction to combustion: concepts and applications, 3rd ed., McGraw-Hill, New York, 2012.
[21] M. Conturso, M. Sirignano, A. D'Anna, Effect of furanic biofuels on particles formation in premixed ethylene–air flames: An experimental study, Fuel 175 (2016) 137-145.
[22] M. Conturso, M. Sirignano, A. D'Anna, Effect of 2,5-dimethylfuran doping on particle size distributions measured in premixed ethylene/air flames, Proceedings of the Combustion Institute 36 (2017) 985-992.
[23] P. Minutolo, M. Commodo, A. Santamaria, G. De Falco, A. D'Anna, Characterization of flame-generated 2-D carbon nano-disks, Carbon 68 (2014) 138-148.
[24] L.D. Smoot, D.T. Pratt, Pulverized-coal combustion and gasification: theory and applications for continuous flow processes, Plenum Press, New York, 1979.
[25] A. Williams, Combustion of droplets of liquid fuels: A review, Combustion and Flame 21 (1973) 1-31.
[26] S. Bejaoui, X. Mercier, P. Desgroux, E. Therssen, Laser induced fluorescence spectroscopy of aromatic species produced in atmospheric sooting flames using UV and visible excitation wavelengths, Combustion and Flame 161 (2014) 2479-2491.
[27] M.D. Smooke, M.B. Long, B.C. Connelly, M.B. Colket, R.J. Hall, Soot formation in laminar diffusion flames, Combustion and Flame 143 (2005) 613-628.
[28] H. Wang, Formation of nascent soot and other condensed-phase materials in flames, Proceedings of the Combustion Institute 33 (2011) 41-67.
[29] P. Desgroux, X. Mercier, K.A. Thomson, Study of the formation of soot and its precursors in flames using optical diagnostics, Proceedings of the Combustion Institute 34 (2013) 1713-1738.
[30] H.A. Michelsen, Probing soot formation, chemical and physical evolution, and oxidation: A review of in situ diagnostic techniques and needs, Proceedings of the Combustion Institute 36 (2017) 717-735.
[31] D.B. Kittelson, Engines and nanoparticles: a review, Journal of Aerosol Science 29 (1998) 575-588.
[32] H. Bockhorn, Soot formation in combustion, Berlin-Heidelberg-NewYork, 1994.
[33] H. Bockhorn, A. D'Anna, A. F. Sarofim, Combustion generated fine carbonaceous particles, KIT Scientific Publishing2009.

[34] A. D'Alessio, A. D'Anna, A. D'Orsi, P. Minutolo, R. Barbella, A. Ciajolo, Precursor formation and soot inception in premixed ethylene flames, Symposium (International) on Combustion 24 (1992) 973-980.
[35] B. Zhao, Z.W. Yang, J.J. Wang, M.V. Johnston, H. Wang, Analysis of soot nanoparticles in a laminar premixed ethylene flame by scanning mobility particle sizer, Aerosol Science and Technology 37 (2003) 611-620.
[36] B. Zhao, Z. Yang, M.V. Johnston, H. Wang, A.S. Wexler, M. Balthasar, M. Kraft, Measurement and numerical simulation of soot particle size distribution functions in a laminar premixed ethylene-oxygen-argon flame, Combustion and Flame 133 (2003) 173-188.
[37] M.M. Maricq, Size and charge of soot particles in rich premixed ethylene flames, Combustion and Flame 137 (2004) 340-350.
[38] B. Zhao, Z. Yang, Z. Li, M.V. Johnston, H. Wang, Particle size distribution function of incipient soot in laminar premixed ethylene flames: effect of flame temperature, Proceedings of the Combustion Institute 30 (2005) 1441-1448.
[39] M. Thierley, H.H. Grotheer, M. Aigner, Z. Yang, A. Abid, B. Zhao, H. Wang, On existence of nanoparticles below the sooting threshold, Proceedings of the Combustion Institute 31 (2007) 639-647.
[40] M. Alfè, B. Apicella, R. Barbella, J.N. Rouzaud, A. Tregrossi, A. Ciajolo, Structure–property relationship in nanostructures of young and mature soot in premixed flames, Proceedings of the Combustion Institute 32 (2009) 697-704.
[41] R.L. Vander Wal, Soot precursor carbonization: Visualization using LIF and LII and comparison using bright and dark field TEM, Combustion and Flame 112 (1998) 607-616.
[42] R.L. Vander Wal, Onset of carbonization: Spatial location via simultaneous LIF-LII and characterization via TEM, Combustion Science and Technology 118 (1996) 343-360.
[43] H.A. Michelsen, C. Schulz, G.J. Smallwood, S. Will, Laser-induced incandescence: Particulate diagnostics for combustion, atmospheric, and industrial applications, Progress in Energy and Combustion Science 51 (2015) 2-48.
[44] S. De Iuliis, F. Migliorini, F. Cignoli, G. Zizak, Peak soot temperature in laser-induced incandescence measurements, Applied Physics B 83 (2006) 397-402.
[45] F. Goulay, P.E. Schrader, H.A. Michelsen, Effect of the wavelength dependence of the emissivity on inferred soot temperatures measured by spectrally resolved laser-induced incandescence, Applied Physics B 100 (2010) 655-663.
[46] D.R. Snelling, K.A. Thomson, F. Liu, G.J. Smallwood, Comparison of LII derived soot temperature measurements with LII model predictions for soot in a laminar diffusion flame, Applied Physics B 96 (2009) 657-669.
[47] R. Lemaire, M. Mobtil, Modeling laser-induced incandescence of soot: a new approach based on the use of inverse techniques, Applied Physics B 119 (2015) 577-606.
[48] P. Minutolo, G. Gambi, A. D'Alessio, A. D'Anna, Optical and Spectroscopic Characterization of Rich Premixed Flames across the Soot Formation Threshold, Combustion Science and Technology 101 (1994) 311-325.
[49] A. D'Anna, M. Commodo, S. Violi, C. Allouis, J. Kent, Nano organic carbon and soot in turbulent non-premixed ethylene flames, Proceedings of the Combustion Institute 31 (2007) 621-629.

[50] A. D'Anna, M. Commodo, M. Sirignano, P. Minutolo, R. Pagliara, Particle formation in opposed-flow diffusion flames of ethylene: An experimental and numerical study, Proceedings of the Combustion Institute 32 (2009) 793-801.
[51] M. Sirignano, A. Collina, M. Commodo, P. Minutolo, A. D'Anna, Detection of aromatic hydrocarbons and incipient particles in an opposed-flow flame of ethylene by spectral and time-resolved laser induced emission spectroscopy, Combustion and Flame 159 (2012) 1663-1669.
[52] H. Bladh, N.E. Olofsson, T. Mouton, J. Simonsson, X. Mercier, A. Faccinetto, P.E. Bengtsson, P. Desgroux, t.f. Fysik, f. Gemensamma institutioner för naturvetenskapliga och tekniska, Förbränningsfysik, t.f.o.S. Common departments, Engineering, P. Combustion, i. Fysiska, F.o.T. Physics, P. Department of, u. Lunds, U. Lund, Probing the smallest soot particles in low-sooting premixed flames using laser-induced incandescence, Proceedings of the Combustion Institute 35 (2015) 1843-1850.
[53] G. Cléon, T. Amodeo, A. Faccinetto, P. Desgroux, Laser induced incandescence determination of the ratio of the soot absorption functions at 532 nm and 1064 nm in the nucleation zone of a low pressure premixed sooting flame, Applied Physics B 104 (2011) 297-305.
[54] P. Desgroux, A. Faccinetto, X. Mercier, T. Mouton, D. Aubagnac Karkar, A. El Bakali, Comparative study of the soot formation process in a "nucleation" and a "sooting" low pressure premixed methane flame, Combustion and Flame 184 (2017) 153-166.
[55] N.H. Qamar, Z.T. Alwahabi, Q.N. Chan, G.J. Nathan, D. Roekaerts, K.D. King, Soot volume fraction in a piloted turbulent jet non-premixed flame of natural gas, Combustion and Flame 156 (2009) 1339-1347.
[56] R. Lemaire, E. Therssen, P. Desgroux, Effect of ethanol addition in gasoline and gasoline–surrogate on soot formation in turbulent spray flames, Fuel 89 (2010) 3952-3959.
[57] J. Hayashi, N. Hashimoto, N. Nakatsuka, H. Tsuji, H. Watanabe, H. Makino, F. Akamatsu, Soot formation characteristics in a lab-scale turbulent pulverized coal flame with simultaneous planar measurements of laser induced incandescence of soot and Mie scattering of pulverized coal, Proceedings of the Combustion Institute 34 (2013) 2435-2443.
[58] M.E. Mueller, Q.N. Chan, N.H. Qamar, B.B. Dally, H. Pitsch, Z.T. Alwahabi, G.J. Nathan, Experimental and computational study of soot evolution in a turbulent nonpremixed bluff body ethylene flame, Combustion and Flame 160 (2013) 1298-1309.
[59] S.M. Mahmoud, G.J. Nathan, P.R. Medwell, B.B. Dally, Z.T. Alwahabi, Simultaneous planar measurements of temperature and soot volume fraction in a turbulent non-premixed jet flame, Proceedings of the Combustion Institute 35 (2015) 1931-1938.
[60] K.P. Geigle, M. Kohler, W. O'Loughlin, W. Meier, Investigation of soot formation in pressurized swirl flames by laser measurements of temperature, flame structures and soot concentrations, Proceedings of the Combustion Institute 35 (2015) 3373-3380.
[61] M. Köhler, K.-P. Geigle, T. Blacha, P. Gerlinger, W. Meier, Experimental characterization and numerical simulation of a sooting lifted turbulent jet diffusion flame, Combustion and Flame 159 (2012) 2620-2635.
[62] B. Franzelli, P. Scouflaire, S. Candel, Time-resolved spatial patterns and interactions of soot, PAH and OH in a turbulent diffusion flame, Proceedings of the Combustion Institute 35 (2015) 1921-1929.

[63] B.M. Crosland, K.A. Thomson, M.R. Johnson, Simultaneous instantaneous measurements of soot volume fraction, primary particle diameter, and aggregate size in turbulent buoyant diffusion flames, Proceedings of the Combustion Institute 35 (2015) 1851-1859.
[64] H. Richter, J.B. Howard, Formation of polycyclic aromatic hydrocarbons and their growth to soot—a review of chemical reaction pathways, Progress in Energy and Combustion Science 26 (2000) 565-608.
[65] C.S. McEnally, L.D. Pfefferle, B. Atakan, K. Kohse-Höinghaus, Studies of aromatic hydrocarbon formation mechanisms in flames: Progress towards closing the fuel gap, Progress in Energy and Combustion Science 32 (2006) 247-294.
[66] S.A. Skeen, H.A. Michelsen, K.R. Wilson, D.M. Popolan, A. Violi, N. Hansen, Near-threshold photoionization mass spectra of combustion-generated high-molecular-weight soot precursors, Journal of Aerosol Science 58 (2013) 86-102.
[67] K.H. Homann, Formation of large molecules, particulates and ions in premixed hydrocarbon flames; Progress and unresolved questions, Symposium (International) on Combustion 20 (1985) 857-870.
[68] B. Apicella, A. Carpentieri, M. Alfè, R. Barbella, A. Tregrossi, P. Pucci, A. Ciajolo, Mass spectrometric analysis of large PAH in a fuel-rich ethylene flame, Proceedings of the Combustion Institute 31 (2007) 547-553.
[69] J. Appel, H. Bockhorn, M. Frenklach, Kinetic modeling of soot formation with detailed chemistry and physics: Laminar premixed flames of C2 hydrocarbons, Combustion and Flame 121 (2000) 122-136.
[70] J.Z. Wen, M.J. Thomson, S.H. Park, S.N. Rogak, M.F. Lightstone, Study of soot growth in a plug flow reactor using a moving sectional model, Proceedings of the Combustion Institute 30 (2005) 1477-1484.
[71] J. Singh, R.I.A. Patterson, M. Kraft, H. Wang, Numerical simulation and sensitivity analysis of detailed soot particle size distribution in laminar premixed ethylene flames, Combustion and Flame 145 (2006) 117-127.
[72] S.B. Dworkin, Q. Zhang, M.J. Thomson, N.A. Slavinskaya, U. Riedel, Application of an enhanced PAH growth model to soot formation in a laminar coflow ethylene/air diffusion flame, Combustion and Flame 158 (2011) 1682-1695.
[73] H.F. Calcote, Mechanisms of soot nucleation in flames—A critical review, Combustion and Flame 42 (1981) 215-242.
[74] S.J. Harris, A.M. Weiner, Surface Growth of Soot Particles in Premixed Ethylene/Air Flames, Combustion Science and Technology 31 (1983) 155-167.
[75] S.J. Harris, A.M. Weiner, Determination of the Rate Constant for Soot Surface Growth, Combustion Science and Technology 32 (1983) 267-275.
[76] I. Glassman, Soot formation in combustion processes, Symposium (International) on Combustion 22 (1989) 295-311.
[77] M. Frenklach, H. Wang, Detailed modeling of soot particle nucleation and growth, Symposium (International) on Combustion 23 (1991) 1559-1566.
[78] A. D'Anna, A. Violi, A. D'Alessio, A.F. Sarofim, A reaction pathway for nanoparticle formation in rich premixed flames, Combustion and Flame 127 (2001) 1995-2003.
[79] D. Chen, Z. Zainuddin, E. Yapp, J. Akroyd, S. Mosbach, M. Kraft, A fully coupled simulation of PAH and soot growth with a population balance model, Proceedings of the Combustion Institute 34 (2013) 1827-1835.

[80] A. D'Anna, M. Sirignano, J. Kent, A model of particle nucleation in premixed ethylene flames, Combustion and Flame 157 (2010) 2106-2115.
[81] M. Sirignano, J. Kent, A. D'Anna, Detailed modeling of size distribution functions and hydrogen content in combustion-formed particles, Combustion and Flame 157 (2010) 1211-1219.
[82] F. Bisetti, G. Blanquart, M.E. Mueller, H. Pitsch, On the formation and early evolution of soot in turbulent nonpremixed flames, Combustion and Flame 159 (2012) 317-335.
[83] P. Pedata, T. Stöger, R. Zimmermann, A. Peters, G. Oberdörster, A. D'Anna, "Are we forgetting the smallest, sub 10 nm combustion generated particles?", 2015.
[84] B. Apicella, P. Pré, M. Alfè, A. Ciajolo, V. Gargiulo, C. Russo, A. Tregrossi, D. Deldique, J.N. Rouzaud, Soot nanostructure evolution in premixed flames by High Resolution Electron Transmission Microscopy (HRTEM), Proceedings of the Combustion Institute 35 (2015) 1895-1902.
[85] C. Russo, A. Ciajolo, Effect of the flame environment on soot nanostructure inferred by Raman spectroscopy at different excitation wavelengths, Combustion and Flame 162 (2015) 2431-2441.
[86] R.L. Vander Wal, A.J. Tomasek, Soot nanostructure: dependence upon synthesis conditions, Combustion and Flame 136 (2004) 129-140.
[87] R.A. Dobbins, H. Subramaniasivam, Soot Precursor Particles in Flames, in: H. Bockhorn (Ed.), Soot Formation in Combustion: Mechanisms and Models, Springer Berlin Heidelberg, Berlin, Heidelberg, 1994, pp. 290-301.
[88] A. D'Alessio, A. D'Anna, G. Gambi, P. Minutolo, The spectroscopic characterisation of UV absorbing nanoparticles in fuel rich soot forming flames, Journal of Aerosol Science 29 (1998) 397-409.
[89] T.C. Bond, R.W. Bergstrom, Light Absorption by Carbonaceous Particles: An Investigative Review, Aerosol Science and Technology 40 (2006) 27-67.
[90] R.L. Vander Wal, Laser-induced incandescence: detection issues, Applied Optics 35 (1996) 6548-6559.
[91] R.L. Vander Wal, T.M. Ticich, A. Brock Stephens, Can soot primary particle size be determined using laser-induced incandescence?, Combustion and Flame 116 (1999) 291-296.
[92] T.C. Williams, C.R. Shaddix, K.A. Jensen, J.M. Suo-Anttila, Measurement of the dimensionless extinction coefficient of soot within laminar diffusion flames, International Journal of Heat and Mass Transfer 50 (2007) 1616-1630.
[93] K.C. Smyth, C.R. Shaddix, The elusive history of (m)over-bar=1.57-0.56i for the refractive index of soot, Combustion and Flame 107 (1996) 314-320.
[94] R.A. Dobbins, R.A. Fletcher, H.C. Chang, The evolution of soot precursor particles in a diffusion flame, Combustion and Flame 115 (1998) 285-298.
[95] R.L. Vander Wal, Soot precursor material: Visualization via simultaneous LIF-LII and characterization via tem, Symposium (International) on Combustion 26 (1996) 2269-2275.
[96] R.A. Dobbins, R.A. Fletcher, W. Lu, Laser microprobe analysis of soot precursor particles and carbonaceous soot, Combustion and Flame 100 (1995) 301-309.
[97] M. Commodo, G. De Falco, A. Bruno, C. Borriello, P. Minutolo, A. D'Anna, Physicochemical evolution of nascent soot particles in a laminar premixed flame: from nucleation to early growth, Combustion and Flame 162 (2015) 3854-3863.

[98] A. Bruno, C. de Lisio, P. Minutolo, A. D'Alessio, Evidence of fluorescent carbon nanoparticles produced in premixed flames by time-resolved fluorescence polarization anisotropy, Combustion and Flame 151 (2007) 472-481.
[99] M. Commodo, S. Violi, A. D'Anna, A. D'Alessio, C. Allouis, F. Beretta, P. Minutolo, Soot and Nanoparticle Formation in Laminar and Turbulent Flames, Combustion Science and Technology 179 (2007) 387-400.
[100] G. Rusciano, A.C. De Luca, A. D'Alessio, P. Minutolo, G. Pesce, A. Sasso, Surface-enhanced Raman scattering study of nano-sized organic carbon particles produced in combustion processes, Carbon 46 (2008) 335-341.
[101] A. D'Anna, A. Rolando, C. Allouis, P. Minutolo, A. D'Alessio, Nano-organic carbon and soot particle measurements in a laminar ethylene diffusion flame, Proceedings of the Combustion Institute 30 (2005) 1449-1456.
[102] S.L. Fiedler, S. Izvekov, A. Violi, The effect of temperature on nanoparticle clustering, Carbon 45 (2007) 1786-1794.
[103] C. Russo, A. Tregrossi, A. Ciajolo, Dehydrogenation and growth of soot in premixed flames, Proceedings of the Combustion Institute 35 (2015) 1803-1809.
[104] M. Commodo, A. D'Anna, G. De Falco, R. Larciprete, P. Minutolo, Illuminating the earliest stages of the soot formation by photoemission and Raman spectroscopy, Combustion and Flame 181 (2017) 188-197.
[105] P. Elvati, V.T. Dillstrom, A. Violi, Oxygen driven soot formation, Proceedings of the Combustion Institute 36 (2017) 825-832.
[106] K.O. Johansson, T. Dillstrom, M. Monti, F. El Gabaly, M.F. Campbell, P.E. Schrader, D.M. Popolan-Vaida, N.K. Richards-Henderson, K.R. Wilson, A. Violi, H.A. Michelsen, Formation and emission of large furans and oxygenated hydrocarbons from flames, Proceedings of the National Academy of Sciences of the United States of America 113 (2016) 8374-8379.
[107] R.L. Vander Wal, A TEM Methodology for the Study of Soot Particle Structure, Combustion Science and Technology 126 (1997) 333-357.
[108] Ü.Ö. Köylü, G.M. Faeth, Structure of overfire soot in buoyant turbulent diffusion flames at long residence times, Combustion and Flame 89 (1992) 140-156.
[109] Ü.Ö. Köylü, G.M. Faeth, T.L. Farias, M.G. Carvalho, Fractal and projected structure properties of soot aggregates, Combustion and Flame 100 (1995) 621-633.
[110] K.O. Johansson, F. El Gabaly, P.E. Schrader, M.F. Campbell, H.A. Michelsen, Evolution of maturity levels of the particle surface and bulk during soot growth and oxidation in a flame, Aerosol Science and Technology 51 (2017) 1333-1344.
[111] R.P. Bambha, M.A. Dansson, P.E. Schrader, H.A. Michelsen, Effects of volatile coatings and coating removal mechanisms on the morphology of graphitic soot, Carbon 61 (2013) 80-96.
[112] M. Sirignano, A. D'Anna, Coagulation of combustion generated nanoparticles in low and intermediate temperature regimes: An experimental study, Proceedings of the Combustion Institute 34 (2013) 1877-1884.
[113] M. Salamanca, M. Sirignano, A. Danna, Particulate formation in premixed and counter-flow diffusion ethylene/ethanol flames, Energy and Fuels 26 (2012) 6144-6152.
[114] P. Minutolo, G. Gambi, A. D'Alessio, S. Carlucci, Spectroscopic characterisation of carbonaceous nanoparticles in premixed flames, Atmospheric Environment 33 (1999) 2725-2732.

[115] R. Sun, N. Zobel, Y. Neubauer, C. Cardenas Chavez, F. Behrendt, Analysis of gas-phase polycyclic aromatic hydrocarbon mixtures by laser-induced fluorescence, Optics and Lasers in Engineering 48 (2010) 1231-1237.
[116] R.L. Vander Wal, K.A. Jensen, M.Y. Choi, Simultaneous laser-induced emission of soot and polycyclic aromatic hydrocarbons within a gas-jet diffusion flame, Combustion and Flame 109 (1997) 399-414.
[117] F. Ossler, T. Metz, M. Aldén, Picosecond laser-induced fluorescence from gas-phase polycyclic aromatic hydrocarbons at elevated temperatures. I. Cell measurements, Applied Physics B 72 (2001) 465-478.
[118] A. Bruno, M. Alfè, B. Apicella, C. de Lisio, P. Minutolo, Characterization of nanometric carbon materials by time-resolved fluorescence polarization anisotropy, Optics and Lasers in Engineering 44 (2006) 732-746.
[119] A. Bruno, F. Ossler, C.d. Lisio, P. Minutolo, N. Spinelli, A. D'Alessio, Detection of fluorescent nanoparticles in flame with femtosecond laser-induced fluorescence anisotropy, Optics Express 16 (2008) 5623-5632.
[120] A. Bruno, C.d. Lisio, P. Minutolo, Time resolved fluorescence polarization anisotropy of carbonaceous particles produced in combustion systems, Optics Express 13 (2005) 5393-5408.
[121] A. Bruno, C.d. Lisio, P. Minutolo, A. D'Alessio, Characterization of ultrafast fluorescence from nanometric carbon particles, Journal of Optics A: Pure and Applied Optics 8 (2006) S578-S584.
[122] M. Commodo, L.A. Sgro, X. Wang, C. De Lisio, P. Minutolo, Fluorescence anisotropy in a diffusion flame to shed light in the 'dark region', Proceedings of the Combustion Institute 34 (2013) 1845-1852.
[123] K. Hayashida, T. Mogi, K. Amagai, M. Arai, Growth characteristics of polycyclic aromatic hydrocarbons in dimethyl ether diffusion flame, Fuel 90 (2011) 493-498.
[124] K. Hayashida, K. Amagai, K. Satoh, M. Arai, Experimental analysis of soot formation in shooting diffusion flame by using laser-induced emissions, Journal of Engineering for Gas Turbines and Power 128 (2006) 241.
[125] P.O. Witze, S. Hochgreb, D. Kayes, H.A. Michelsen, C.R. Shaddix, Time-resolved laser-induced incandescence and laser elastic-scattering measurements in a propane diffusion flame, Applied Optics 40 (2001) 2443-2452.
[126] S.-H. Chung, A. Violi, Peri-condensed aromatics with aliphatic chains as key intermediates for the nucleation of aromatic hydrocarbons, Proceedings of the Combustion Institute 33 (2011) 693-700.
[127] M. Sirignano, J. Kent, A. D'Anna, Modeling formation and oxidation of soot in nonpremixed flames, Energy and Fuels 27 (2013) 2303-2315.
[128] M. Kholghy, M. Saffaripour, C. Yip, M.J. Thomson, The evolution of soot morphology in a laminar coflow diffusion flame of a surrogate for Jet A-1, Combustion and Flame 160 (2013) 2119-2130.
[129] S.H. Chung, A. Violi, Insights on the nanoparticle formation process in counterflow diffusion flames, Carbon 45 (2007) 2400-2410.
[130] P. Minutolo, G. Gambi, A. D'Alessio, The optical band gap model in the interpretation of the UV-visible absorption spectra of rich premixed flames, Symposium (International) on Combustion 26 (1996) 951-957.

[131] L.A. Sgro, A.C. Barone, M. Commodo, A. D'Alessio, A. De Filippo, G. Lanzuolo, P. Minutolo, Measurement of nanoparticles of organic carbon in non-sooting flame conditions, Proceedings of the Combustion Institute 32 (2009) 689-696.
[132] L.A. Sgro, G. Basile, A.C. Barone, A. D'Anna, P. Minutolo, A. Borghese, A. D'Alessio, Detection of combustion formed nanoparticles, Chemosphere 51 (2003) 1079-1090.
[133] G. Basile, A. Rolando, A. D'Alessio, A. D'Anna, P. Minutolo, Coagulation and carbonization processes in slightly sooting premixed flames, Proceedings of the Combustion Institute 29 (2002) 2391-2397.
[134] L.A. Sgro, P. Minutolo, G. Basile, A. D'Alessio, UV-visible spectroscopy of organic carbon particulate sampled from ethylene/air flames, Chemosphere 42 (2001) 671-680.
[135] J.R. Lakowicz, SpringerLink, Principles of Fluorescence Spectroscopy, Springer US, Boston, MA, 2006.
[136] I.B. Berlman, Handbook of fluorescence spectra of aromatic molecules, Elsevier Science, Burlington, 2012.
[137] R.A. Dobbins, Hydrocarbon Nanoparticles Formed in Flames and Diesel Engines, Aerosol Science and Technology 41 (2007) 485-496.
[138] A.D. Abid, N. Heinz, E.D. Tolmachoff, D.J. Phares, C.S. Campbell, H. Wang, On evolution of particle size distribution functions of incipient soot in premixed ethylene–oxygen–argon flames, Combustion and Flame 154 (2008) 775-788.
[139] B. Zhao, K. Uchikawa, H. Wang, A comparative study of nanoparticles in premixed flames by scanning mobility particle sizer, small angle neutron scattering, and transmission electron microscopy, Proceedings of the Combustion Institute 31 (2007) 851-860.
[140] A.C. Barone, A. D'Alessio, A. D'Anna, Morphological characterization of the early process of soot formation by atomic force microscopy, Combustion and Flame 132 (2003) 181-187.
[141] A. Santamaria, N. Yang, E. Eddings, F. Mondragon, Chemical and morphological characterization of soot and soot precursors generated in an inverse diffusion flame with aromatic and aliphatic fuels, Combustion and Flame 157 (2010) 33-42.
[142] N.J. Kempema, M.B. Long, Combined optical and TEM investigations for a detailed characterization of soot aggregate properties in a laminar coflow diffusion flame, Combustion and Flame 164 (2016) 373-385.
[143] K. Hayashida, S. Nagaoka, H. Ishitani, Growth and oxidation of graphitic crystallites in soot particles within a laminar diffusion flame, Fuel 128 (2014) 148-154.
[144] A. De Filippo, L.A. Sgro, G. Lanzuolo, P. Minutolo, A. D'Anna, A. D'Alessio, Formation and growth of nanoparticles in non-sooting rich premixed flames, Spring Meeting of the Western States Section of the Combustion Institute , March17 & 18, 2008, University of Southern California, USA, 2008.
[145] A. D'Alessio, A.C. Barone, R. Cau, A. D'Anna, P. Minutolo, Surface deposition and coagulation efficiency of combustion generated nanoparticles in the size range from 1 to 10 nm, Proceedings of the Combustion Institute 30 (2005) 2595-2603.
[146] P. Minutolo, A. D'Anna, A. D'Alessio, On detection of nanoparticles below the sooting threshold, Combustion and Flame 152 (2008) 287-292.
[147] M.M. Maricq, A comparison of soot size and charge distributions from ethane, ethylene, acetylene, and benzene/ethylene premixed flames, Combustion and Flame 144 (2006) 730-743.

[148] D.R. Snelling, O. Link, K.A. Thomson, G.J. Smallwood, Measurement of soot morphology by integrated LII and elastic light scattering, Applied Physics B 104 (2011) 385-397.
[149] R.L. Vander Wal, T.M. Ticich, A.B. Stephens, Optical and microscopy investigations of soot structure alterations by laser-induced incandescence, Applied Physics B 67 (1998) 115-123.
[150] H.A. Michelsen, A.V. Tivanski, M.K. Gilles, L.H. Van Poppel, M.A. Dansson, P.R. Buseck, Particle formation from pulsed laser irradiation of soot aggregates studied with a scanning mobility particle sizer, a transmission electron microscope, and a scanning transmission x-ray microscope, Applied Optics 46 (2007) 959-977.
[151] B.M. Crosland, K.A. Thomson, M.R. Johnson, Instantaneous in-flame measurement of soot volume fraction, primary particle diameter, and aggregate radius of gyration via auto-compensating laser-induced incandescence and two-angle elastic light scattering, Applied Physics B 112 (2013) 381-393.
[152] Y.Y. Wei, L.L. Ma, T.T. Cao, Q. Zhang, J. Wu, P.R. Buseck, J.E. Thompson, Light Scattering and Extinction Measurements Combined with Laser-Induced Incandescence for the Real-Time Determination of Soot Mass Absorption Cross Section, Analytical Chemistry 85 (2013) 9181-9188.
[153] B. Ma, M.B. Long, Combined soot optical characterization using 2-D multi-angle light scattering and spectrally resolved line-of-sight attenuation and its implication on soot color-ratio pyrometry, Applied Physics B 117 (2014) 287-303.
[154] G. De Falco, M. Commodo, C. Bonavolonta, G.P. Pepe, P. Minutolo, A. D'Anna, Optical and electrical characterization of carbon nanoparticles produced in laminar premixed flames, Combustion and Flame 161 (2014) 3201-3210.
[155] C. Saggese, A. Cuoci, A. Frassoldati, S. Ferrario, J. Camacho, H. Wang, T. Faravelli, Probe effects in soot sampling from a burner-stabilized stagnation flame, Combustion and Flame 167 (2016) 184-197.
[156] F. Carbone, S. Moslih, A. Gomez, Probing gas-to-particle transition in a moderately sooting atmospheric pressure ethylene/air laminar premixed flame. Part II: Molecular clusters and nascent soot particle size distributions, Combustion and Flame 181 (2017) 329-341.
[157] B. Hu, B. Yang, U.O. Koylu, Soot measurements at the axis of an ethylene/air non-premixed turbulent jet flame, Combustion and Flame 134 (2003) 93-106.
[158] B. Hu, U. Koylu, Size and Morphology of Soot Particulates Sampled from a Turbulent Nonpremixed Acetylene Flame, Aerosol Science and Technology 38 (2004) 1009-1018.
[159] B.O. Yang, B. Hu, U.O. Koylu, Mean Soot Volume Fractions in Turbulent Hydrocarbon Flames: A Comparison of Sampling and Laser Measurements, Combustion Science and Technology 177 (2005) 1603-1626.
[160] G.P. Reischl, J.M. Mäkelä, R. Karch, J. Necid, Bipolar charging of ultrafine particles in the size range below 10 nm, Journal of Aerosol Science 27 (1996) 931-949.
[161] A.P.D.P. Intra, N. Tippayawong, An overview of differential mobility analyzers for size classification of nanometer-sized aerosol particles, 2008.
[162] P. Roth, A.V. Filippov, In situ ultrafine particle sizing by a combination of pulsed laser heatup and particle thermal emission, Journal of Aerosol Science 27 (1996) 95-104.

[163] A.V. Filippov, M.W. Markus, P. Roth, In-situ characterization of ultrafine particles by laser-induced incandescence: sizing and particle structure determination, Journal of Aerosol Science 30 (1999) 71-87.
[164] T. Lehre, B. Jungfleisch, R. Suntz, H. Bockhorn, Size distributions of nanoscaled particles and gas temperatures from time-resolved laser-induced-incandescence measurements, Applied Optics 42 (2003) 2021-2030.
[165] R.J. Santoro, H.G. Semerjian, Soot formation in diffusion flames: Flow rate, fuel species and temperature effects, Symposium (International) on Combustion 20 (1985) 997-1006.
[166] B. Axelsson, R. Collin, P.E. Bengtsson, Laser-induced incandescence for soot particle size and volume fraction measurements using on-line extinction calibration, Applied Physics B 72 (2001) 367-372.
[167] N.J. Kempema, M.B. Long, Quantitative Rayleigh thermometry for high background scattering applications with structured laser illumination planar imaging, Applied Optics 53 (2014) 6688-6697.
[168] T. Joutsenoja, A. D'Anna, A. D'Alessio, M.I. Nazzaro, Ultraviolet absorption spectra of carbon dioxide and oxygen at elevated temperatures, Applied Spectroscopy 55 (2001) 130-135.
[169] H.A. Michelsen, Understanding and predicting the temporal response of laser-induced incandescence from carbonaceous particles, Journal of Chemical Physics 118 (2003) 7012-7045.
[170] S. De Iuliis, M. Barbini, S. Benecchi, F. Cignoli, G. Zizak, Determination of the Soot Volume Fraction in an Ethylene Diffusion Flame by Multiwavelength Analysis of Soot Radiation, Combustion and Flame 115 (1998) 253-261.
[171] H. Chang, T.T. Charalampopoulos, Determination of the Wavelength Dependence of Refractive-Indexes of Flame Soot, Proceedings of the Royal Society-Mathematical and Physical Sciences 430 (1990) 577-591.
[172] D.R. Snelling, F. Liu, G.J. Smallwood, Ö.L. Gülder, Determination of the soot absorption function and thermal accommodation coefficient using low-fluence LII in a laminar coflow ethylene diffusion flame, Combustion and Flame 136 (2004) 180-190.
[173] R.T. Wainner, J.M. Seitzman, Soot diagnostics using laser-induced incandescence in flames and exhaust flows, American Institute of Aeronautics & Astronautics, (1999).
[174] H. Bladh, P.E. Bengtsson, J. Delhay, Y. Bouvier, E. Therssen, P. Desgroux, Experimental and theoretical comparison of spatially resolved laser-induced incandescence (LII) signals of soot in backward and right-angle configuration, Applied Physics B 83 (2006) 423-433.
[175] H. Bladh, J. Johnsson, P.-E. Bengtsson, On the dependence of the laser-induced incandescence (LII) signal on soot volume fraction for variations in particle size, Applied Physics B 90 (2008) 109-125.
[176] F. Goulay, L. Nemes, P.E. Schrader, H.A. Michelsen, Spontaneous emission from C2(d 3Πg) and C3(A 1Πu) during laser irradiation of soot particles, Molecular Physics 108 (2010) 1013-1025.
[177] F. Goulay, P.E. Schrader, L. Nemes, M.A. Dansson, H.A. Michelsen, Photochemical interferences for laser-induced incandescence of flame-generated soot, Proceedings of the Combustion Institute 32 (2009) 963-970.

[178] F. Goulay, P.E. Schrader, X. López-Yglesias, H.A. Michelsen, A data set for validation of models of laser-induced incandescence from soot: temporal profiles of LII signal and particle temperature, Applied Physics B 112 (2013) 287-306.
[179] C.B. Stipe, J.H. Choi, D. Lucas, C.P. Koshland, R.F. Sawyer, Nanoparticle production by UV irradiation of combustion generated soot particles, Journal of Nanoparticle Research 6 (2004) 467-477.
[180] C.B. Stipe, D. Lucas, C.P. Koshland, R.F. Sawyer, Soot particle disintegration and detection by two-laser excimer laser fragmentation fluorescence spectroscopy, Applied Optics 44 (2005) 6537-6544.
[181] J.H. Choi, D. Lucas, C.P. Koshland, Laser ablation of nanoscale particles with 193 nm light, Journal of Physics: Conference Series 59 (2007) 54-59.
[182] E.A. Rohlfing, Optical emission studies of atomic, molecular, and particulate carbon produced from a laser vaporization cluster source, The Journal of Chemical Physics 89 (1988) 6103-6112.
[183] P.-E. Bengtsson, M. Aldén, Optical investigation of laser-produced C2 in premixed sooty ethylene flames, Combustion and Flame 80 (1990) 322-328.
[184] M. Commodo, F. Ossler, C. de Lisio, A. D'Anna, P. Minutolo, Size Measurements of Fluorescent Carbon Nanoparticles in a Coflowing Laminar Diffusion Flame by Time-Resolved Fluorescence Anisotropy, Combustion Science and Technology 184 (2012) 916-928.
[185] Z. Chi, B.M. Cullum, D.L. Stokes, J. Mobley, G.H. Miller, M.R. Hajaligol, T. Vo-Dinh, Laser-induced fluorescence studies of polycyclic aromatic hydrocarbons (PAH) vapors at high temperatures, Spectrochimica Acta Part A: Molecular and Biomolecular Spectroscopy 57 (2001) 1377-1384.
[186] A. D'Anna, M. Sirignano, M. Commodo, R. Pagliara, P. Minutolo, An Experimental and Modelling Study of Particulate Formation in Premixed Flames Burning Methane, Combustion Science and Technology 180 (2008) 950-958.
[187] A. Bruno, M. Alfè, A. Ciajolo, C. de Lisio, P. Minutolo, Time-resolved fluorescence polarization anisotropy of multimodal samples: the asphaltene case, Applied Physics B 90 (2008) 61-67.
[188] M.V. Heitor, A.L.N. Moreira, Thermocouples and sample probes for combustion studies, Progress in Energy and Combustion Science 19 (1993) 259-278.
[189] J.H. Kint, A noncatalytic coating for platinum-rhodium thermocouples, Combustion and Flame 14 (1970) 279-281.
[190] G. De Falco, M. Commodo, A. D'Anna, P. Minutolo, The evolution of soot particles in premixed and diffusion flames by thermophoretic particle densitometry, Proceedings of the Combustion Institute 36 (2017) 763-770.
[191] G. De Falco, G. Moggia, M. Sirignano, M. Commodo, P. Minutolo, A. D'Anna, Exploring soot particle concentration and emissivity by transient thermocouples measurements in laminar partially premixed coflow flames, Energies 10 (2017) 232.
[192] C.S. McEnally, Ü.Ö. Köylü, L.D. Pfefferle, D.E. Rosner, Soot volume fraction and temperature measurements in laminar nonpremixed flames using thermocouples, Combustion and Flame 109 (1997) 701-720.
[193] S.B. Dworkin, B.C. Connelly, A.M. Schaffer, B.A.V. Bennett, M.B. Long, M.D. Smooke, M.P. Puccio, B. McAndrews, J.H. Miller, Computational and experimental study

of a forced, time-dependent, methane–air coflow diffusion flame, Proceedings of the Combustion Institute 31 (2007) 971-978.
[194] W. Yao, J. Zhang, A. Nadjai, T. Beji, M.A. Delichatsios, A global soot model developed for fires: Validation in laminar flames and application in turbulent pool fires, Fire Safety Journal 46 (2011) 371-387.
[195] Yunardi, R.M. Woolley, M. Fairweather, Conditional moment closure prediction of soot formation in turbulent, nonpremixed ethylene flames, Combustion and Flame 152 (2008) 360-376.
[196] B.M. Vaglieco, S.S. Merola, A. D'Anna, A. D'Alessio, Spectroscopic analysis and modeling of particulate formation in a diesel engine, Journal of Quantitative Spectroscopy and Radiative Transfer 73 (2002) 443-450.
[197] M. Sirignano, M. Alfè, A. Tregrossi, A. Ciajolo, A. D'Anna, Experimental and modeling study on the molecular weight distribution and properties of carbon particles in premixed sooting flames, Proceedings of the Combustion Institute 33 (2011) 633-640.
[198] M. Sirignano, M. Conturso, A. D'Anna, Effect of furans on particle formation in diffusion flames: An experimental and modeling study, Proceedings of the Combustion Institute 35 (2015) 525-532.
[199] M. Sirignano, J. Kent, A. D'Anna, Further experimental and modelling evidences of soot fragmentation in flames, Proceedings of the Combustion Institute 35 (2015) 1779-1786.
[200] G. Nathan, International Sooting Flame (ISF) Workshop. http://www.adelaide.edu.au/cet/isfworkshop/ 2017).
[201] M. Salamanca, M. Sirignano, M. Commodo, P. Minutolo, A. D'Anna, The effect of ethanol on the particle size distributions in ethylene premixed flames, Experimental Thermal and Fluid Science 43 (2012) 71-75.
[202] M. Conturso, M. Sirignano, A. D'Anna, Effect of alkylated aromatics on particle formation in diffusion flames: An experimental study, Experimental Thermal and Fluid Science 73 (2016) 27-32.
[203] F. Goulay, P.E. Schrader, H.A. Michelsen, The effects of pulsed laser injection seeding and triggering on the temporal behavior and magnitude of laser-induced incandescence from soot, Applied Physics B 96 (2009) 613-621.
[204] Photomultiplier Handbook, Burle Industries Inc, USA, 1980.
[205] M. Commodo, G. Tessitore, G. De Falco, A. Bruno, P. Minutolo, A. D'Anna, Further details on particle inception and growth in premixed flames, Proceedings of the Combustion Institute 35 (2015) 1795-1802.
[206] E. Cenker, G. Bruneaux, T. Dreier, C. Schulz, Determination of small soot particles in the presence of large ones from time-resolved laser-induced incandescence, Applied Physics B 118 (2015) 169-183.
[207] C.S. McEnally, A.M. Schaffer, M.B. Long, L.D. Pfefferle, M.D. Smooke, M.B. Colket, R.J. Hall, Computational and experimental study of soot formation in a coflow, laminar ethylene diffusion flame, Symposium (International) on Combustion 27 (1998) 1497-1505.
[208] B.C. Connelly, M.B. Long, M.D. Smooke, R.J. Hall, M.B. Colket, Computational and experimental investigation of the interaction of soot and NO in coflow diffusion flames, Proceedings of the Combustion Institute 32 (2009) 777-784.

[209] Yale Coflow Diffusion Flames. http://guilford.eng.yale.edu/yalecoflowflames/index.html 2017).
[210] B.C. Connelly, B.A.V. Bennett, M.D. Smooke, M.B. Long, A paradigm shift in the interaction of experiments and computations in combustion research, Proceedings of the Combustion Institute 32 (2009) 879-886.
[211] N.J. Kempema, M.B. Long, Boundary condition thermometry using a thermographic-phosphor-coated thin filament, Applied Optics 55 (2016) 4691-4698.
[212] N.J. Kempema, B. Ma, M.B. Long, Investigation of in-flame soot optical properties in laminar coflow diffusion flames using thermophoretic particle sampling and spectral light extinction, Applied Physics B 122 (2016) 1-13.
[213] P.B. Kuhn, B. Ma, B.C. Connelly, M.D. Smooke, M.B. Long, Soot and thin-filament pyrometry using a color digital camera, Proceedings of the Combustion Institute 33 (2011) 743-750.
[214] L. Holthuis, Holthuis & Associates Flat Flame Burners. http://www.flatflame.com/home.html 2017).
[215] M. Sirignano, M. Salamanca, A. D'Anna, The role of dimethyl ether as substituent to ethylene on particulate formation in premixed and counter-flow diffusion flames, Fuel 126 (2014) 256-262.
[216] C. Russo, A. D'Anna, A. Ciajolo, M. Sirignano, Analysis of the chemical features of particles generated from ethylene and ethylene/2,5 dimethyl furan flames, Combustion and Flame 167 (2016) 268-273.
[217] A.R. Masri, R.W. Dibble, R.S. Barlow, The structure of turbulent nonpremixed flames revealed by Raman-Rayleigh-LIF measurements, Progress in Energy and Combustion Science 22 (1996) 307-362.
[218] J.Y. Zhang, C.R. Shaddix, R.W. Schefer, Design of "model-friendly" turbulent non-premixed jet burners for C2+ hydrocarbon fuels, Review of Scientific Instruments 82 (2011) 074101.
[219] J.H. kent, H.G. Wagner, Who do Diffusion flames Emit smoke, Combustion Science and Technology 41 (1984) 245-269.
[220] M. Sirignano, Nanoparticle in high temperature environment: experimental techniques and aspects of synthesis properties, Università degli Studi di Napoli Federico II, 2011.
[221] C.B. Stipe, B.S. Higgins, D.D. Lucas, C.P. Koshland, R.F. Sawyer, Soot detection using excimer laser fragmentation fluorescence spectroscopy, Proceedings of the Combustion Institute 29 (2002) 2759-2766.
[222] C.J. Damm, D. Lucas, R.F. Sawyer, C.P. Koshland, Characterization of diesel particulate matter with excimer laser fragmentation fluorescence spectroscopy, Proceedings of the Combustion Institute 29 (2002) 2767-2774.
[223] W. Hinds, Aerosol Technology-properties, behavior, and measurement of airborne particles", John Wiley & Sons, 1982.
[224] H.A. Michelsen, P.O. Witze, D. Kayes, S. Hochgreb, Time-resolved laser-induced incandescence of soot: the influence of experimental factors and microphysical mechanisms, Applied Optics 42 (2003) 5577-5590.
[225] K.O. Johansson, T. Dillstrom, P. Elvati, M.F. Campbell, P.E. Schrader, D.M. Popolan-Vaida, N.K. Richards-Henderson, K.R. Wilson, A. Violi, H.A. Michelsen,

Radical–radical reactions, pyrene nucleation, and incipient soot formation in combustion, Proceedings of the Combustion Institute 36 (2017) 799-806.
[226] J.B. Birks, Organic molecular photophysics, J. Wiley, London;New York;, 1973.
[227] G. De Falco, M. Commodo, P. Minutolo, A. D'Anna, Flame-Formed Carbon Nanoparticles: Morphology, Interaction Forces, and Hamaker Constant from AFM, 2015.
[228] B.M. Cetegen, S. Basu, Soot topography in a planar diffusion flame wrapped by a line vortex, Combustion and Flame 146 (2006) 687-697.
[229] H.S. Hura, I. Glassman, Fuel Oxygen Effects on Soot Formation in Counterflow Diffusion Flames, Combustion Science and Technology 53 (1987) 1-21.
[230] K.T. Walsh, J. Fielding, M.D. Smooke, M.B. Long, Experimental and computational study of temperature, species, and soot in buoyant and non-buoyant coflow laminar diffusion flames, Proceedings of the Combustion Institute 28 (2000) 1973-1979.
[231] Object-Oriented Software for Reacting Flows. https://cantera.org/ 2016).
[232] Y. Kobayashi, T. Furuhata, K. Amagai, M. Arai, Soot precursor measurements in benzene and hexane diffusion flames, Combustion and Flame 154 (2008) 346-355.
[233] M.D. Smooke, R.J. Hall, M.B. Colket, J. Fielding, M.B. Long, C.S. McEnally, L.D. Pfefferle, Investigation of the transition from lightly sooting towards heavily sooting co-flow ethylene diffusion flames, Combustion Theory and Modelling 8 (2004) 593-606.
[234] H.A. Michelsen, Laser-induced incandescence of flame-generated soot on a picosecond time scale, Applied Physics B 83 (2006) 443.
[235] C.S. McEnally, L.D. Pfefferle, Experimental study of nonfuel hydrocarbons and soot in coflowing partially premixed ethylene/air flames, Combustion and Flame 121 (2000) 575-592.
[236] A. Mitrovic, T.W. Lee, Soot formation characteristics of laminar partially premixed flames, Combustion and Flame 115 (1998) 437-442.
[237] C.S. McEnally, L.D. Pfefferle, Experimental study of nonfuel hydrocarbon concentrations in coflowing partially premixed methane/air flames, Combustion and Flame 118 (1999) 619-632.
[238] C.S. McEnally, L.D. Pfefferle, The Effect of Nitrogen Dilution on Nonfuel Hydrocarbons in Laminar Nonpremixed Flames, Combustion Science and Technology 151 (2000) 133-155.
[239] H.S. Hura, I. Glassman, Soot formation in diffusion flames of fuel/oxygen mixtures, Symposium (International) on Combustion 22 (1989) 371-378.
[240] Z.W. Sun, B. Dally, G. Nathan, Z. Alwahabi, Effects of hydrogen and nitrogen on soot volume fraction, primary particle diameter and temperature in laminar ethylene/air diffusion flames, Combustion and Flame 175 (2017) 270-282.
[241] Ö.L. Gülder, D.R. Snelling, Influence of nitrogen dilution and flame temperature on soot formation in diffusion flames, Combustion and Flame 92 (1993) 115-124.
[242] Ö.L. Gülder, Effects of oxygen on soot formation in methane, propane, and n-Butane diffusion flames, Combustion and Flame 101 (1995) 302-310.
[243] J.Y. Hwang, S.H. Chung, W. Lee, Effects of oxygen and propane addition on soot formation in counterflow ethylene flames and the role of C3 chemistry, Proceedings of the Combustion Institute 27 (1998) 1531-1538.
[244] O.L. Gulder, Dependence of sooting characteristics and temperature field of co-flow laminar pure and nitrogen-diluted ethylene-air diffusion flames on pressure, Combustion and Flame 162 (2015) 1566-1574.

[245] M.R.J. Charest, H.I. Joo, Ö.L. Gülder, C.P.T. Groth, Experimental and numerical study of soot formation in laminar ethylene diffusion flames at elevated pressures from 10 to 35 atm, Proceedings of the Combustion Institute 33 (2011) 549-557.
[246] D. Gu, Z. Sun, B.B. Dally, P.R. Medwell, Z.T. Alwahabi, G.J. Nathan, Simultaneous measurements of gas temperature, soot volume fraction and primary particle diameter in a sooting lifted turbulent ethylene/air non-premixed flame, Combustion and Flame 179 (2017) 33-50.
[247] V. Narayanaswamy, N.T. Clemens, Simultaneous LII and PIV measurements in the soot formation region of turbulent non-premixed jet flames, Proceedings of the Combustion Institute 34 (2013) 1455-1463.
[248] S.-Y. Lee, S.R. Turns, R.J. Santoro, Measurements of soot, OH, and PAH concentrations in turbulent ethylene/air jet flames, Combustion and Flame 156 (2009) 2264-2275.
[249] N.H. Qamar, G.J. Nathan, Z.T. Alwahabi, K.D. King, The effect of global mixing on soot volume fraction: measurements in simple jet, precessing jet, and bluff body flames, Proceedings of the Combustion Institute 30 (2005) 1493-1500.
[250] C.R. Shaddix, J.E. Harrington, K.C. Smyth, Quantitative measurements of enhanced soot production in a flickering methane/air diffusion flame, Combustion and Flame 99 (1994) 723-732.
[251] K.C. Smyth, C.R. Shaddix, D.A. Everest, Aspects of soot dynamics as revealed by measurements of broadband fluorescence and flame luminosity in flickering diffusion flames, Combustion and Flame 111 (1997) 185,IN182,195-194,IN183,207.
[252] Z.W. Sun, Z.T. Alwahabi, D.H. Gu, S.M. Mahmoud, G.J. Nathan, B.B. Dally, Planar laser-induced incandescence of turbulent sooting flames: the influence of beam steering and signal trapping, Applied Physics B 119 (2015) 731-743.
[253] B.F. Magnussen, An investigation into the behavior of soot in a turbulent free jet C2H2-flame, Symposium (International) on Combustion 15 (1975) 1415-1425.
[254] A. Gomez, M.G. Littman, I. Glassman, Comparative study of soot formation on the centerline of axisymmetric laminar diffusion flames: Fuel and temperature effects, Combustion and Flame 70 (1987) 225-241.
[255] D.R. Snelling, G.J. Smallwood, F. Liu, O.L. Gülder, W.D. Bachalo, A calibration-independent laser-induced incandescence technique for soot measurement by detecting absolute light intensity, Applied Optics 44 (2005) 6773.
[256] J. Reimann, S.-A. Kuhlmann, S. Will, 2D aggregate sizing by combining laser-induced incandescence (LII) and elastic light scattering (ELS), Applied Physics B 96 (2009) 583-592.
[257] S. Will, S. Schraml, A. Leipert, Comprehensive two-dimensional soot diagnostics based on laser-induced incandescence (LII), Symposium (International) on Combustion 26 (1996) 2277-2284.
[258] C.M. Sorensen, Light Scattering by Fractal Aggregates: A Review, Aerosol Science and Technology 35 (2001) 648-687.
[259] H. Oltmann, J. Reimann, S. Will, Single-shot measurement of soot aggregate sizes by wide-angle light scattering (WALS), Applied Physics B 106 (2012) 171-183.